Czech Technical University in Prague
Faculty of Civil Engineering

Department of Concrete and Masonry Structures

Effect of Neutron Irradiation on Concrete Aggregates

by

Bc. Syrym Sertayev

A master's thesis submitted to the Faculty of Civil Engineering, Czech Technical University in Prague, in partial fulfilment of the requirements for the degree of Master of Science.

Master degree study programme: Civil Engineering
Specialization: Building Structures

Prague, January 2021

Title of the thesis:

Effect of Neutron Irradiation on Concrete Aggregates

Student:

Bc. Syrym Sertayev
Email: syrym.sertayev@fsv.cvut.cz / ssyrym@mail.ru

Supervisor:

Mgr. Yuliia Khmurovska, Ph.D.
Email: yuliia.khmurovska@fsv.cvut.cz

Address:

Department of Concrete and Masonry Structures
Faculty of Civil Engineering
Czech Technical University in Prague
Thákurova 7
166 29 Prague 6
Czech Republic

CZECH TECHNICAL UNIVERSITY IN PRAGUE
Faculty of Civil Engineering
Thákurova 7, 166 29 Prague 6, Czech Republic

DIPLOMA THESIS ASSIGNMENT FORM

I. PERSONAL AND STUDY DATA

Surname: Sertayev Name: Syrym Personal number: 462496

Assigning Department: Concrete and Masonry Structures

Study programme: Civil Engineering - N3648

Branch of study: (3607T030) Building Structures

II. DIPLOMA THESIS DATA

Diploma Thesis (DT) title: Effect of Neutron Irradiation on Concrete Aggregates

Diploma Thesis title in English:

Instructions for writing the thesis:
Baseline characterization of non-irradiated samples
Irradiation of samples at Research Centre Řež
Baseline characterization of irradiated samples
Baseline characterization includes water and helium pycnometry, XRD, SEM+EDX, microscopy
Numerical analysis of stresses in aggregates
Discussion of effect of neutron irradiation on aggregates
Selection of most suitable rocks for concrete aggregates

List of recommended literature:
Eurocode 2 - online version
Sciencedirect.com - online scientific papers
NUREG reports - online versions

Name of Diploma Thesis Supervisor: Mgr. Yuliia Khmurovska, Ph.D.

DT assignment date: 1.10.2020 DT submission date: 3.1.2021

[redacted]
DT Supervisor's signature

[redacted]
Head of Department's signature

III. ASSIGNMENT RECEIPT

I declare that I am obliged to write the Diploma Thesis on my own, without anyone's assistance, except for provided consultations. The list of references, other sources and consultants' names must be stated in the Diploma Thesis and in referencing I must abide by the CTU methodological manual "How to Write University Final Theses" and the CTU methodological instruction "On the Observation of Ethical Principles in the Preparation of University Final Theses".

1.10.2020
Assignment receipt date

[redacted]
Student's name

Declaration

Author

Syrym Sertayev

Thesis

Effect of Neutron Irradiation on Concrete Aggregates

I hereby affirm that this master's thesis has been written by myself, under the supervision of Mgr. Yullia Khmurovska, Ph.D.

All sources of information that have been used in the thesis are acknowledged in the text and listed in the Bibliography, in accordance with the requirements given by the CTU Guideline. The results of conducted experiments in Research Centre Řež owned by Mitsubishi Research Institute, Inc., Kajima Corporation and Nagoya University.

.....
Syrym Sertayev
Prague, January 2021

Abstract

Safe exploitation of nuclear power plants is one of the main concerns of the modern society. In Japan, close attention has been made to local nuclear infrastructure especially after the incident at the Fukushima-Daiichi power plant. In such structures, concrete has found its application as a support structure for reactor and/or biological shielding wall against ionizing radiation emitted from reactor. Under the harsh radiation environment, the deterioration of concrete structures is subjected to elevated temperature, neutron and gamma radiation. When concrete aggregates are affected by neutron radiation the accumulation of defects in crystalline solids causes radiation-induced swelling. The swelling of aggregates, in general, is the main factor for degradation of strength and Young's modulus of concrete, as a consequence of crack formation and degraded physical properties of minerals. This is exactly to what drawn special attention.

In this thesis, the effect of *Radiation-Induced Volumetric Expansion (RIVE)* of selected rocks is described under the *Japanese Concrete Aging Management Program (JCAMP)* and presents the experimental results of the effects of neutron irradiation on selected rocks, or rather on minerals. The initiated research project under JCAMP was granted to Research Centre Řež.

Dedication

This thesis is dedicated to the memory of my grandfather, Sertay Kenzhalin, who was a loving husband, father, grandfather, and deputy of the Supreme Soviet of the USSR.

Acknowledgements

I would like to express my deep gratitude to my academic supervisor, Mgr. Yuliia Khmurovska, Ph.D. for her valuable comments, consultations and efforts in organization through tough times of pandemic.

I would like to express my special thanks to prof. Ing. Petr Štemberk, Ph.D., D.Eng. for his inspiration for research, and teaching to stay positive and strive for excellence.

Also, I would like to thank RNDr. Ondřej Srba, Ph.D., Mgr. Patricie Halodová, Ph.D. and other colleagues from the Research Centre Řež (Centrum výzkumu Řež s.r.o.) for a kind introduction to research experiments and consultations.

Lastly, I would like express my deepest gratitude to my parents, Serik and Yessengul, who have made great efforts in shaping future for me and my siblings.

Contents

List of Figures

List of Tables

Abbreviations

BWR	**B**oiling **W**ater **R**eactor
CBS	**C**oncrete **B**iological **S**hielding
C-S-H	**C**alcium **S**ilicate **H**ydrate
CVŘ	**R**esearch **C**entre **Ř**ež
DEM	**D**iscrete **E**lement **M**ethod
FTIR	**F**ourier-**T**ransform **I**nfrared **S**pectroscopy
IFE	**I**nstitute **f**or **E**nergy
ITZ	**I**nterfacial **T**ransition **Z**one
LOM	**L**ight **O**ptical **M**icroscope
LVR-15	(***L**ehko**V**odní-**R**eaktor-**15***) light water research reactor
LWR	**L**ight **W**ater **R**eactor
NPP	**N**uclear **P**ower **P**lant
NRA	**N**uclear **R**egulation **A**uthority
PEEK	**P**olyether **E**ther **K**etone
PKA	**P**rimary **K**nock-on **A**tom
PLM	**P**lant **L**ife **M**anagement
PWR	**P**ressurized **W**ater **R**eactor
RBSM	**R**igid **B**ody **S**pring **M**odel
RIVE	**R**adiation-**I**nduced **V**olumetric **E**xpansion
RPV	**R**eactor **P**ressure **V**essel
SEM	**S**canning **E**lectron **M**icroscope
XRD	**X**-**R**ay **D**iffraction

Symbols

$\left(\frac{\Delta V}{V}\right)_{max}$	maximum RIVE of a mineral at a completely saturated state
$\frac{\Delta V}{V}$	relative volumetric expansion of a mineral
A_α	coefficient listed in Table 2.5.1
B_α	coefficient listed in Table 2.5.1
B_β	coefficient listed in Table 2.5.1
E_{max}	maximum energy of the neutron spectrum
E_{min}	minimum energy of the neutron spectrum
T_{max}	maximum energy transferred in a collision from moving particle to an atom at rest
T_{min}	minimum energy transferred in a collision from moving particle to an atom at rest
V_h	volume from helium pycnometry
V_d	volume from dimension measurements
β_0	coefficient listed in Table 2.5.1
ρ_h	density obtained from helium pycnometer
ρ_w	density obtained from water pycnometer
σ_{dpa}	energy dependent dpa cross-section
N	atom number density
R	number of displaced atoms per unit volume per unit time
T	temperature of irradiation
a	irradiation temperature-dependent parameter
b	irradiation temperature-dependent parameter
dpa	displacements per atom
p	porosity
s	time in seconds
α	irradiation temperature-dependent parameters
β	irradiation temperature-dependent parameters
σ	area for the collision resulting in transfer of energy
υ	number of defects per PKA
φ	neutron fluence rate spectrum

CHAPTER 1

Introduction

1.1 Nuclear energy infrastructure worldwide and plant life management

By the mid of 1939, scientists of the world had important theoretical knowledges in the field of nuclear physics, which made possible to start an extensive research program further. It turned out, that the uranium atom can be split into two parts. By this means a huge amount of energy releases. Moreover, fission reaction releases neutrons, which in turn can fission other uranium atoms and cause a nuclear chain reaction. The history of nuclear energy began in December 2, 1942, when for the first time a chain reaction of nuclear decay was carried out at the University of Chicago using uranium as a fuel and graphite as a moderator. Electrical energy from fission energy was generated on December 20, 1951 at Idaho National Laboratory using the Experimental Breeder Reactor-I (EBR-I) fast reactor. The world's first nuclear power plant (NPP) to produce electrical energy for a power grid started operation in 1954 in Obninsk, USSR. Since 1970s, massive construction of NPPs around the world has begun and by the beginning of July 2020, there are 408 nuclear reactors, excluding Long-Term Outages (LTO), operated by 31 countries.

According to the annual report of *World Nuclear Industry Status Report (WNISR)* (Schneider, 2020) as of 2020, nowadays there are 270 of operable reactors, two-thirds of them have been in service for 31 or more years (Figure 1.1.1). Moreover, out of 270 reactors, approximately 20% reaching 41 or more years. Some of them are even 80 years old. Usually, nuclear facilities are designed for 30-40 years of service life, however operational life can be extended on the framework of local authorities. For instance, in the US, each newly-build reactor licensed to operate for 40 years and could receive a license renewal for an additional 20 years from Nuclear Regulatory Commission (NRC) with unlimited number of renewals. In the European Union (EU) most of NPPs were constructed between 1970s and 1980s, therefore the assessment of soundness of reactor parts is the problem of modern days (ENSREG, 2018). Mean age of NPPs worldwide steadily grows due to the small number of newly built (Figure 1.1.2).

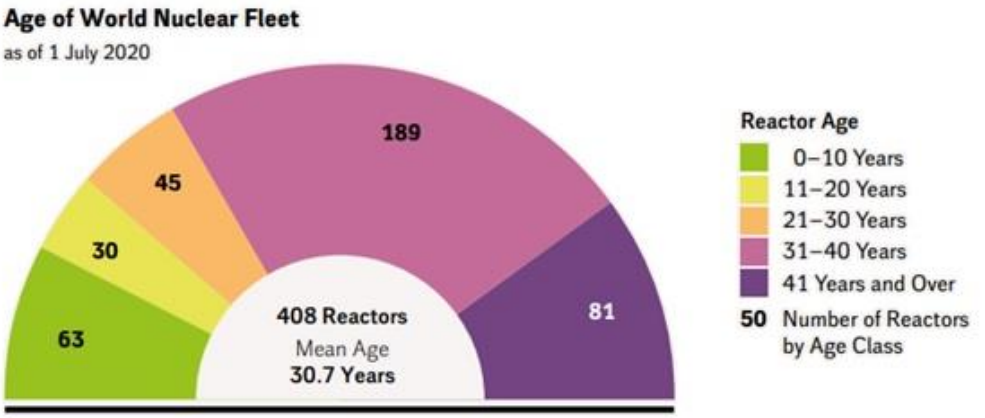

Figure 1.1.1. Age of world nuclear fleet (Schneider, 2020)

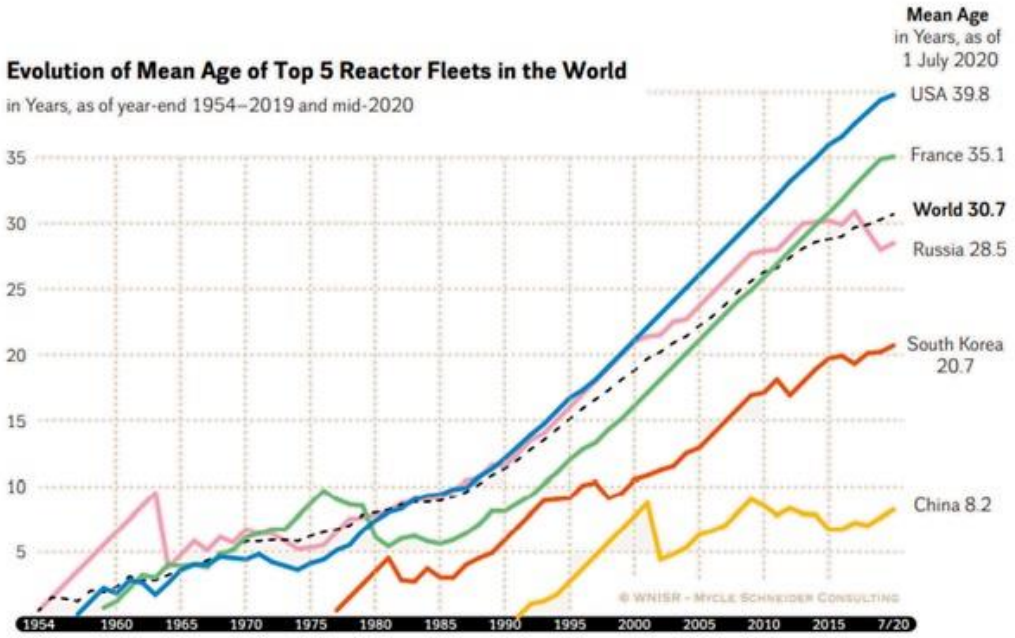

Figure 1.1.2. Evolution of mean age (Schneider, 2020)

According to World Nuclear Association (WNA) (World Nuclear Association, 2020), up until 2011, Japan was generating one-third of electricity from NPPs and at that time it was expected to increase production to at least 40%. However, after March 2011 Tōhoku earthquake and the following accident at the Fukushima Daiichi NPP, all of the existing Japanese reactors have had to get regulatory approval from the Nuclear Regulation Authority (NRA) within new stricter rules via so called Plant Life Management (PLM) examination. The PLM must be supervised for every 10 years after first 30 years of operation. An improved system evaluation method is developed through scientific researches to judge if each single NPP is sound or not. The license renewal is preferable over decommissioning since construction of new NPPs in future will be considerably difficult in Japan and reactor shut off is associated with high costs.

Table 1.1.1 includes Japanese NPPs currently under review of NRA as for August 2019. It should be noted that presented NPPs undergoes assessment based on many natural/technological factors and the soundness of every individual structure and machinery equipment.

Table 1.1.1. NPPs currently under NRA review (Uetaki, 2019)

NAME	AGE[1]	REACTOR	OWNER	OPERATOR
HAMAOKA-3	33	BWR	Chubu EPCO	Chubu EPCO
HAMAOKA-4	27	BWR	Chubu EPCO	Chubu EPCO
HIGASHIDORI-1	14	BWR	TEPCO	TEPCO
OHMA	Under constr.	ABWR	EPDC	EPDC
ONAGAWA-2	25	BWR	Tohoku EPCO	Tohoku EPCO
SHIKA-2	14	ABWR	Hokuriku EPCO	Hokuriku EPCO
SHIMANE-2	31	BWR	Chugoku EPCO	Chugoku EPCO
SHIMANE-3	Under constr.	ABWR	Chugoku EPCO	Chugoku EPCO
TOMARI-1	31	PWR	Hokkaido EPCO	Hokkaido EPCO
TOMARI-2	29	PWR	Hokkaido EPCO	Hokkaido EPCO
TOMARI-3	10	PWR	Hokkaido EPCO	Hokkaido EPCO
TSURUGA-2	33	PWR	JAPC	JAPC

1.2 Problem description

Among numerous types of construction materials, concrete possesses a good shielding property against ionizing radiation and used in nuclear power facilities, as it is well suited for long-term service life and has a high-temperature resistance.

Light Water Reactor (LWR) is considered as an important power supplier in Japan. There are two basic types of reactors: Boiling Water Reactor (BWR or Advanced BWR) and Pressurized Water Reactor (PWR; 2-loop and 3-loop). Concrete has found several of its applications in NPPs as a Concrete Biological Shielding (CBS) in case of PWR and as a support structure (pedestal) for Reactor Pressure Vessel (RPV) and CBS in case of BWR. In fact, concrete elements in plants are irreplaceable and requires a detailed research in order to keep a safe long-term

[1] as of 01.11.2020

operation. Extensive research on degradation mechanisms of reinforced concrete has been made for civil structures so far: steel rebar degradation due to corrosion and concrete degradation due to alkali-silica reaction, carbonation, chloride and sulfate attack, delayed ettringite formation etc. However, in application of NPPs the radiation environment created by a reactor vessel is another form of reinforced concrete degradation caused by a high-energy flux of neutron and gamma rays. Mainly, the mechanism of concrete deterioration under the ionizing radiation environment occurs via so-called radiation-induced volumetric expansion (RIVE) of aggregates and shrinkage of cement paste through radiation-induced radiolysis of free water and high temperature in reactor zone. The mutual effect of swelling of aggregates and contraction of cement paste is the main peril for crack formation, and, as a result, loss of bearing capacity takes a place, degradation of shielding properties and dynamic stability of structural elements.

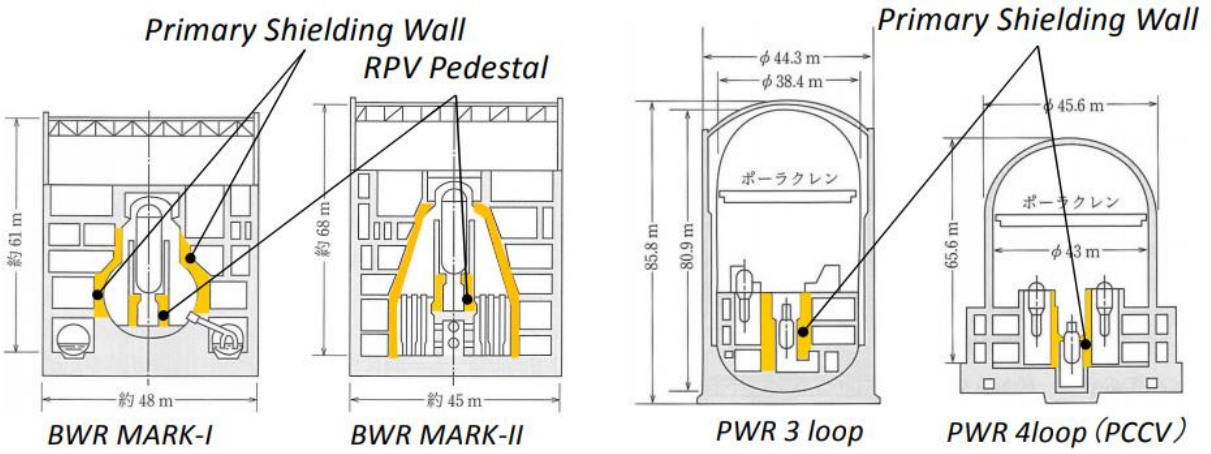

Figure 1.2.1. Section view of RPV pedestal and CBS of Japanese NPPs (Ishikawa, et al., 2017)

The effects of ionizing irradiation on mechanical properties of concrete have been concluded by Hilsdorf *et al.* (Hilsdorf et al., 1978). They have determined the threshold for decrease of the compressive strength of concrete under the impact of high-energy neutrons (E > 100 keV) above a fluence of 1×10^{19} n/cm^2 and the effect of gamma ray on the mechanical properties, particularly the energy dose above which such effects noticeable, is not sufficiently clarified, however Hilsdorf *et al.* have indicated comparative changes in properties beyond a dose of 5×10^5 kGy. The results show a good correlation with the output made by Dubrovskii *et al.* (Dubrovskii et al., 1966, 1967, 1968 1970), where the threshold was approximately estimated to be 5×10^{19} n/cm^2. Lately, Fujiwara *et al.* (Fujiwara et al., 2009) and Kontani *et al.* (Kontani et al, 2010) pointed out that output of experimental work, at some points, made by Hilsdorf *et al.*

was not suited for concrete members in LWRs. Maruyama *et al.* (Maruyama et al., 2013) then summarized the data applicable for LWRs, where they have indicated degradation of irradiated concrete after the neutron fluence of 1×10^{19} n/cm^2. Various sources (Dubrovskii et al. 1967) (Hilsdorf et al., 1978) (Kontani et al., 2010) (Maruyama et al, 2012) proposed that the main reason for concrete degradation is amorphization of siliceous rock-forming minerals (Elleuech, 1971) due to the neutron irradiation. The amorphization is caused by demolition of crystalline structure of minerals. As aggregate expands the cement matrix is crushed resulting in degradation of concrete's mechanical properties, such as Young's modulus and compressive/tensile strength.

Table 1.2.1. Forecasted values of neutron and gamma ray doses of NPPs in Japan after 60 years of operation (Maruyama et al., 2017)

NPP	Reactor	State	Place	Energy of neutrons	Neutron fluence [n/cm^2]	Gamma ray Dose [Gy]
Fukushima-1	BWR	Decomis.	Outside of RPV	≥ 0,1 MeV	3×10^{18}	$< 2 \times 10^{8}$
Fukushima-2					3×10^{18}	$< 2 \times 10^{8}$
Shimane-1					3×10^{18}	8×10^{7}
Tsuruga-1				≥ 1,0 MeV	1×10^{17}	$< 2 \times 10^{8}$
Fukushima-5			RPV pedestal structure	≥ 0,1 MeV	$2{,}8 \times 10^{14}$	$2{,}3 \times 10^{4}$
Hamaoka-1					$5{,}7 \times 10^{13}$	$1{,}6 \times 10^{4}$
Fukushima-3					$1{,}6 \times 10^{9}$	$2{,}2 \times 10^{5}$
Mihama-2	PWR	Decomis.	Inner part of the first CBS	≥ 0,11 MeV	$6{,}2 \times 10^{19}$	$1{,}8 \times 10^{8}$
Ikata-1		In oper.			6×10^{19}	$2{,}8 \times 10^{8}$
Genkai-1		Decomis.			$4{,}8 \times 10^{19}$	$2{,}8 \times 10^{8}$
Mihama-3		In oper.			$4{,}7 \times 10^{19}$	$2{,}5 \times 10^{8}$
Takahama-1					$4{,}5 \times 10^{19}$	$2{,}3 \times 10^{8}$
Takahama-2					$4{,}5 \times 10^{19}$	$2{,}4 \times 10^{8}$
Mihama-1		Decomis.			$3{,}6 \times 10^{19}$	$1{,}5 \times 10^{8}$

According to the Review Manual for Technical Evaluation of Aging Management (Japan Nuclear Energy Safety Organization, 2013), the soundness assessment of concrete elements under neutron and gamma ray irradiation is based on the reference levels of 1×10^{20} n/cm^2 and 2×10^{5} kGy respectively. If the reference levels were not exceeded after 60 years of operation,

then concrete elements were assessed as sound as designed. The threshold levels were obtained from the studies made by Hilsdorf *et al.* (Hilsdorf et al., 1978). Though they have indicated the fluence level of 1×10^{19} n/cm^2 as a starting point for concrete degradation and the effect of gamma ray irradiation was insignificant, however the reference levels do not correspond with the levels provided by Hilsdorf *et al.* (Maruyama et al., 2017). Table 1.2.1 includes the forecasted doses of irradiation for Japanese NPPs after 60 years of operation, where the neutron fluences are expected to be higher than the threshold values provided by Hilsdorf *et al.* (1×10^{19} n/cm^2). However, the reference level will be exceeded even after 40 years of operation.

According to Maruyama et al. (Maruyama et al., 2017), the cited literature used in Hilsdorf et al.'s experiments was studied in detail. Incompatibilities were pointed between concrete used in LWRs and the conducted experiments, such as cement type, temperature conditions, etc. (Kontani et al., 2010). Therefore, Japanese reference levels must be carefully revised by more in-detail experiments.

In this thesis, the effect of neutron irradiation on concrete aggregates is studied through available literature and concluded via experimental investigations.

1.3 Goals of master's thesis

The goals of the thesis as follows:

- To provide a general overview of the state of the art
- To explain an interaction between neutron irradiation and matter
- To provide a baseline characterization of investigated samples before and after irradiation by means of water and helium pycnometry, XRD, LOM, SEM+EDX, FTIR and RAMAN microscopy.
- To discuss and interpret the effect of neutron irradiation on test specimens
- To select the most suitable rocks as a part of concrete's aggregate for CBS structure

1.4 Structure of master's thesis

The structure of the thesis as follows:

- **Chapter 1. Introduction:** includes a basic information to introduce a reader into the problem
- **Chapter 2. State of the Art:** an overview of past/current available research, modern trends and gaps in knowledges
- **Chapter 3. Methodology:** a description of research methodology and important steps in procedure
- **Chapter 4. Procedure:** a detailed description of the procedure, equipment and used techniques at the Research Centre Řež
- **Chapter 5. Results and Discussions:** discussion of obtained results and comparison with the similar previously made research
- **Chapter 6. Conclusion:** includes summary of highlights discussed in Chapter 5
- **Chapter 7. References:** a list of cited literature

State of the art

2.1 Mechanism of radiation damage and subsequent defects

The radiation damage could be characterized as a transfer of energy of a moving particle to target atoms resulting in rearrangement of atoms inside a solid body. The damage is composed of different processes:

- The interaction of a moving particle with a lattice atom
- The excitation of a lattice atom by transfer of kinetic energy
- The excited atom travels within the body, also referred as the primary knock-on atom (PKA)
- The transition of the PKA through the body and creation of additional knock-on atoms
- The creation of a displacement cascade (a set of created point defects by the PKA)
- The termination of the PKA as an interstitial

The damage caused by radiation can only take a place if the energy, transferred to an atom at rest, is higher than the threshold displacement energy (the minimum kinetic energy required to cause displacement of an atom from its original site to a defect position) of the same atom. The result of the radiation damage is the collection of Frenkel pairs (vacancy-interstitial) and clusters.

The probability of interaction between two atoms is described by the cross-section of energy neutrons. It is measured in barns and the value varies depending on a chemical element.

The radiation damage is quantified as a number of displaced atoms per unit volume per unit time R.

$$R = N \int_{E_{min}}^{E_{max}} \int_{T_{min}}^{T_{max}} \varphi(E_i)\sigma(E_i, T)\upsilon(T)dTdE_i \quad (1)$$

where N is the atom number density, E_{max} and E_{min} are the maximum and minimum energies of the travelling particle, $\varphi(E_i)$ flux of particles with respect to energy, T_{max} and T_{min} are the maximum and minimum energies transferred in a collision from moving particle to an atom at rest, $\sigma(E_i, T)$ is the area for the collision resulting in transfer of energy, $\upsilon(T)$ is the number

defects per PKA.

According to Remec *et al.* (Remec et al., 2018), the total displacement per atom (dpa, number of times that an atom is displaced for a given fluence) is obtained as:

$$\frac{dpa}{s} = \int_0^{E_{max}} \sigma_{dpa}(E)\varphi(E)dE \qquad (2)$$

where E_{max} denotes the maximum energy of the neutron spectrum, $\sigma_{dpa}(E)$ is the energy dependent dpa cross-section and $\varphi(E)$ is the neutron fluence rate spectrum. With the help of Eq. 2, it is possible to assess dpa rates for NPPs and forecast emitted doses in function of time. It is also useful to assess the relative contribution of neutrons with energies higher than E_0 for a given neutron fluence rate spectrum.

$$\frac{\frac{dpa}{s}(E > E_0)}{\frac{dpa}{s}} = \frac{\int_{E_0}^{E_{max}} \sigma_{dpa}(E)\varphi(E)dE}{\int_0^{E_{max}} \sigma_{dpa}(E)\varphi(E)dE} \times 100 \qquad (3)$$

In the same study (Remec et al., 2018), the dpa rates (in the cavity) and dpa at 80 years of operation for some minerals were summarized in Table 2.1.1. It depends on a PWR type and material.

Table 2.1.1. Dpa rates and dpa in the cavity for PWR (Remec et al., 2018)

PWR	MINERAL	DPA RATE [S^{-1}]	DPA (80 YEARS)
2-LOOP	Quartz (SiO_2)	2,39E-11	0,055
	Calcite ($CaCO_3$)	1,90E-11	0,044
	Silicon (Si)	2,40E-11	0,056
	Anorthite ($CaAl_2Si_2O_8$)	2,22E-11	0,052
	Microcline ($KAlSi_3O_8$)	2,22E-11	0,052
	Albite ($NaAlSi_3O_8$)	2,40E-11	0,056
	Almandine ($Fe_3Al_2(SiO_4)_3$)	2,1E-11	0,049
	Fayalite (Fe_2SiO_4)	1,88E-11	0,044
3-LOOP	Quartz (SiO_2)	9,15E-12	0,021
	Calcite ($CaCO_3$)	7,29E-12	0,017
	Silicon (Si)	9,04E-12	0,021
	Anorthite ($CaAl_2Si_2O_8$)	8,51E-12	0,020
	Microcline ($KAlSi_3O_8$)	8,51E-12	0,020
	Albite ($NaAlSi_3O_8$)	9,20E-12	0,021
	Almandine ($Fe_3Al_2(SiO_4)_3$)	8,03E-12	0,019
	Fayalite (Fe_2SiO_4)	7,15E-12	0,017

2.2 Effects of radiation on concrete constituents

2.2.1 Interaction of gamma ray and concrete constituents

A gamma ray is a type of electromagnetic radiation of high frequency, whereas photons have high energy per particle, occurring from the radioactive decay of nuclei. The absorbed dose is the energy imparted by ionizing radiation in a volume element of a specified material divided by the mass of this volume element. The unit of an absorbed dose is a gray (J/kg): 1 Gy = 100 rad. There are three different principles by which high frequency photons interact with material's atoms: both photoelectric and photonuclear effect, Compton scattering and electron-positron pair production (Figure 2.2.1.1). To a lesser degree, photo-fission, Rayleigh scattering and Thomson scattering also takes a place. The most common type of interaction is photoelectric effect, where the energy of gamma rays is of the same order of magnitude as the energy of electrons related to nuclei. The high energy (above 0,5 MeV) proton is absorbed and causes the ejection of an orbital electron. On the other hand, in Compton scattering photon (mid-level energy) is not absorbed, but elastically scattered and electron is ejected. For electron-positron pair production, when the energy of gamma rays exceeds 1,02 MeV it transforms into a matter with a strong electric field of nucleus and acts as a catalyst in production of an electron and a positron.

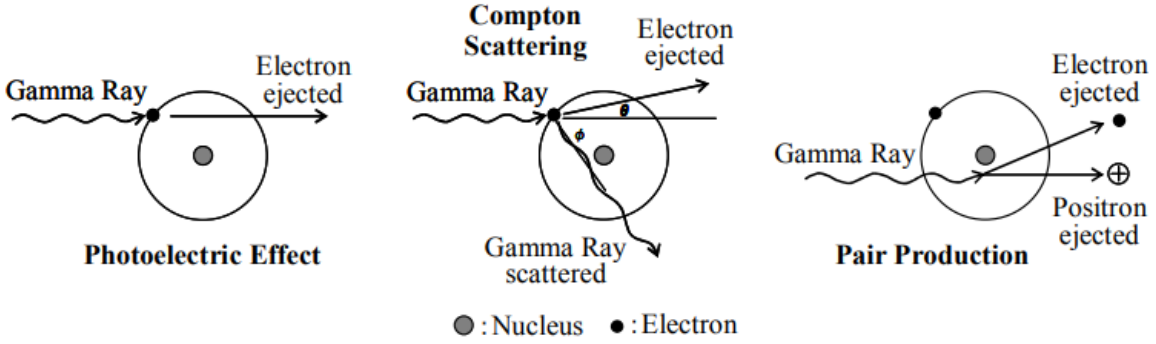

Figure 2.2.1.1. Photoelectric effect; Compton scattering; electron-positron pair production (Kontani et al., 2010)

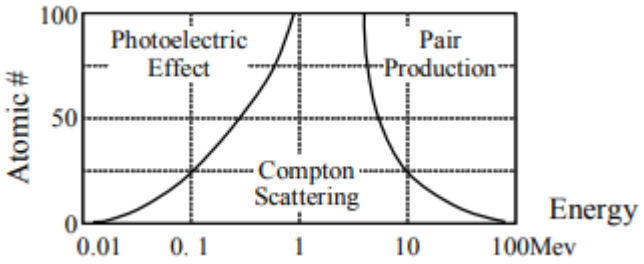

Figure 2.2.1.2. Interaction between gamma rays and an atom (Kontani et al., 2010)

Usually, LWRs emits gamma rays of energies between 100 keV to 10 MeV. Figure 2.2.1.2 shows the interaction of gamma rays and atomic number, in other words it marks which effect is dominant in dependence of energy and mass of an atom. Compton scattering is a dominant interaction with cement paste and aggregate, due to the atomic number usually found in particles of concrete. The emitted particles of electrons have a low energy and does not significantly affect solids; they decompose internal water via radiolysis effect, which, in return, produces free radicals and hydrogen peroxide, that reacts with cement paste (Bouniol, 1998) (Bjergbakke, 2008) (Caër, 2011). The possible effects of gamma rays are presented in Table 2.2.1.1.

Table 2.2.1.1 Impacts of gamma rays on concrete constituents (Maruyama et al., 2017)

		Gamma ray
Cement paste	Water	• Cement paste properties might change due to radiolysis and gamma heating • Products of decomposition (hydrogen peroxide and free radicals) might alter properties of cement paste
	Solid	• Gamma heating causes shrinkage • Hydrates are decomposed due to gamma heating • Drying changes mechanical properties • Si-O-Si bond is deformed by radiolysis and ballistic impact of electron • Si-O-Si bond and oxide atoms knocked out by kinetic impact of electron • Defects are healed by excess of water by solution-precipitation process
Aggregate	Water	• Gamma heating evaporates free water • Crystal water is released by gamma heating • Clay minerals and other layered structures shrinks due to drying
	Solid	• Volume change occurs through metamictization[2] of Si-O-Si bound • Deformation and metamictized state are healed by thermal effect • Secondary electrons knock out some atoms

[2] Is a process of complete destruction of mineral's crystal structure, leaving the mineral amorphous

It should be emphasized, that the cement properties might significantly change beyond the threshold of 200 MGy of the absorbed gamma ray dose, however, it is questionable. Decomposition of hydrates can take a place within the absorbed gamma ray dose of 130 to 836 MGy (Lowinska-Kluge & Piszora, 2008). On the other hand, concrete aggregates are insignificantly affected by gamma rays (Hilsdorf et al., 1978) and gamma rays are of a lesser importance in this research. However, a lack of available data on gamma ray – concrete interaction is an incentive for further investigations (Khmurovska, 2019).

According to McDowall (McDowall, 1972), gamma irradiated concrete tends to creep less than non-irradiated, but shrinks to a greater degree. Such trend considered anomalous assuming that the shrinkage of the irradiated concrete specimens indicates a drying-out process via radiolysis of water content in concrete.

2.2.2 Interaction of neutron radiation and concrete constituents

Interaction of neutron radiation and material generally can be classified into two groups, scattering and absorption. Scattering, in its turn, is categorized by the character of collision, elastic and inelastic. The type of interaction depends on neutron energy. The unit of neutron energy is electronvolt [eV] 1 eV = $1{,}602176634\times10^{-19}$ J. It is the amount of kinetic energy gained by a single electron accelerating from rest through an electrical potential of one volt in vacuum. Usually, keV and MeV are used to describe a radiation field. The terms *neutron flux* and *neutron fluence* are used to describe the effects of irradiation on matter. The *neutron flux* is defined as a relation of a number of neutrons *dN* travelling through a sphere per unit of time to cross-sectional area *dS*; the *neutron fluence* is obtained by integration of neutron flux over a certain period of time. The units used in the majority of the similar studies are $cm^{-2}s^{-1}$ and cm^{-2} respectively. Another important term is the *neutron spectrum*. It is defined as an energy distribution of radiation particles in dependence of the number of particles per certain energy interval.

Neutrons are classified by their kinetic energy in approximate values, since there are no exact values of the thresholds. The ranges of energy values are provided in Table 2.2.2.1 (Charit, 2013).

Table 2.2.2.1. Classification of neutrons according to Charit (Charit, 2013)

Type	Cold	Thermal	Epithermal	Intermediate	Fast	Relativistic
Energy	<0,003 eV	0,003 – 0.4 eV	0,4 – 100 eV	100 eV – 200 keV	200 keV – 10 MeV	>10 MeV

Hilsdorf (Hilsdorf et al., 1978) used the following classification (Table 2.2.2.2) in his work, where thermal neutrons have energies less than 1 eV, epithermal (intermediate) neutrons lie in the range from 1 eV to 0,1 MeV, and fast neutrons have energies above 0,1 MeV. The reference levels could be explained by the mechanism of interaction.

Table 2.2.2.2. Classification of neutrons according to Hilsdorf (Hilsdorf et al., 1978)

Type	Thermal	Intermediate	Fast
Energy	< 1 eV	1 eV – 0,1 MeV	> 0,1 MeV

It is also necessary to include the classification according to Denisov since the largest data of irradiation effects was obtained in the USSR, and recently collected and published in Russian literature (Table 2.2.2.3).

Table 2.2.2.3. Classification of neutrons according to Denisov (Denisov et al., 2012)

Type	Cold	Thermal	Epithermal	Intermediate	Fast	Superfast
Energy	< 0,005 eV	0,005 – 0,1 eV	0,1 – 500 eV	500 eV – 200 keV	200 keV – 20 MeV	> 20 MeV

When a fast neutron collides with a nucleus it is absorbed and a new unstable compound nucleus is created, which in return decays releasing in random paths one or more gamma rays (secondary gamma ray) and a neutron. The secondary gamma rays produce electrons and generate electronic excitation by electron-positron pair production and Compton scattering. Produced electrons are then absorbed by atoms as thermal vibrations. A fast neutron is absorbed for a relatively small amount of time and, since the new compound nucleus is unstable, it released with the change of direction. Such interaction is called inelastic scattering and will continue until the fast neutron becomes intermediate. An intermediate neutron interacts elastically as it does not have sufficient energy to be absorbed, thus does not release gamma rays. After the collision, nucleus ejects a neutron in different direction. This interaction is called elastic scattering. Since each collision causes loss of neutron's kinetic energy, the process is repeated until the intermediate neutron becomes thermal. The energy of a thermal neutron is absorbed after the collision without the release of neutron nor gamma particles.

Both inelastic and elastic scattering are depicted in Figure 2.2.2.1.

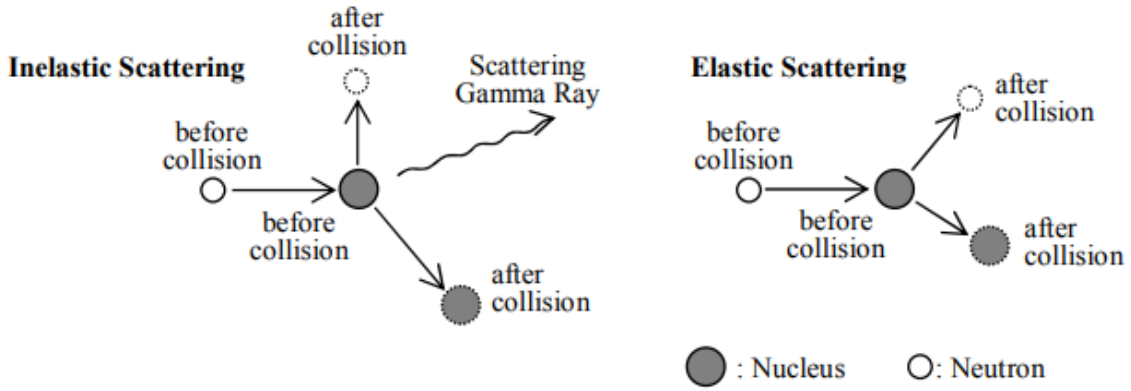

Figure 2.2.2.1. Inelastic and elastic scattering before and after collision (Kontani O., 2010)

When minerals are subjected to high-energy neutron flux, an atom in crystalline structure is displaced leaving a vacant lattice site called *vacancy (Schottky effect)*; the displaced atom comes in rest and is called *interstitial* (illustrated in Figure 2.2.2.2). The effect of interaction of an atom and travelling neutron is called *ballistic effect*; and a pair of vacancy and interstitial is called a *Frenkel pair*.

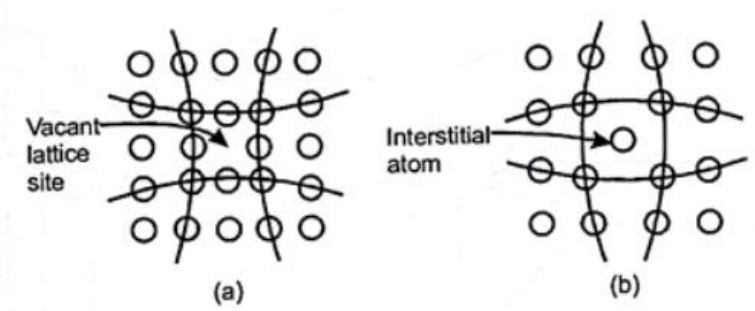

Figure 2.2.2.2. Vacancy and interstitial lattice defects (Kontani et al., 2010)

Development of Frenkel pairs is leading to metamictization process (amorphization) which alters properties of minerals, such as density, volume, modulus of elasticity, thermal conductivity (Gray, 1971), and stops once saturation is reached. Additional metamictization might be caused by secondary gamma rays. While a created vacancy causes contraction of minerals, an interstitial atom contributes in expansion in a much higher degree (Denisov et al., 2012). This effect is called *radiation-induced volumetric expansion* (RIVE). The reference level of neutron's energy to cause considerable changes in lattice structured minerals is equal to 10 keV, according to Denisov *et al.* (Denisov et al., 2012).

The neutrons have a more significant effect on crystalline structure of minerals or aggregates rather than on predominantly amorphous structure of cement paste. Moreover, a cement paste

has a high porosity (pore volume about 20 % of calcium silicate hydrate) and does not accumulate enough damage to alter its properties. The reference level of neutron's energy to cause a significant damage is higher and has a value of more than 0,8 MeV. It should be emphasized, that a neutron flux can initiate radiolysis of free water producing hydrogen, oxide and hydrogen peroxide, which in return might alter the properties. The reaction will cause shrinkage of cement paste and clay minerals (Maruyama et al., 2017).

The effect of neutron irradiation on creep of concrete is not fully investigated. According to research made by Gray (Gray, 1971), it appeared to be insignificant, however, the final result is controversial. Denisov (Denisov et al., 2012) has explained an increased creep by a high temperature in test reactor and its rate was equivalent to the rate of temperature.

The possible effects of neutron radiation on cement paste and aggregates are summarized in Table 2.2.2.4.

Table 2.2.2.4. Impacts of neutron rays on concrete constituents (Maruyama et al., 2017)

		Neutron radiation
Cement paste	Water	• Cement paste properties might change due to radiolysis and gamma heating • Products of decomposition (hydrogen peroxide and free radicals) might alter properties of cement paste
	Solid	• Calcium silicate hydrate has an amorphous structure, the irradiation damage is negligible • Defects in C-S-H are healed by solution-precipitation of water
Aggregate	Water	• Gamma heating evaporates free water • Crystal water is released by gamma heating • Clay minerals and other layered structures shrinks due to drying
	Solid	• Crystalline structure of minerals is destroyed by neutrons • Metamictized minerals partly healed by thermal effect • Some minerals are expanded by reordering of atoms • α-quartz shows the largest expansion • Additional metamictization is caused by secondary gamma rays

2.2.3 Mechanism of concrete deterioration

As it was mentioned above, the main mechanism of concrete deterioration under ionizing radiation is caused by the mutual effect of swelling of aggregates due to RIVE and shrinkage of cement paste due to radiation-induced radiolysis of water. Concrete is a composite material which mainly consists of aggregates (approximately 70% of volume fraction) typically of fine and coarse sizes, which, in return, formed by minerals.

Development of cracks around concrete aggregates under gamma ray irradiation primarily caused by shrinkage of cement paste via drying and heating. Initially, crack formation more likely will appear along the weakest paths known as the ITZ. Strength changes of concrete primarily appear due to differential expansion, where aggregates tend to swell due to metamictization creating microcracks inside and between minerals contributing to even larger expansion, and cement paste tend to contract.

The possible phenomena of structural changes are summarized by Maruyama *et al.* (Maruyama et al., 2017) in Table 2.2.3.1.

Table 2.2.3.1. Possible phenomena of concrete degradation under gamma and neutron irradiation (Maruyama et al., 2017)

	GAMMA RAY	NEUTRON RADIATION
CONCRETE	• Crack development around aggregates due to drying and heating • Unreacted parts of cement react under elevated temperature caused by thermal vibrations • Change in strength due to colloidal and porous media of cement paste, and cracking of concrete due to differential volumetric expansion of mortar and aggregate • Degradation of Young's modulus	• Expansion of aggregates due to metamictization • Crack formation in cement paste due to restraint by aggregates • Crack formation and crack openings causes degradation of strength and Young's modulus

2.3 Structural groups of aggregate-forming minerals

As it was mentioned earlier, neutron irradiation has a large influence on aggregates. Therefore, it is necessary to distinguish the composition of them. Usually, aggregates are polymineralic rocks composed of minerals. Minerals, in return, show different swelling under irradiation as they have various structure, chemical composition, density, nuclear density (the density of

nucleus of an atom) and heat of fusion (quantity of heat required to change 1 g of a crystalline solid to a liquid without temperature change).

According to their chemical composition, minerals are divided into many classes. The main minerals that make up building materials belong to the classes of silicates, carbonates and oxides. The division of silicate group of minerals into structural types is based on the following. In the structure of most minerals, isolated spatial or planar groups of atoms can be distinguished, which are interconnected either by shared atoms or through additional ions. Depending on the degree of quartz polarization, the following types of structures of minerals are distinguished according to Denisov *et al.* (Denisov et al., 2012):

Nesosilicates (Island silicates) – groups of atoms are not linked by common atoms. Connection between them is through additional ions.

Inosilicates (Single and Double chain silicates) - groups of atoms are linked into chains and ribbons by shared atoms. The link between chains and ribbons is through additional ions.

Phyllosilicates (Sheet silicates) - structures in which groups of atoms are linked by sharing of atoms into flat endless layers.

Tectosilicates (Framework silicates) - structures in which groups of atoms are linked by shared atoms into a three-dimensional flat endless framework.

2.3.1 Silicate mineral class

The basis of the structure of minerals of silicates are silicon-oxygen tetrahedra SiO_4^{4-}, an atom of silicon is located at the center, and atoms of oxygen are located at the vertices. Structure of silicates is distinguished depending on the method of connection between these tetrahedrons. Atom of aluminium can replace an atom of silicon. Then the composition of silicates includes cations of various metals and silicates, therefore the silicates are called aluminosilicates (Denisov et al., 2012).

The main framework silicates found in building materials:

- Modifications of silica SiO_2 with a framework $[SiO_2]_\infty$ differing in the degree of symmetry. Typical examples are quartz, tridymite, cristobalite and coesite.
- Feldspars with a framework $[(Si, Al)_4O_8]_\infty$ + Na, K, Ca, which include: potassium feldspars $KAlSi_3O_8$ (microcline, orthoclase and sanidine); plagioclases as solid solutions of albite $NaAlSi_3O_8$ and anorthite $CaAl_2Si_2O_8$ (albite, oligoclase, andesine,

labrador, bitovnite, anorthite with different fraction albite and anorthite)

- Feldspathoids. Typical examples are nepheline $Na_3KAl_4Si_4O_{16}$, leucite $KAlSi_2O_6$ and analcime $NaAlSi_2O_6H_2O$.

The main sheet silicates found in building materials:

- Micas or aluminosilicates of complex composition with a small the amount of OH hydroxyl with layers of $[Si_3AlO_{10}]$ + $(OH)_2$ + K, Al, Mg + Fe. Typical examples are muscovite - potassium (K, Al) mica, phlogopite - potassium-magnesium (K, Mg) mica and biotite - potassium-magnesium-ferruginous (K, Fe + Mg) mica.
- Serpentines, distinguished as various hydrous minerals of composition $Mg_3[Si_2O_5](OH)_4$.
- Chlorites, distinguished as water-bearing magnesian-ferruginous aluminosilicates of complex composition.

The main single chain silicates found in building materials:

- Pyroxenes with chains $[(Si, Al)_2O_6]_\infty$ + Ca, Mg, Fe. Typical examples are enstatite, hypersthene, diopside, hedenbergite, aegirine, augite and wollastonite.

The main double chain silicates found in building materials:

- Hornblendes which are complex compositions of water-containing aluminosilicates - $Ca_2Na(Mg, Fe^{2+})_4(Al, Fe^{3+})[(Si, Al)_4O_{11}]_2[OH]_2$.

The main island silicates found in building materials:

- Minerals of composition $(SiO_4)_\infty$ + Mg, Fe. Typical examples are forsterite Mg_2SiO_4, fayalite Fe_2SiO_4, olivine $[Mg, Fe]_2SiO_4$, monticellite $CaMgSiO_4$ and zircon $ZrSiO_4$.

The content of SiO_2 in minerals decreases with the transition from framework to sheet, single chain and double chain minerals and further to island minerals. This increases the density, nuclear density (density of the nucleus of an atom), temperature and heat of fusion of minerals (Denisov et al., 2012).

2.3.2 Carbonate mineral class

Minerals of the carbonate class have a low thermal stability. These minerals do not melt when heated, but decompose to form oxide and release carbon dioxide. The least thermally stable minerals are siderite (decomposes at 280-450 ° C) and magnesite (decomposes at 375-540 ° C). Calcite and dolomite decompose at a temperature of about 900 ° C. The structure of carbonate

class minerals is based on planar groups of CO_3^{-2} atoms.

The main minerals of the carbonate class that are part of building materials are island carbonates. Typical examples are calcite $CaCO_3$, magnesite $MgCO_3$, siderite $FeCO_3$, dolomite $CaMg[CO_3]_2$ and ankerite (ferrous dolomite) $(Ca[Mg, Fe][CO_3]_2$.

2.3.3 Oxide mineral class

The class of oxide minerals includes those minerals in which the oxide anion is bonded to one or more metal alloys. Hydroxide-containing minerals usually fall into the class of oxides.

The main minerals of the class of oxides that make up building materials are:

- Sheet minerals such as corundum Al_2O_3 and hematite Fe_2O_3.
- Spinel minerals such as spinel $[Mg, Fe]Al_2O_4$, chromite $[Mg, Fe]Cr_2O_4$ and magnetite Fe_3O_4.

2.4 Radiation-induced volumetric changes

The radiation-induced volumetric changes of minerals, aggregates, cement paste and concrete, as a whole, were summarized by Khmurovska and Štemberk (Khmurovska & Štemberk, 2019) based on the extensive literature review. The radiation-induced swelling or contraction discussed in main patterns according to concrete phases and constituents of aggregates.

2.4.1 Volumetric expansion of minerals

As it was mentioned earlier, the threshold level to cause RIVE of minerals is assumed to be 1×10^{19} n/cm^2. However, it is also important to account for energy levels of the neutrons (Denisov et al., 2012), since the type of particle interaction depend on them (Kontani et al., 2010) following with the creation of defects, mainly Frenkel pairs. These energy level neutrons are characterized by neutron spectrum. The spectrum with the higher amount of high energy neutrons is called the *hard spectrum*, and the spectrum with the lower amount of high energy neutrons is called the *soft spectrum* (Figure 2.4.1.1 (a)). The hard spectrum produces more lattice defects than the soft spectrum (Figure 2.4.1.1 (b)).

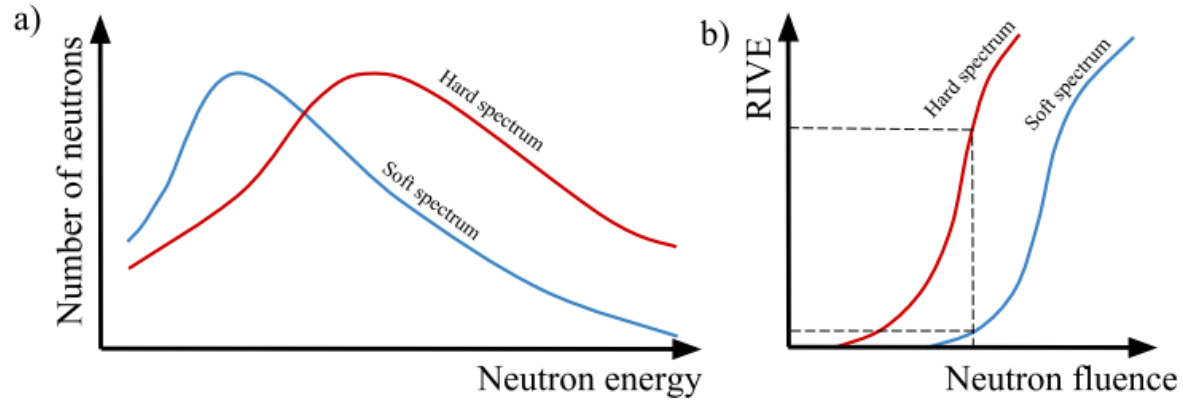

Figure 2.4.1.1 Hard and soft spectrums a) Spectrum division b) Effect on RIVE (Khmurovska & Štemberk, 2019) (Dubrovskii et al., 2010)

Approximately 400 of RIVE data was collected and recently published in Russian literature (Denisov et al., 2012). It was noted, that the metamictization process also depends on the temperature of irradiation. The high temperature of irradiation could lead to recombination of lattice defects. Therefore, some lattice defects could be annealed by heating. According to the experimental work conducted by Bykov *et al.* (Bykov et al., 1981), the higher temperature basically slows down the process of metamictization and, hence, the expansion (Figure 2.4.1.2 (a) and (b)). Generally, the temperature on the inner and outer surface of a CBS wall is around 60° C and 45° C respectively, which could be considered as low temperatures with the higher rate of expansion.

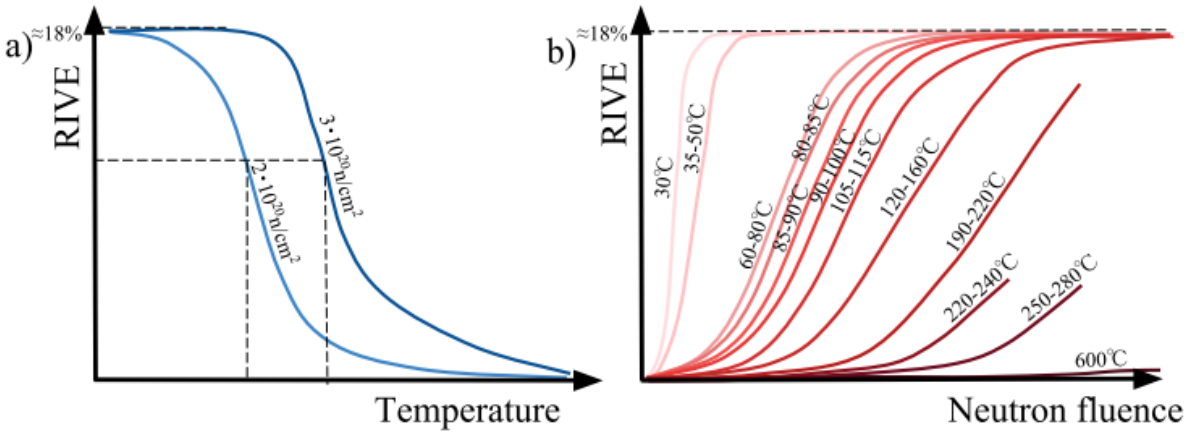

Figure 2.4.1.2 Temperature dependent RIVE a) Various fluence b) Various temperature (Khmurovska & Štemberk, 2019) (Dubrovskii et al., 2010)

The RIVE greatly depends on the type of minerals. The most important features of minerals are (Denisov et al., 2012): chemical composition, which make it possible to divide minerals by classes; microstructure, according to which minerals are divided into structural types and corresponding subclasses; unit cell parameters of the space lattice, characterizing the

dimensions and symmetry of the elementary volume lattice, reflecting the structure of the mineral: linear parameters - the dimensions of the sides (main axes) of the unit cell a, b and c; angular parameters - angles α, β, γ between the axes; appearance; and physical properties. Generally, the RIVE is higher with the larger content of α-quartz (quartz or SiO_2). The highest volumetric expansion was observed for sheet silicates with the largest content of α-quartz and recorded as high as 17,9 %. With the reduced content of α-quartz in the feldspar group the RIVE is reduced to 8 %. Moreover, it was noted that with the lower silicate degree of polymerization, the RIVE is also reduced. In descending order from framework silicates, to sheet silicates (up to 5 % for micas), further to chain silicates (up to 2,8 % for double-chain silicates and up to 1,5 % for single-chain silicates) and closing with the island silicates (up to 0,9 % for olivine) (Figure 2.4.1.3) (Khmurovska & Štemberk, 2019).

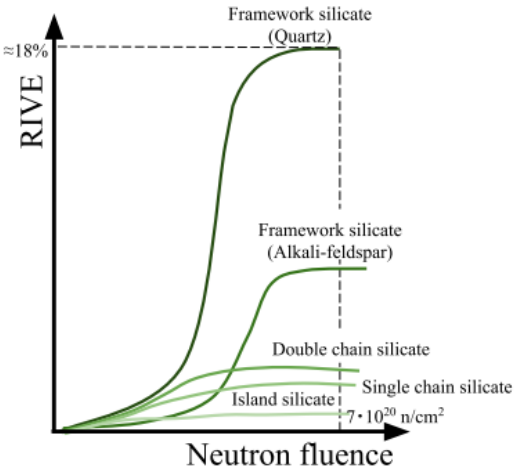

Figure 2.4.1.3. Structural groups of minerals and the corresponding RIVE (Khmurovska & Štemberk, 2019) (Dubrovskii et al., 2010)

It was also mentioned that the volumetric expansion is typically higher for silicates with lower nuclear density than for carbonates, which vary in the range from 0,5 to 4 % and higher with the complexity of structure and lower with the degree of structural symmetry. Moreover, another important factors to take into account are the phase transformation energy of minerals called heat of fusion (Denisov et al., 2012) and the energy required for a chemical bond dissociation in minerals called bond-dissociation energy (Le Pape et al., 2018). The RIVE in these cases is higher with the lower heat of fusion and lower with the lower bond-dissociation energy (Khmurovska & Štemberk, 2019).

2.4.2 Volumetric expansion of aggregates

Since aggregates are basically represented as a compound of different minerals it is necessary to account for each of them (Figure 2.4.2.1). However, the total volumetric expansion of aggregates is higher than the total RIVE of minerals. Such phenomenon could be explained by the complex stress state caused by differential swelling of minerals (Khmurovska & Štemberk, 2019). Therefore, the total RIVE of aggregates must also include the total volume of crack openings between minerals and crack formation in minerals. Hence, the RIVE of aggregates is higher than the total RIVE of minerals up to 23 %. Moreover, it was noted that the volumetric expansion is higher for coarse-grained aggregates rather than for fine-grained aggregates (Denisov et al., 2012).

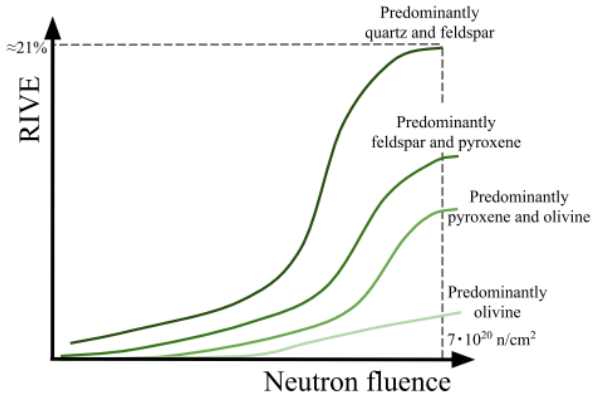

Figure 2.4.2.1. The total RIVE for aggregate groups (Khmurovska & Štemberk, 2019) (Dubrovskii et al., 2010)

Another noteworthy fact is that completely amorphous phase in aggregates tends to contract under neutron radiation. For example, according to Denisov *et al.* (Denisov et al., 2012), quartz glass exhibit radiation-induced volumetric contraction and, hence, cause formation of regions with contraction in aggregates. As it was discussed earlier, the degree of crystallinity of minerals should be taken into account prior assessing the possible volumetric changes.

2.4.3 Radiation-induced shrinkage of cement paste

The cement paste phase in concrete is predominantly represented as an amorphous phase, since the main component of cement paste is the *calcium silicate hydrate* (C-S-H) which is by nature is amorphous. In the experiments conducted by Denisov *et al.* (Denisov et al., 2012), cement paste exhibited contraction nearly 9,5 % at the irradiation temperature 400° C (Figure 2.4.3.1). It was explained by the process of hydrate decomposition and radiation-induced

radiolysis of free and chemically bounded water (up to 64 %) resulting in large release of gases, such as hydrogen and oxide.

Generally, the radiation-induced contraction of cement paste is higher with the higher fluence and the harder spectrum of neutrons showing similarities with the effect on minerals. The increased temperature contributed in slowing down the swelling of minerals by the annealing process, however, in the case of cement paste, the elevated temperature contributed in drying shrinkage (Khmurovska & Štemberk, 2019).

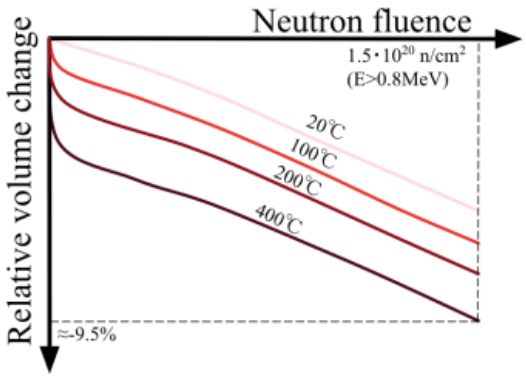

Figure 2.4.3.1. Volumetric contraction of cement paste (Khmurovska & Štemberk, 2019)

2.4.4 Volumetric and strength changes of concrete

Since concrete is a three-phase (aggregates, cement paste and ITZ, sometimes porosity is also included) composite material, an assessment of the total deformation is based on the assessment of every individual phase. Therefore, the overall RIVE of concrete could be judged based on amount, proportion, type and structure of present minerals in aggregates, composition, age and structure of cement paste. Relative strength and relative Young's modulus (post-irradiation value/initial value) are introduced to describe the degradation process with respect to fluence in Figure 2.4.4.1.

As it was mentioned earlier, the RIVE of concrete is leading to degradation of physical properties as performance of each phase is subjected to deterioration regardless to some beneficial points, such as partial healing of metamictized minerals by thermal effect, healing of C-S-H by solution-precipitation of water, and creep. Basically, deterioration due to RIVE is overestimated without the contribution of creep. However, the effect of creep of concrete under irradiation is not clarified yet.

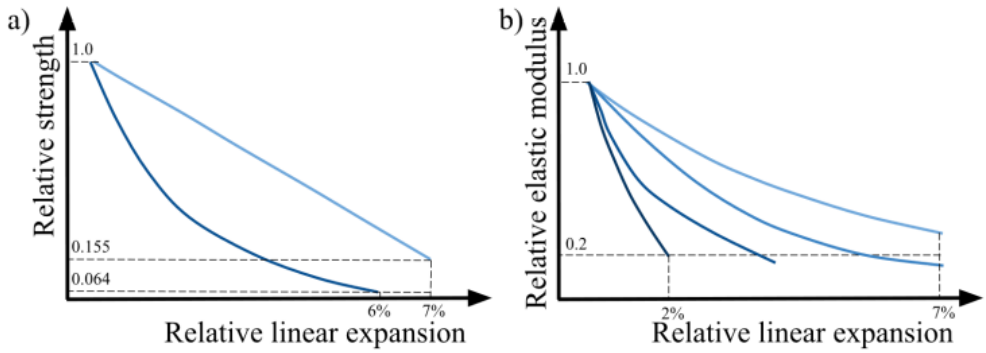

Figure 2.4.4.1. Degradation of concrete's physical properties with various composition a) Relative strength b) Relative elastic modulus (Khmurovska & Štemberk, 2019)

2.5 Analytical model for radiation-induced volumetric expansion of minerals

Based on extensive experimental work with irradiated minerals, Denisov *et al.* (Denisov et al., 2012) proposed an analytical model for mineral growth. In this model, displacements per atom (dpa) varies from 0 to 5. The total RIVE of minerals could be forecasted based on the following expressions:

$$\frac{\Delta V}{V} = \begin{cases} \dfrac{a(T)\left(\frac{\Delta V}{V}\right)_{max}\left(e^{b(T)dpa}-1\right)}{\left(\frac{\Delta V}{V}\right)_{max} a(T)e^{b(T)dpa}} & when\ a(T) \neq \infty\ and\ \beta(T) \neq 0 \\ \left(\frac{\Delta V}{V}\right)_{max}\left(1-e^{-b(T)dpa}\right) & when\ a(T) = \infty\ and\ \beta(T) = 0 \end{cases} \quad (4)$$

where $\frac{\Delta V}{V}$ [%] is the relative volumetric expansion of a mineral. $\left(\frac{\Delta V}{V}\right)_{max}$ [%] is the maximum RIVE of a mineral at a completely saturated state. $a(T)$ and $b(T)$ are the irradiation temperature-dependent parameters determined by the formulas:

$$a(T) = \frac{\alpha(T)}{\beta(T)} \quad (5)$$

$$b(T) = \beta(T)\left(\frac{\Delta V}{V}\right)_{max} + \alpha(T) \quad (6)$$

where $\alpha(T)$ and $\beta(T)$ are also the irradiation temperature-dependent parameters and could be described within the temperature range from 30° C to 270° C by the formulas:

$$\alpha(T) = A_\alpha \exp\left(\frac{B_\alpha}{T}\right) \quad (7)$$

$$\beta(T) = (A_\beta + B_\beta T)^{-1} + \beta_0 \quad (8)$$

where A_α, B_α, B_β and β_0 are the coefficients listed in Table 2.5.1; T [° K] is the average

irradiation temperature over the period of exposure.

Though the model reflects mineral growth with the correlation 95 %, it does not take into account volume expansion inside minerals caused by crack formation. Also, in case of polymineralic aggregates, additional swelling between grains of minerals due to uneven volumetric expansion must be taken into account.

Table 2.5.1. Parameter values for some minerals (Denisov et al., 2012)

Mineral	$\frac{\Delta V}{V}$ [%]	$-\ln A_{\alpha}$ [−]	$B_{\alpha}, 10^{3}$[°K]	$-A_{\beta}$[%]	$B_{\beta}, 10^{-2}$[% ∗ °K^{-1}]	β_0[%$^{-1}$]
Quartz	17,9	13,12	3,96	10,8	3,65	0,4
Tridymit	3,0	15,0	4,2	1,8	0,63	2,3
Cristobalite	6,0	16,1	4,8	3,7	1,2	1,2
Potassium feldspars	7,7	15,58	4,74	6,3	2,11	1,1
Albite	9,7	15,1	4,41	8,2	2,76	0,74
Oligoclase	7,0	14,8	4,41	5,9	1,99	1,03
Labrador	4,5	13,8	4,2	3,2	1,1	1,6
Anorthite	2,5	12,8	4,2	1,5	0,51	2,8
Nepheline	10,0	14,0	4,2	6,1	2,1	0,7
Leucite	2,0	15,7	4,2	1,2	0,4	3,50
Analcime	4,0	13,6	4,2	4,3	1,4	1,0
Muscovite	15,0	12,7	4,2	20,0	7,6	0,19
Biotite	15,0	14,4	4,2	9,1	3,1	0,46
Chlorite	1,5	12,3	4,2	0,61	0,21	7,0
Serpentine	2,0	11,38	4,2	1,2	0,4	3,5
Enstatitis	2,75	10,3	3,92	2,4	0,79	3,25
Diopside	2,75	10,3	3,92	2,4	0,79	3,25
Calcite	0,4	-3,7	0	∞	0	0
Magnesite	0,7	-3,0	0	∞	0	0
Dolomite	0,8	-3,0	0	∞	0	0
Ankerite	3,3	-1,28	0	∞	0	0
Periclase	1,2	-0,9	0	∞	0	-1,9
Chromite	1,0	-0,69	0	∞	0	0
Ilmenite	0,8	-0,9	0	∞	0	0
Corundum	1,8	0	0	∞	0	0,3
Hematite	0,9	-1,8	0	∞	0	0
Magnetite	0,6	-1,2	0	∞	0	0
Quartz glass	-3,0	-3,6	0	∞	0	0

Figures 2.5.1 and 2.5.2 represent volumetric expansion of few common minerals at irradiation temperature 60° C according to the model.

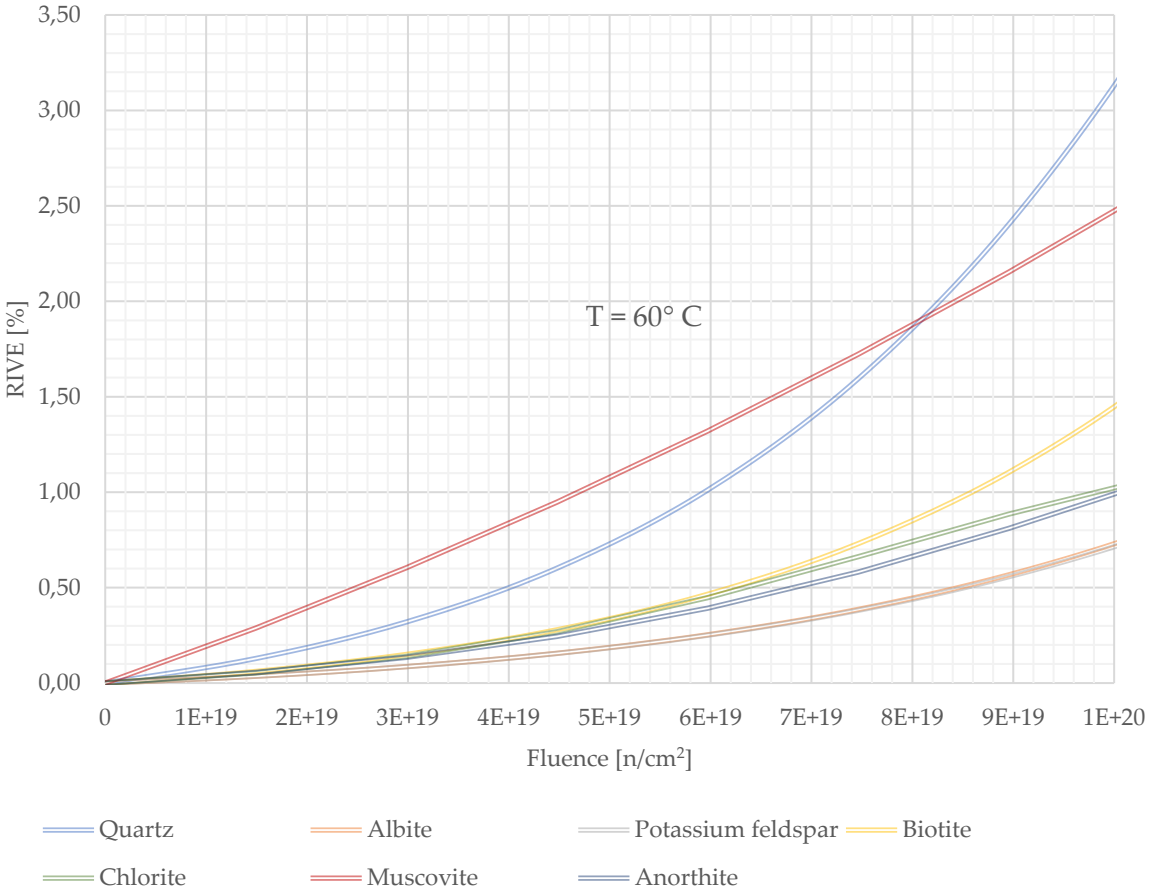

Figure 2.5.1. Volumetric expansion of selected minerals at 60° C (Denisov et al., 2012)

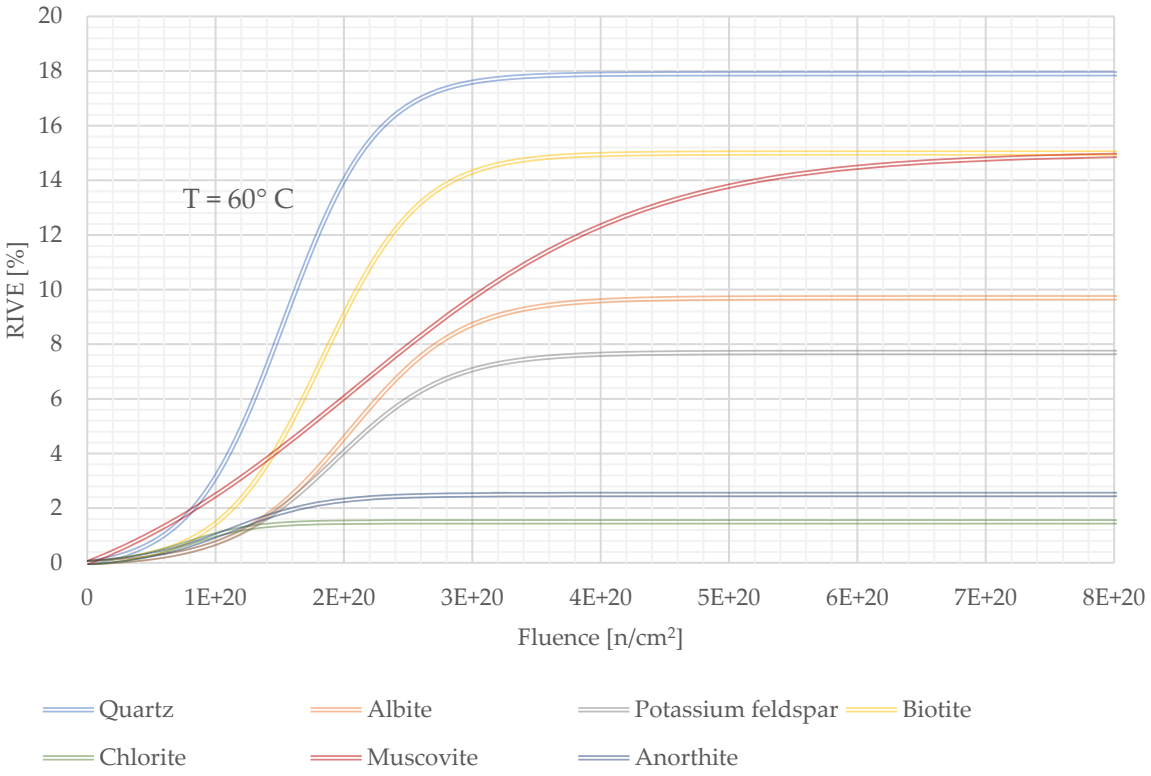

Figure 2.5.2. Volumetric expansion of selected minerals at 60° C (Denisov et al., 2012)

Figure 2.5.3 represent volumetric contraction of amorphous quartz glass at 60° C according to the model.

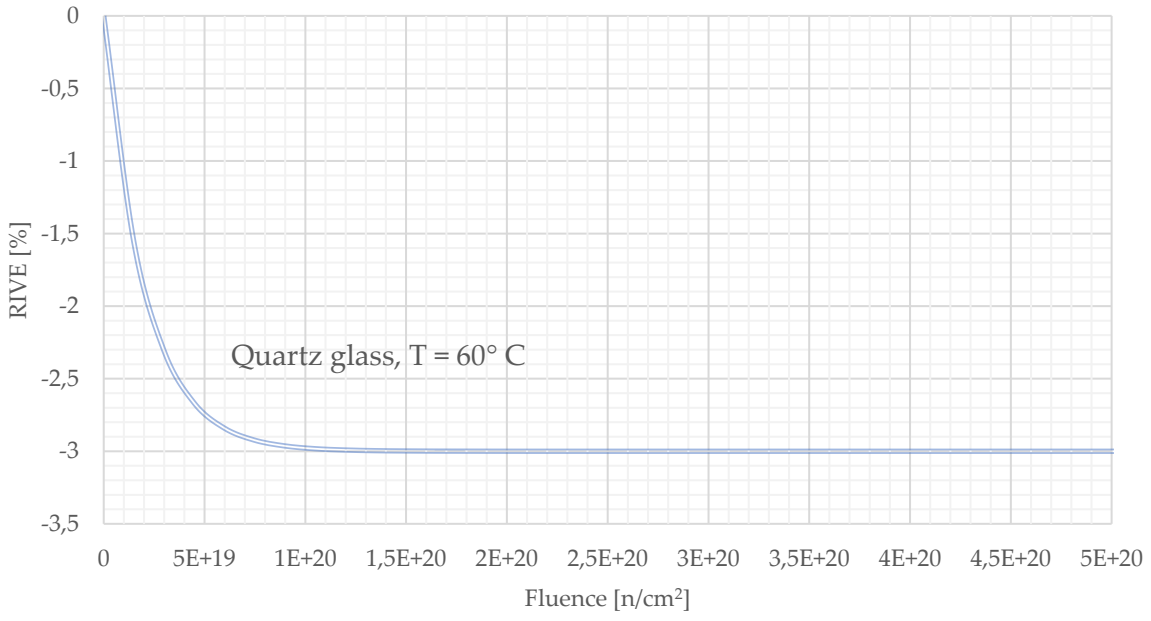

Figure 2.5.3. Volumetric contraction of amorphous quartz glass (Denisov et al., 2012)

2.6 Meso-scale numerical simulation of irradiated concrete

In an attempt to reflect realistic behavior of concrete under irradiation exposure, numerical models based on *finite element method* (FEM) and *discrete element method* (DEM) were introduced into various research methodologies. While the FEM is a numerical method for continuum materials, the DEM is a particle-based approach. A noteworthy type of the DEM is a Rigid Body Spring Model (RBSM) proposed by Kawai (Kawai, 1978). In general, structures could be yielded or crushed under a peak loading and divided into pieces, which behave like rigid bodies. In the 3D RBSM, a model of concrete is represented by rigid polyhedrons interconnected by springs at each of the contact surfaces. Deformations or transfer of internal forces are done by this network of springs. In that way, the displacement of each rigid-body polyhedron could be described by the movement of the respective centroids, consisted of 6 degrees of freedom (therefore, the size of the element stiffness matrix never exceeds 6 × 6). A random geometry of these polyhedrons formed by Voronoi diagram created to possibly reduce mesh bias on the initiation of potential cracks, since the crack propagation is affected by mesh design (Fu et al., 2017).

In the study presented by Sasano *et al.* (Sasano, et al., 2020), an RBSM model is used for numerical simulation of concrete affected by radiation-induced aggregate expansion. The main goal was to assess the mechanical properties (compressive and splitting tensile strength, Young's modulus) of concrete subjected to neutron irradiation and to clarify 1) contributions of the degradation of compressive strength and Young's modulus on mortar expansion and degradation due to expansion of fine-aggregates, 2) isolated expansion of cement paste and fine-aggregates, 3) expansion and following cracks in aggregates, 4) creep of mortar. The model takes into account three phases in concrete, namely aggregates, cement paste and the ITZ. The fracture behavior of the model reflected by nonlinear constitutive laws given to the springs between elements (phases) (Figure 2.6.1). Discontinuous behavior of concrete was modeled explicitly so that it was possible to reproduce the post-peak load deformation and fracture behavior for a stress-strain interaction.

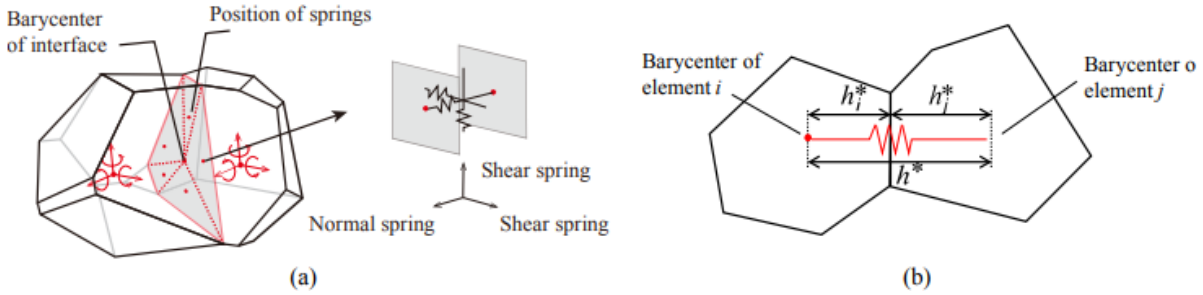

Figure 2.6.1. Illustration of a) Voronoi elements b) connecting springs (Sasano, et al., 2020)

The experimental results obtained by Maruyama *et al.* (Maruyama et al., 2017) were used as the reference data (physical properties and RIVE of aggregates and concrete) for numerical simulations, where the impact of gamma-rays and temperature were separated and temperature increase due to thermal vibrations from secondary gamma-rays is kept below 75° C, so that it was close to the normal operational temperature of NPPs.

The constitutive laws used in the model (Sasano, et al., 2020) were implemented for the springs between the elements to set up instantaneous behaviour based on studies by Yamamoto *et al.* (Yamamoto et al., 2014). Figure 2.6.2 shows the laws, where a) tensile model of a normal spring b) shear spring model c) coefficient of softening for the shear spring d) Mohr-Coulomb criteria for the shear spring and e) shear reduction coefficient.

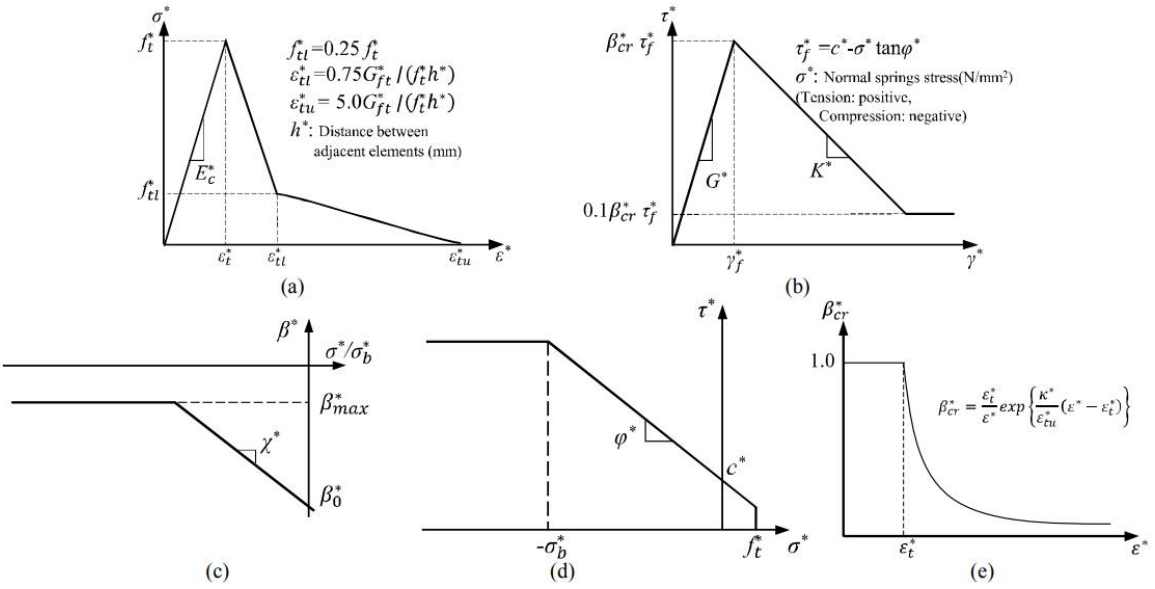

Figure 2.6.2. Spring models, coefficient of softening, Mohr-Coulomb criteria and shear reduction coefficient (Sasano, et al., 2020)

It is worthy to mention the behaviour of a close vicinity between two phases (concrete and cement paste). The contact area is called the third phase or the Interfacial Transition Zone (ITZ), which is the weakest link in concrete structure. It forms near the coarse aggregate

particles, and the cement paste particles cannot pack together closely, as a result the molecular bond of cement paste is weaker at the ITZ. Shearing stresses are exerted on the cement paste by aggregate particles causing water to separate from the cement paste. As a result, water-to-cement ratio is increased at the contact area leading to narrow links of decreased strength bonding. The role of ITZ is very important in realistic numerical modelling of irradiated concrete (Rosseel, et al., 2016) and its effect is considered according to Maruyama *et al.* (Maruyama & Sugie, 2014).

The elastic modulus and strength for the ITZ is lower than for the bulk mortar, and was considered for both normal and shear springs. The constitutive laws for the ITZ are illustrated in Figure 2.6.3 for a) tension and compression b) shear.

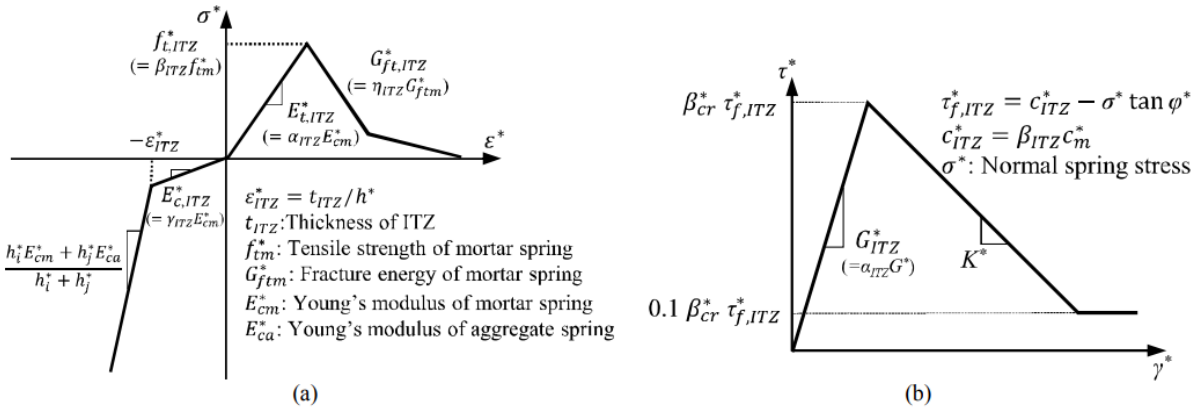

Figure 2.6.3. Constitutive laws for the interfacial transition zone (Sasano, et al., 2020)

Moreover, changes of the moisture content in cement paste is also taken into account via drying-out process, as the moisture content affects the mechanical properties; heat and moisture transfer was introduced by the truss network system, where one-dimensional heat/moisture diffusion problem was solved for every individual truss element.

Figure 2.6.4 illustrates appearance, aggregates, cross-section for coarse and fine mesh of the model.

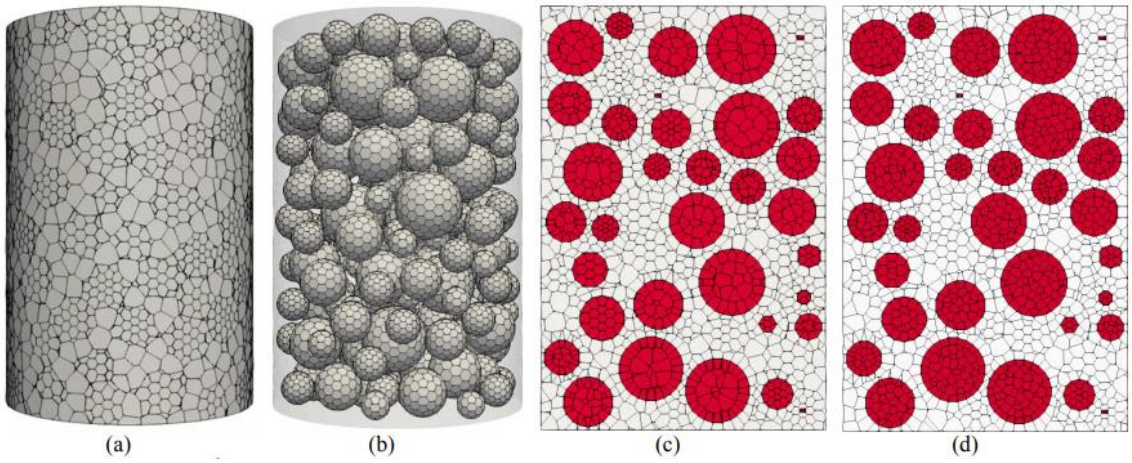

Figure 2.6.4. a) appearance b) aggregates c) cross-section for coarse mesh d) cross-section for fine mesh (Sasano, et al., 2020)

Based on the simulation output, Sasano *et al.* have concluded that:

- the ratio of concrete to coarse aggregates expansion ranged from 0,71 to 0,76 (depending on mortar expansion), which was observed same for the experimental results (Figure 2.6.5).

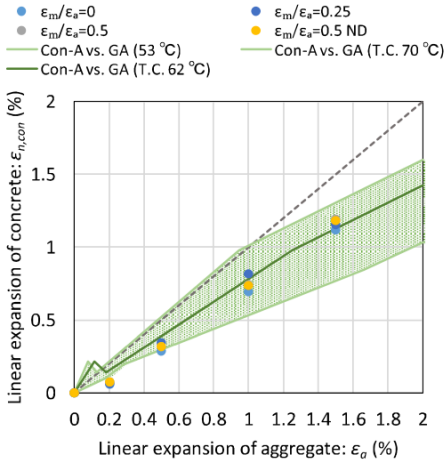

Figure 2.6.5. Ratio of $\varepsilon_{conc}/\varepsilon_a$, green area is the range in the experimental results (Maruyama et al., 2017) and marks are the simulation results (Sasano, et al., 2020)

- the simulation showed similarities of compressive strength and Young's modulus with the experimental data of concrete samples under neutron irradiation (Figure 2.6.6). When the ratio of mortar to aggregate expansion was 0,5, the simulation exhibited the best agreement with the experimental data, where quartz was accounted for half of the volume of mortar and showed larger swelling than pure quartz (Pedersen, 1971). Also, good correlations were obtained with creep consideration for the ratio 0,25. It means that the swelling of fine-particle aggregates in mortar must be considered under neutron irradiation or creep of the same magnitude is expected. Finally, if the neutron-

induced expansion of fine-grain aggregates is minor, and the neutron-induced expansion of coarse aggregates is large, then the damage in concrete is at the maximum, therefore the reduction of strength and Young's modulus is significantly high.

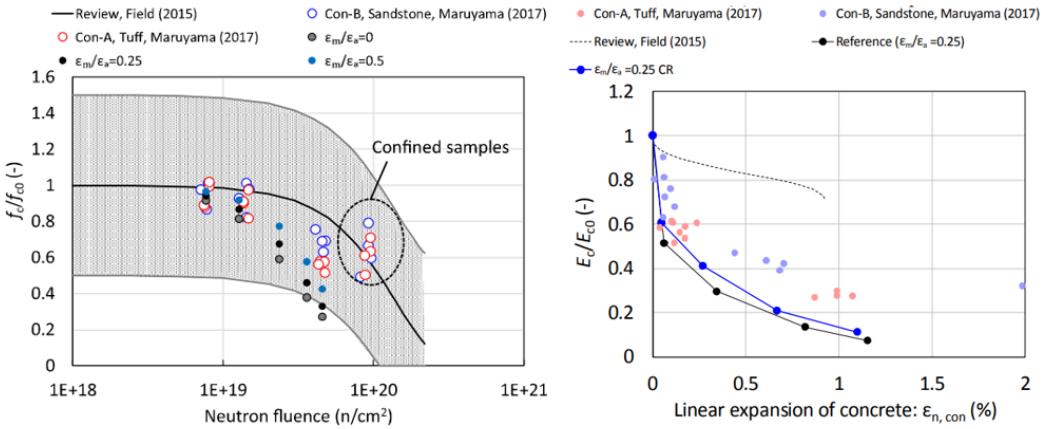

Figure 2.6.6. The ratio of f_c/f_{co} with the neutron fluence, grey area is the st. dev. of Field's curve (Field et al., 2015) (Sasano, et al., 2020); Young's modulus ratio with the linear expansion of concrete (Sasano, et al., 2020)

- the neutron-induced expansion of fine-grain aggregates does not significantly affect physical properties of irradiated concrete, it means that the main factor for concrete degradation is the neutron-induced expansion of coarse aggregates. Figure 2.6.7 illustrates damage simulation after aggregate/mortar expansion.

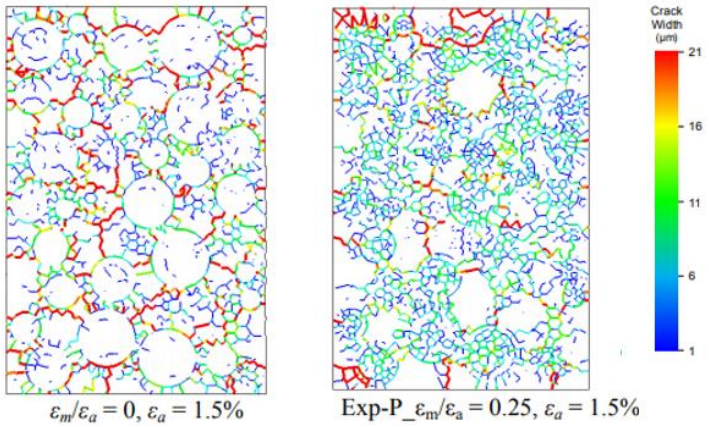

Figure 2.6.7. Damage simulation after aggregate/mortar expansion (Sasano, et al., 2020)

- the type of rocks is critical for an overall expansion of concrete. It was proved by the isolated expansion of mortar (Figure 2.6.8), where fine-grains of sandstone (which exhibit significant expansion) were introduced into the mortar, and coarse aggregates of calcite were applied into the concrete.

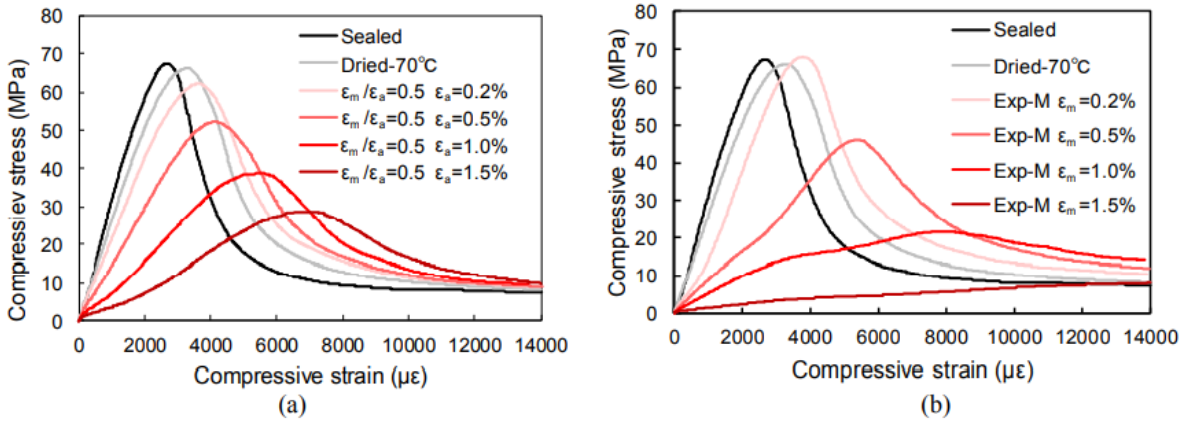

Figure 2.6.8. Simulated stress-strain relationships of a) $\varepsilon_m/\varepsilon_a = 0{,}5$ b) isolated mortar expansion (Sasano, et al., 2020)

- the reduction by 5 – 10 % was observed in Young's modulus of concrete with inhomogeneous expansion of coarse aggregates compared to concrete with homogeneous expansion at the early stages. Therefore, cracks in coarse aggregates with inhomogeneous expansion cause the reduction of Young's modulus, however slight differences appeared in the relationship of concrete strength ratio and linear expansion of concrete (Figure 2.6.9).

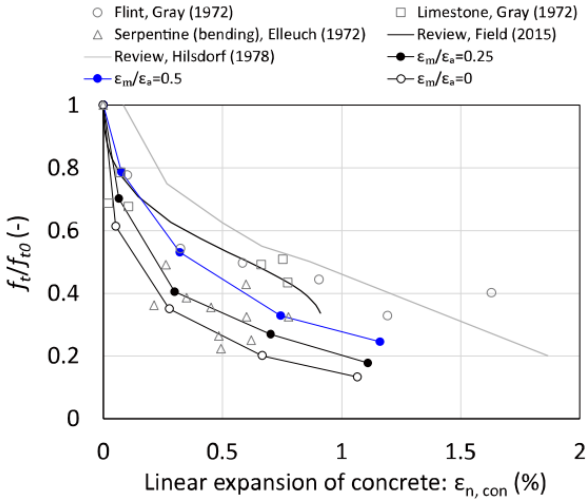

Figure 2.6.9. Simulated splitting tensile strength ratio with the linear expansion of concrete (Sasano, et al., 2020)

CHAPTER 3

Methodology

3.1 Baseline characterization of non-irradiated specimens

In the framework of the project, Research Centre Řež (CVŘ) received 6 series (6 rock types) of aggregates with the total of 30 samples of aggregates from the Oak Ridge National Laboratory, USA, and 2 series of irradiated aggregates with the total of 16 samples from the Institute for Energy (IFE), Norway. For the following pre- and post-irradiation examination of samples, it was decided to proceed with the 2 coincident series marked as E and F, since the post-irradiation examination in CVŘ is not finished yet. Namely, the non-irradiated E27, E32, E37, E38, E39, F27, F32, F37, F38, F39 (10 in total) and the irradiated E01, E02, E07, E08, E13, E14, E19, E20, F01, F02, F07, F08, F13, F14, F19, F20 (16 in total, mostly crushed by mechanical testing at the IFE before shipping), where a letter refers to a rock type. Each whole sample has a cylindrical shape with dimensions Ø 10 mm and 10 mm height. The small sizes were chosen due to specifications of research reactor.

In order to characterize the neutron-induced structural changes, the following techniques are used at the CVŘ:

- Dimension measurements – the procedure to observe geometry changes of the samples. The measurements will be performed at 5 different points for diameter and another 5 for height.
- Density measurements – the procedure to record changes in density. It is based on water and helium pycnometry.
- Light optical microscopy – the procedure to determine a mineralogical content, textural relationships, grain size, present cracks and defects within a rock, and to compare with the other samples.
- Scanning electron microscopy with energy-dispersive spectrometry – the procedure to complement data of phase composition from LOM, where content can be roughly estimated. EDX will be used for microanalytical studies.
- Raman microscopy – the procedure to analyze samples by recording spectra at

different points or on a line of the sample map. The recorded spectra of the individual lines for each sample were used to follow the most significant features/minerals within the thin section.

- Fourier-transform infrared spectroscopy – the procedure to determine mineral content from prepared powder.
- X-ray diffraction – the procedure to determine mineral phases, content of crystalline and amorphous phases by Rietveld analysis from XRD patterns.

3.2 Irradiation in research reactor

The characterized samples will be sent to the LVR-15 for irradiation experiments. Due to the fact, that radiation doses to cause a significant impact are pretty high, and, generally, equal to the amount of dose received by the internal surface of CBS after 40 years of normal operation of LWR, the irradiation experiments should be performed under accelerated conditions. Different target doses, such as 1×10^{19}, $2{,}5 \times 10^{19}$, 5×10^{19}, $7{,}5 \times 10^{19}$ and $12{,}5 \times 10^{19}$ n/cm^2, were chosen to assess the changes in function of fluence. Specialized aluminum rigs will be used as holders for irradiation procedure. Resultant expected temperature (heating produced by secondary gamma rays) of samples is below 60° C.

3.3 Baseline characterization of irradiated specimens

The characterization of irradiated samples will be based on exactly same procedure with exactly same conditions as for non-irradiated samples, except that irradiated samples after geometry and density measurements will be cut into thin section (~1,5 – 2 mm thick) for microstructural analysis (LOM, SEM + EDX, Raman) and other part will be grinded into powder for phase characterization (XRD, FTIR).

In this thesis, characterization of irradiated samples will be based on samples transported from the IFE. The changes will be recorded and used for discussion of E and F series.

Procedure

4.1 Pre- and post-irradiation examination

4.1.1 Dimension measurements

- **Dimension measurements of non-irradiated samples:**

The pre-drying process and weighing were realized prior the measurement procedure. Each sample was pre-dried in a tempered electric furnace for 24 hours with silica gel for moisture absorption. The parameters for pre-drying were 30° C temperature and 20 – 30 mmHg pressure. Dimension measurements were performed using ***Vertex 251HM by MicroVu*** with a touch probe 6W 20 1x4 (Figure 4.1.1.2). Each sample was fixed properly into the specified holder to mitigate any displacements and rotations. As it was proved experimentally, the device is sensitive to vibrations. At first, the sample was placed to the holder for diameter measurements. This holder is fixed to a lead base with 3 screws where samples were affixed to. The holder for height measurements is made from a steel block and had been cut to the shape of cradle with a half circle profile where each sample was fixed. When the sample was fixed in the holder, the program for diameter/height measurements was launched by the operator who manually marked borders of the sample with optical instruments and switched for the automatic probe measurement. The results from measurements were 5 diameters (D1 – D5) and 5 heights (H1 – H5) (Figure 4.1.1.1) measured in designated points. The reports with the exported values were saved in .pdf and .xlsx format. The operator also took at least one picture of each sample during the measurements.

Figure 4.1.1.1. Diameters marked as D-1:5; Heights marked as H-1:5

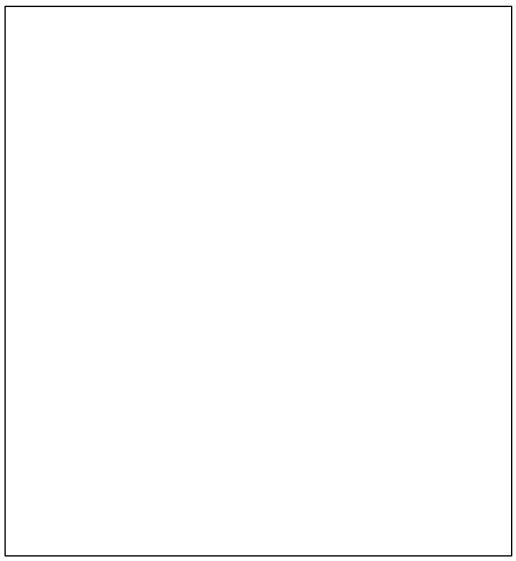

Figure 4.1.1.2. Vertex 251HM by MicroVu with the samples

- **Dimension measurements of irradiated samples:**

After receiving the active samples, they were unpacked and sorted. In case of irradiated aggregates, all works were done inside a hot cell (Figure 4.1.1.3). After unpacking, it was found out that some active samples were broken up into several pieces (Figure 4.1.1.4). Due to such condition of the samples, it was not possible to measure their dimensions.

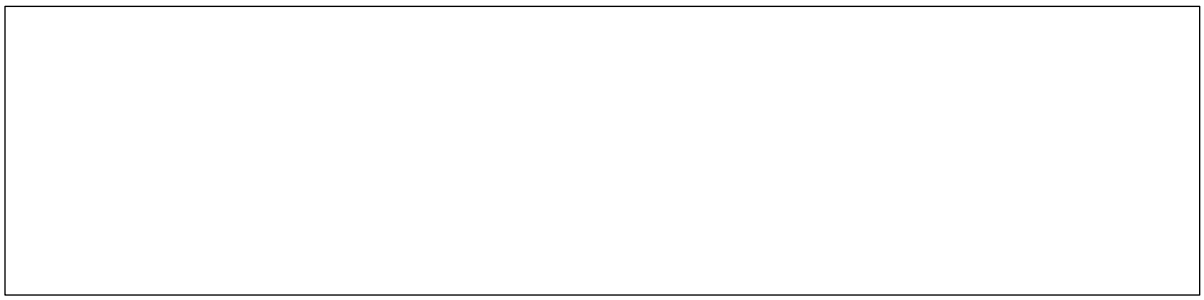

Figure 4.1.1.3. a) b) unpacking c) sorting

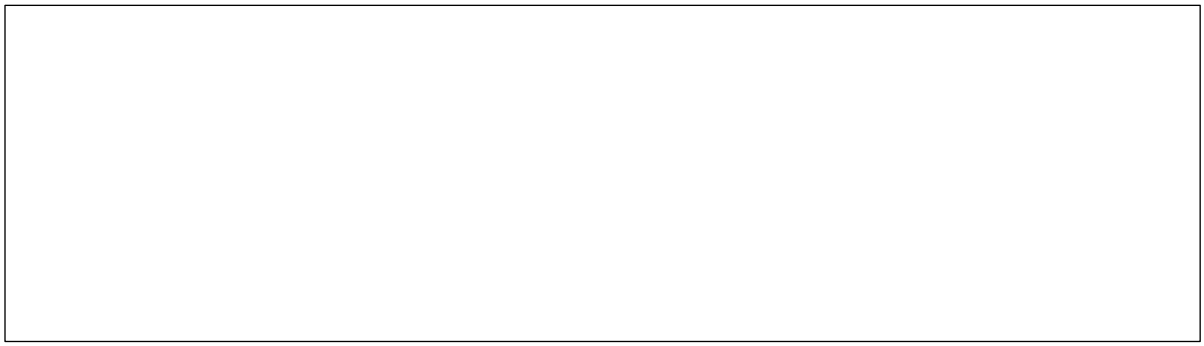

Figure 4.1.1.4. a) b) broken parts of the samples

4.1.2 Helium and water pycnometry

Densities of samples were measured by two different methods – helium pycnometry and water pycnometry. All of the received samples (non-irradiated/irradiated) were prepared for measurements in the same way. Before each measurement, the samples have been dried in the same electrical furnace with the silica gel (Figure 4.1.2.1 (b)). The drying conditions were as follows: temperature 30° C, pressure 30 mm/Hg for 24 hours. After the drying procedure, samples were placed in the desiccator for equalization of temperature differences (Figure 4.1.2.1 (a)).

- **Density measurements with a helium pycnometer:**

Density measurements with a helium pycnometer were performed using the *Pycnomatic – ATC Evo by Porotec* (Figure 4.1.2.1 (d)). The declared accuracy of measurement is ± 0,01 % and depends on cleanliness of samples, purity of gas and a temperature. The factors are taken into account, samples were carefully placed in and out of pycnometer using forceps or medical gloves at the constant temperature 20° C. Obtained precision, standard deviation, in the laboratory typically have varied between 0,0005 – 0,024 % for both density and volume. The measurements of well dried samples were done at 20° C. Sample weight was measured using *Radwag AS220.R2* (Figure 4.1.2.1 (c)). Samples were weighted one time right after the removal from drying/heating chamber and before measurements on pycnometer. It is done with the accuracy ± 0,00001 g. Calibration of the device was done twice a day, before and after measurements to exclude possible errors.

After placing the samples in the pycnometer, 10 cleaning cycles for degassing the sample's chamber were performed. During the cleaning process the chamber is cleaned from atmospheric gases and filled with pure helium. The accuracy of measurements given by the standard deviation 0,025% set before the test. It means that the analysis is stopped when the volume results standard deviation falls below the set value. Based on set weight and measured volume, the real density is calculated. One measurement contained three good cycles. For each sample three such measurements were carried out.

The procedure for density measurements by helium pycnometry was also performed for irradiated samples in the hot cell (Figure 4.1.2.2). However, due to the size and the condition of the samples after irradiation, measurements could not be performed for all samples.

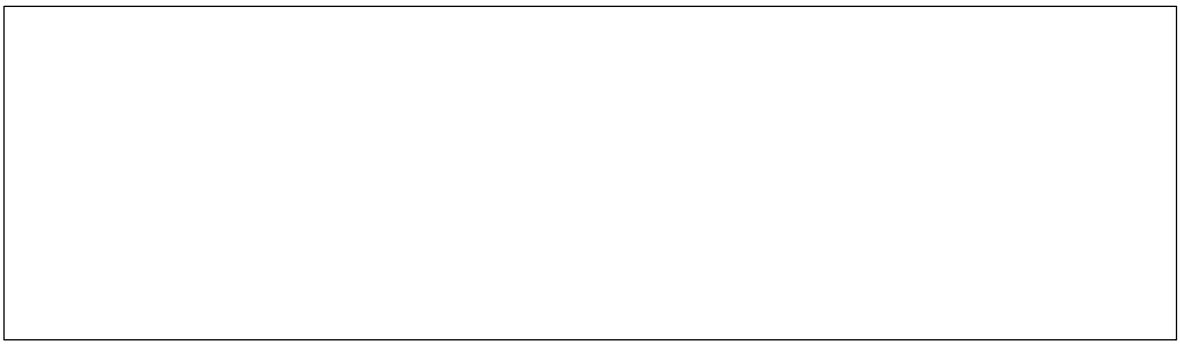

Figure 4.1.2.1. Helium pycnometry equipment; a) desiccator for dried samples storage b) furnace c) scales d) helium pycnometer

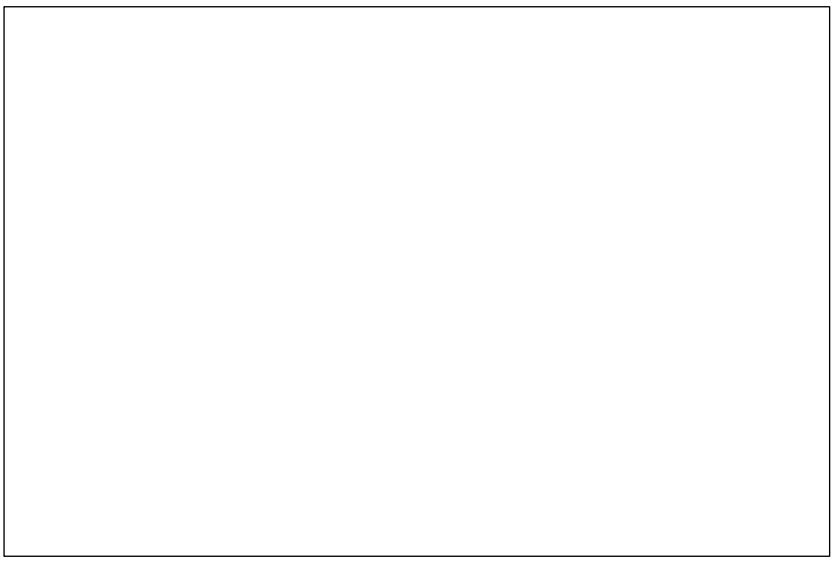

Figure 4.1.2.2. Water and helium pycnometry of irradiated samples in hot cell; a) scales b) helium pycnometer c) furnace d) operational holders e) transportation holders

- **Density measurements with a water pycnometer:**

All water pycnometry measurements were done in the hot cell to ensure the same conditions for measurements of non-irradiated and irradiated samples. For water pycnometry, *Analytical balance Kern 220g x 0,1 mg* with set *YDB-03* for density determination was used. Before measurements, samples are cooled to the room temperature 23 – 24°C. As a reference liquid, distilled water at the same room temperature was used.

Three measurements for each sample were performed. The samples were dried after each measurement. Firstly, the sample was placed carefully on a scale for determination of weight in air, then the sample was immersed into the water at the minimum depth to fully cover the specimen and weight was measured. An effort was made to minimize the formation of bubbles attached to the surface of the samples during immersion in water, which may distort the results due to buoyancy forces. The procedure of immersion is done quickly to avoid

absorption of water by aggregate. Such facts provide us with the information that acting hydrostatic pressure is small and that apparently the density of sample is calculated with pores filled with air. It can be observed from the laboratory data that measured density in water pycnometer is always smaller than the one measured in helium pycnometer for the same specimens. After one measurement, sample was placed into the heating chamber for at least a day to release free water. Each sample was measured three times. The density was calculated based on measured weights and known density of distilled water.

Before and after day cycle measurements, the density of calibration body made of stainless steel was measured to monitor changes in measurement conditions and their possible effect on results. Since measurements are based on Archimedes' Law, it can be observed that accuracy of the device is sensitive to density of water and accuracy of weighing scales. Such factors as temperature of water, atmospheric pressure and relative humidity of the environment influence density of water. While temperature of water is the main influencing parameter, relatively small underpressure of 480-490 Pa created in the hot cell and relative humidity of 22 – 29 % are errors in order of hundredth of percent. Such fact was also experimentally proved during measurement of the reference sample inside and outside of the hot cell.

For the active samples, the same procedure of measurements was used. Since the active samples were disintegrated into several pieces, density measurements were done for each specimen separately.

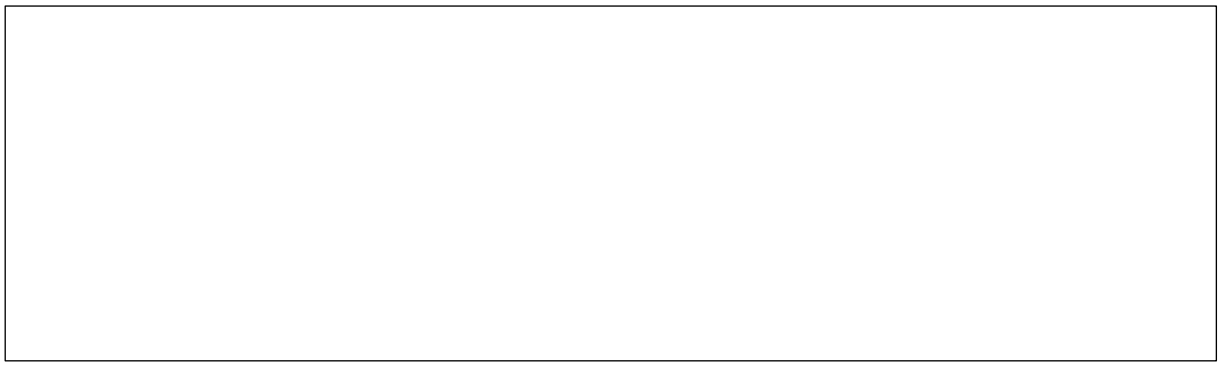

Figure 4.1.2.3. a) water pycnometry equipment in the hot cell b) analytical scales with the immerged sample

4.1.3 Light optical microscopy

- **Thin section preparation:**

In order to describe the mineralogy and petrography of the studied aggregate samples,

petrographic thin section from each sample was prepared for use with a polarizing light optical microscope (LOM), electron microscope and Raman microscopy. A slice ~1,5 – 2 mm thick was cut from the aggregate sample, using a diamond low-speed saw *Buehler Isomet*. One side of the sample was affixed to the glass slide using UV cement *EpoSpeed S (Struers)* and after the curing ground optically flat using 2500 and 5000 grinding wheels and washed carefully. The flat surface is then mounted on a glass slide using insoluble cement *EpoSpeed 20 (Struers)* and the fixed upper part is gently released from the soluble UV cement. *Abele system (Struers)* is then used to grind smooth using progressively finer abrasive grit until the sample is ~50 μm thick. The final grinding and polishing are done on *LaboPol 25 machine (Struers)*, using 2000 grit, and series of diamond suspensions (9,3 and 1 μm) to finalize the surface on the final thickness of ~25 – 30 μm. The final steps are controlled observing the prepared thin section under polarizing microscope. The method involved uses the Michel-Lévy interference color chart. Typically, quartz is used as the gauge to determine thickness, as it is one of the most abundant minerals, showing an interference color of first-order grey to white. Figure 4.1.3.1 illustrates the non-irradiated thin section sample preparation.

Figure 4.1.3.1. Preparation of thin sections from non-active aggregates, where a) sample; b) low-speed diamond saw; c) two cuts are performed to have material for thin section preparation, one backup slice and the rest prepared for further powdering for XRD analysis; d) slice affixed to the glass slide; e) grinding and polishing; f) thickness control with light optical microscope with cross-polarized light

For the preparation of thin section from irradiated aggregate samples, the procedure of

cutting, mounting, grinding and polishing was moved to CVŘ hot cells. Cutting of cylindrical samples was done using a diamond low-speed saw (*Buehler Isomet*) in the hot cell HK1, the specimens were attached using the manipulators. Due to the small sample size, handling of these specimens was extremely difficult and time-consuming. After the specimens cutting, the individual pieces dedicated for thin section sample preparation were shifted to shielded glove box, where grinding and polishing steps were performed (Figure 4.1.3.2). For the grinding and rinsing of irradiated samples, ethanol was used exclusively.

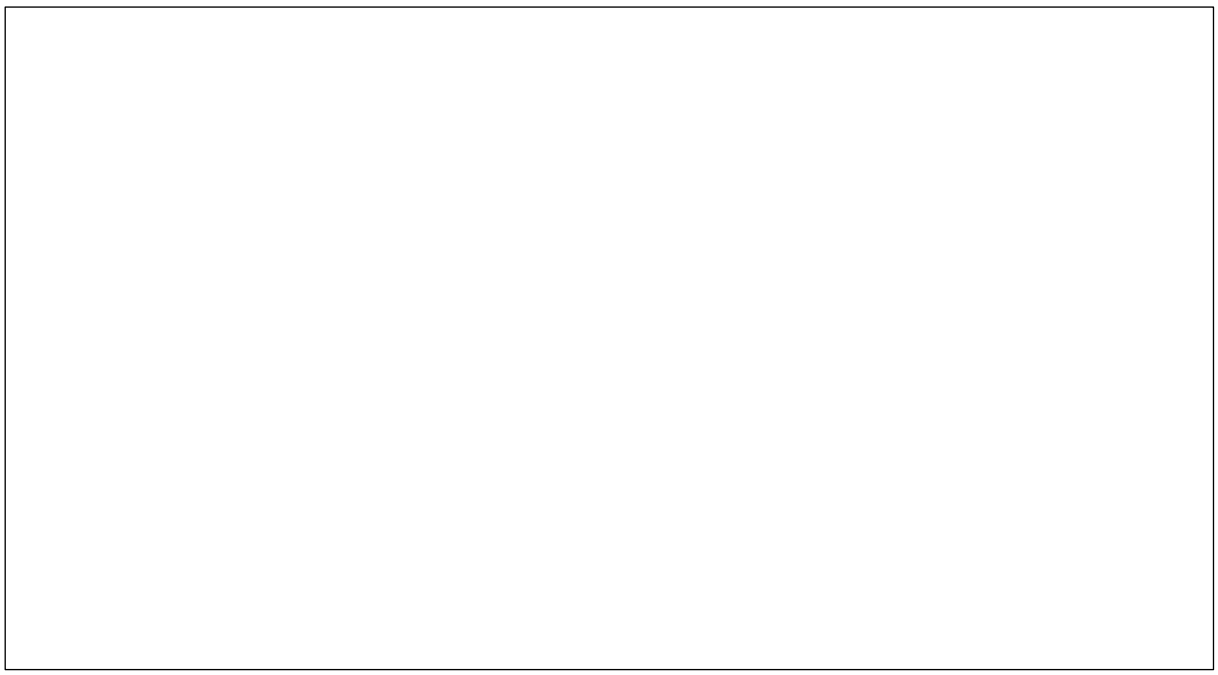

Figure 4.1.3.2. Preparation of thin sections from irradiated aggregates, where a) samples are affixed and cut using low-speed diamond saw; b) two cuts are performed to have material for thin section preparation, one backup slice and the rest prepared for further powdering for XRD analysis; c) d) slice for thin section preparation is moved to the glove-box laboratory, where the fixing to the glass slide is done in active hood; e) f) sample is then moved to shielded glove-box for grinding and polishing using Abele system (Struers)

- **LOM observation:**

Light optical microscopy of the prepared thin sections of aggregates was used for identification of minerals in individual samples, as well as for description of the morphological characteristics of individual minerals, fractures, decomposition or alteration. Special attention was paid to evaluation of textural changes prior/after irradiation. For the microstructural observation, optical microscope *Leica DM 2700M*, fitted with 5 Mpix CCD camera, was used. The microscope is equipped with two Nicol prisms having their polarizing planes oriented perpendicular to one another. Using one polarizer enables to view the slide in plane polarized light; using two polarizes allows for analysis under cross polarized light. The polarized light

microscopy was used to 1) identify the present minerals, 2) describe the main textural features, 3) evaluate the particle sizes, 4) observe the present cracks/defects within the minerals and matrix, 5) compare the similarities and differences among the samples of one aggregate type. The microscopical observation (both optical and electron microscopy) can be used also as auxiliary method for phase identification and quantification in individual aggregate types, supporting the Rietveld analysis of XRD diffraction patterns.

4.1.4 Scanning electron microscopy with energy-dispersive spectrometry

- **Characterization of pre- and post-irradiated aggregate samples by SEM-EDX:**

Scanning electron microscopy (SEM) combined with energy-dispersive spectrometry (EDX) was used to characterize the prepared thin-sections, which were firstly observed by the LOM. The thin sections, dedicated for analysis, were coated by 25 nm thin layer of carbon (*Quorum Technologies Q150T high vacuum carbon coater*) to ensure the conductivity of the surface. To complement the information obtained from the cross-polarized images, where the amount of individual minerals can be roughly estimated, EDX large-area mapping of representative part of the thin section was performed. For the analysis of non-irradiated samples, scanning electron microscope *FIB-SEM Lyra GMU (Tescan)* at the Diagnostic Centre of CVŘ was used. The microscope is equipped with the back-scatter detector (BSE) for visualization of the Z-contrast enables to distinguish between individual mineral phases present in the samples, and *EDX X-Max^N 80 detector (Oxford Instruments)* for microanalytical studies.

Firstly, a set of BSE images and point analyses to identify the phases present in the thin section was performed. For characterization of the chemical composition of aggregates, large-area X-ray elemental maps of the ~25 mm^2 domains were acquired using *Aztec 3,3 software (Oxford Instruments)*, the analytical conditions were 3,5 hours live time, 15 kV accelerating voltage, 20 keV energy range with 10 eV/channel energy resolution. Each large-area map was compiled from 25 individual mapped fields with dimensions of 512 x 512 μm, the spatial resolution of each map is ~1 μm. Phase maps (modal analyses) were calculated using the parameters of boundary tolerance 10,0 and grouping level 0,1. From these phase maps it is possible to calculate the fraction (%) of individual minerals present within the analyzed samples.

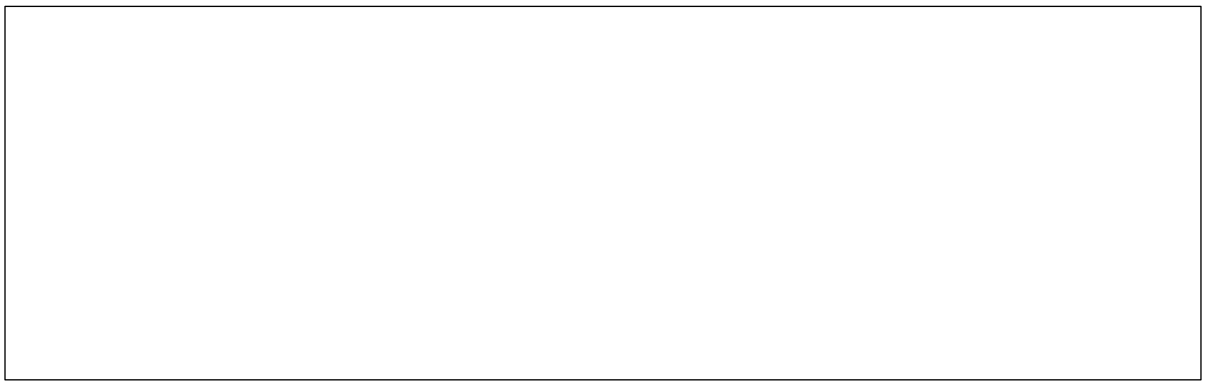

Figure 4.1.4.1. a) preparation of thin sections in the shielded glove box; b) c) SEM-EDX analysis in Semi-Hot cell

4.1.5 Raman microscopy

Micro-Raman spectra of samples were measured by dispersive Raman spectrometer (*Nicolet model DXR2-Raman microscopy*) equipped with the confocal microscope *Olympus*. As an excitation source, a laser, with wave length 532 nm and input power 10 mW, was used. Samples were measured with the following parameters: laser power 2,5 – 10 mW, measurement time is 15 s and a number of accumulations of spectrum is 15. The parameters were adjusted as such to exclude thermal destruction of samples. High-resolution Grating-1800 gr/mm (spectral range 1800 – 50 cm^{-1}), 25 or 50 μm confocal pinhole apertures and CCD detector (a multi-channel cooled CCD camera) were used (Figure 4.1.5.1). The *OMNIC* and *Origin* software were used to analyze the recorded spectra.

Using microscopy, samples were focused to select a micro location of interest and to create a map of the micro area. The samples were then analyzed by recording spectra at different points (point analysis) or on a line (line analysis) of the sample map. The recorded spectra of the individual lines for each sample were used to follow the most significant features/minerals within the thin section. The line contained 8 to 25 spectra. On the other hand, the individual grains of some samples were analyzed by point analysis, with the aim to distinguish the main minerals, such as quartz, albite, microcline based on their spectra.

Since resolution of the optical microscope is lower than that used for SEM-EDX and LOM characterization, we indicated the location of the line/points after measurement and obtained the LOM images of the analyzed regions for comparison.

Figure 4.1.5.1. Raman microscopy a) full equipment; b) detail of the sampling site

4.1.6 Fourier-transform infrared spectroscopy

The spectra of prepared powder samples were measured on ***FT-IR spectrometer Nicolet iS50*** equipped with Attenuated Total Reflection (ATR) module containing Diamond crystal (see Figure 4.1.6.1). The spectra were collected in the range of 400 – 4000 cm^{-1} after 120 scans at 4 cm^{-1} resolution. The background (air) was measured before each sample measurement.

Both non-irradiated and irradiated samples were measured following the same experimental setup.

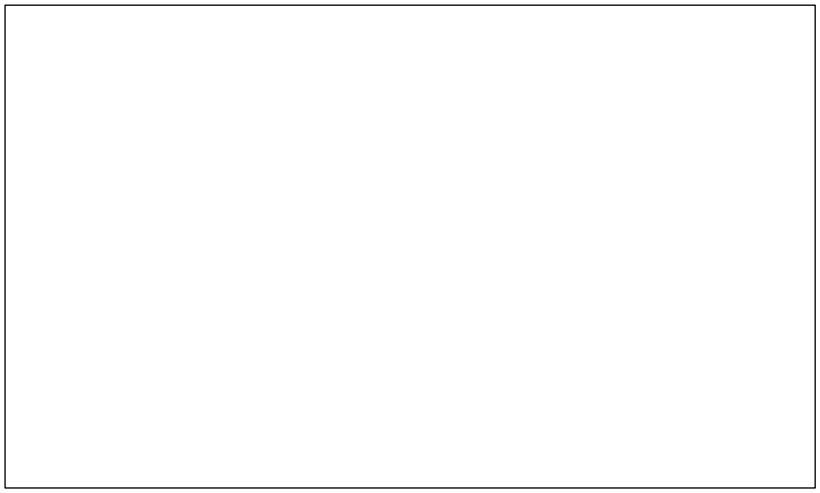

Figure 4.1.6.1. FTIR spectrometer

4.1.7 X-ray diffraction

- **Characterization of pre- and post-irradiated aggregate samples by SEM-EDX:**

The received samples, in bulk, consisted of cylinders with average dimensions 6 mm height and 10 mm in diameter.

The powders were prepared using an *oscillating ball mill, model MM400 (Retsch, Germany)*, equipped with zirconium oxide balls (10 – 20 mm diameter) and two stainless steel milling jars

(35 ml) with zirconium oxide inner coating (Figure 4.1.7.1). Three steps were followed for the grinding of the bulk samples, firstly, a "dry" grinding to break down the bulk sample into a coarse powder, the second and third steps were "wet" milling using different oscillation frequencies to reduce and homogenize the size distribution of the particles in the powder and finally produce a fine powder. The use of ethanol (2 ml) as a wet medium reduces the friction between the particles, therefore more homogeneous and rounded particles with narrower size distribution are produced. Using this method an average particle size of 4 microns was achieved.

After the milling process, the result is a slurry from the mixing of powder and ethanol. The slurry is then poured on a petri dish and dried by air from a hair-dryer. After drying, the powder is collected and labelled according to the name of the aggregate sample.

The preparation of irradiated samples has three main differences. Firstly, the procedure is carried out inside of a shielded glove box. Secondly, all the three milling steps are carried using a "wet" route; and, thirdly, the slurries are air-dried at a room temperature until the solvent (ethanol) evaporates.

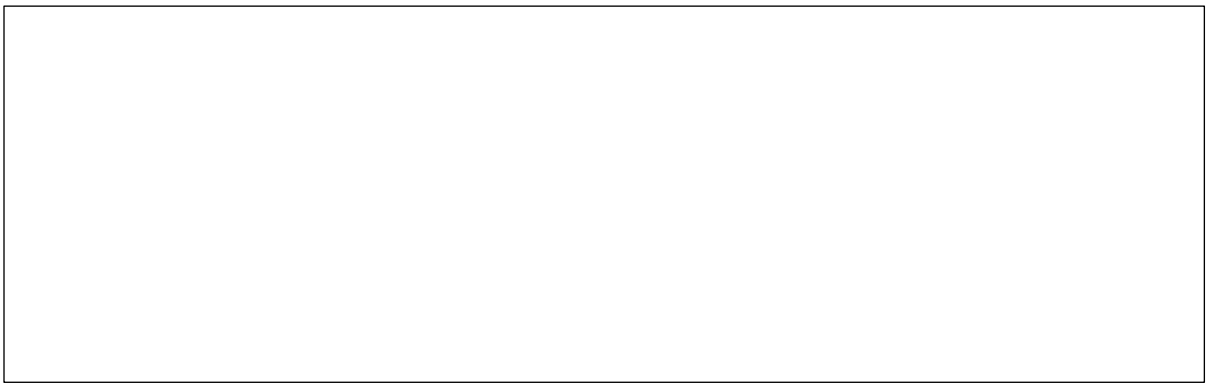

Figure 4.1.7.1. XRD equipment; a) oscillating ball mill; b) accessories used for preparation of powder samples

- **Sample preparation for XRD measurements:**

Two sets of samples were prepared: 1) the powder samples prepared as described in the previous section, and 2) the powder samples prepared as described in the previous section mixed with an internal standard.

The fine powders, with and without internal standard, were placed independently on top of a polyether ether ketone (PEEK, 6 μm, *BIEGLO GmbH*) foil attached to a metallic transmission sample holder and covered with the second PEEK foil (Figure 4.1.7.3 (a)). The reason for choosing PEEK over mylar foil is that it almost does not show diffraction peaks in the region

of interest during the XRD measurements as it can be seen in Figure 4.1.7.2.

Zinc oxide (*Sigma-Aldrich, cat. No. 205532*, Reagent grade 99,9%) heated at 700 ˚C for 5 hours was used as an internal standard for estimating the amorphous content. ZnO was mixed with the powder sample in the ratio 1:1 and homogenized in ethanol suspension using an agate mortar.

The procedure used for preparation of irradiated samples is quite similar to the one used for non-irradiated samples, with the difference that all the procedure is carried inside a glove box (Figure 4.1.7.4 (a)) and disposable plastic holders are used instead of metallic holders. Details of the disposable holder are shown in Figure 4.1.7.3 (b). The procedure is divided in two stages, in the first stage the bulk sample is "wet" milled in ethanol using the same settings (frequency and time) used for non-active samples, the resultant suspension is drop-casted onto the PEEK foil (Figure 4.1.7.4 (b)), then air-dried and cover by the second layer of PEEK foil, and finally sealed with a fast-drying glue before loading the inset plastic holder into the metallic holder. The sealing of the holder secures the irradiated sample inside the holder preventing any leakage. In the second stage of the procedure, the dried suspension (powder) is divided into two parts, one for FTIR analysis (Figure 4.1.7.4 (c)) and the other to be mixed with the crystalline standard in the 1:1 ratio, again under ethanol (Figure 4.1.7.4 (d)). The new suspension is used to prepare 3 samples for XRD measurements (Figure 4.1.7.4 (e)). After that, the prepared samples for XRD are transported in a shielded container to the room where the XRD measurements are performed. To avoid unnecessary irradiation of the operator of the diffractometer, only one active sample is measured at the time (Figure 4.1.7.3 (c)).

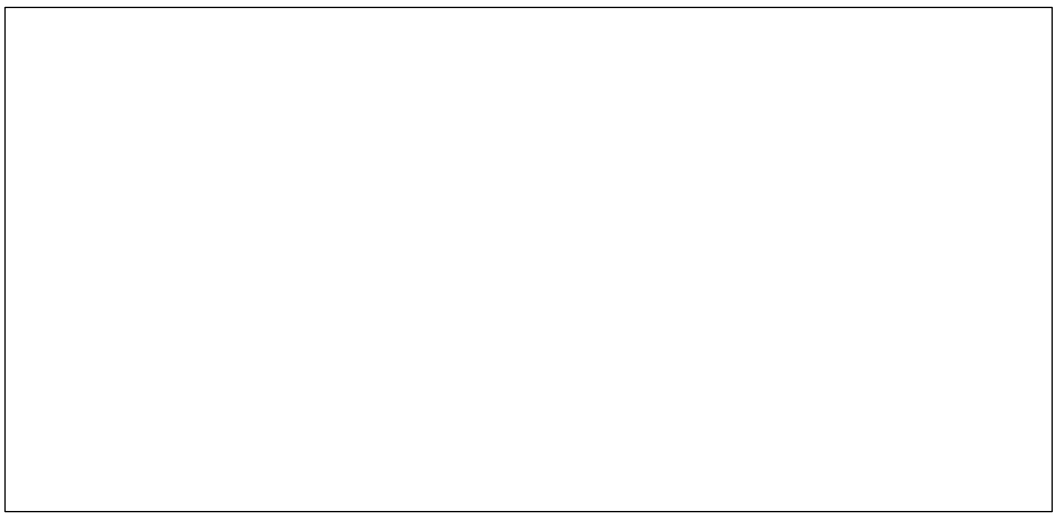

Figure 4.1.7.2. Comparison of diffraction patterns of Mylar and PEEK foils

Figure 4.1.7.3. a) holders and sample preparation of non-active samples for XRD measurements; b) disposable transmission insert holders: a – unmounted pieces, b – assembled pieces with the PEEK foil, c – assembled inset holder with powder inserted into the transmission metallic holder; c) XRD in transmission configuration with the mounted sample

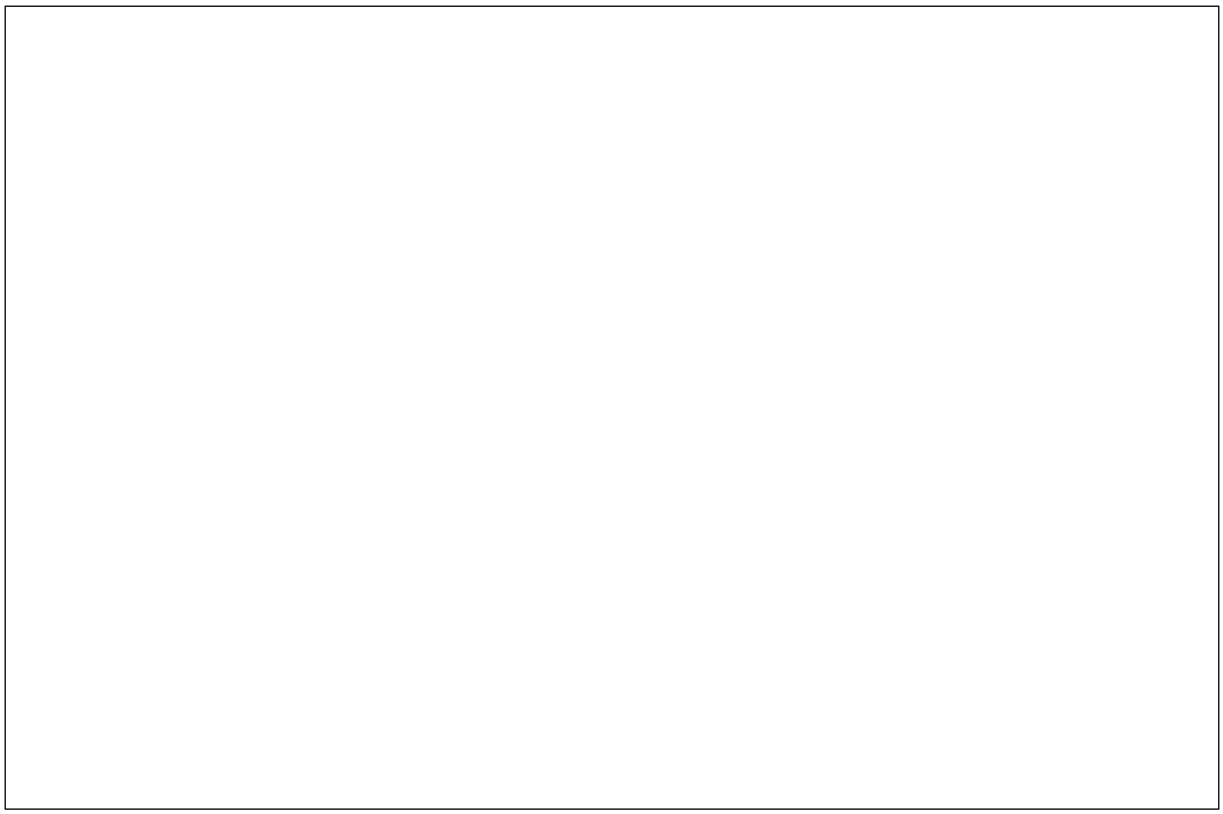

Figure 4.1.7.4. a) interior; b) preparation by drop-casting of sample for XRD analysis; c) weighting of sample for FTIR analysis; d) mixing of powder sample with crystalline standard; e) samples ready for XRD measurements

4.2 Irradiation in research reactor LVR-15

All the characterized samples will be irradiated in the light water research reactor LVR-15 (*LehkoVodní-Reaktor-15*) (Figure 4.2.1) in order to conclude swelling and structural changes caused by neutron irradiation dose. As a fuel used ^{235}Uranium (enrichment 19,75 %). The maximum heat output is 10 MW and the maximum heat flow is 1×10^{20} $ncm^{-2}s^{-1}$.

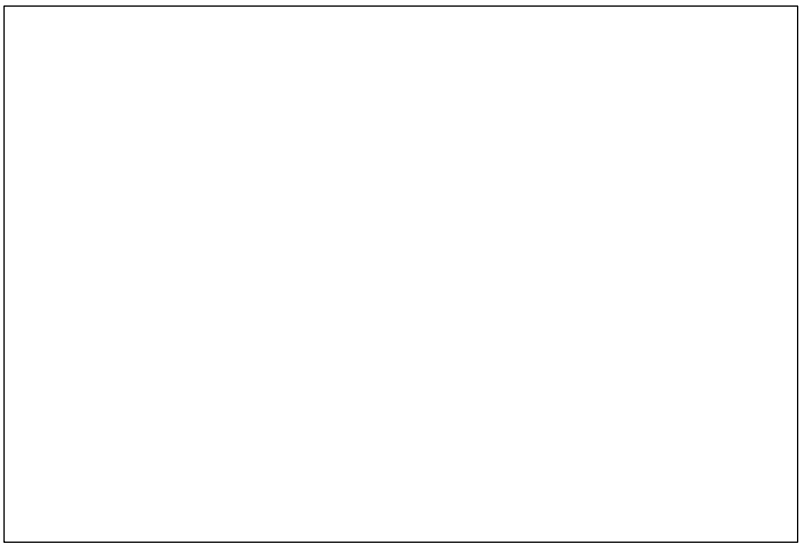

Figure 4.2.1. Interior of the LVR-15

For irradiation, samples are placed inside aluminium tubes which located inside the rig (Figure 4.2.2) also made of aluminium. Thin cavity gap filled with inert gas is provided for free swelling of aggregates. The rigs, in return, will be placed inside the reactor zone according to their position (Figure 4.2.3). Temperature control was based on detectors placed in between samples (Figure 4.2.2). Temperature of irradiation in the LVR-15 is less than 60° C (max. 59,4° C and min 45,4° C) and the neutron radiation dose vary depending on assigned target doses (Table 4.2.1).

Table 4.2.1. Target fluence and average flux for tubes

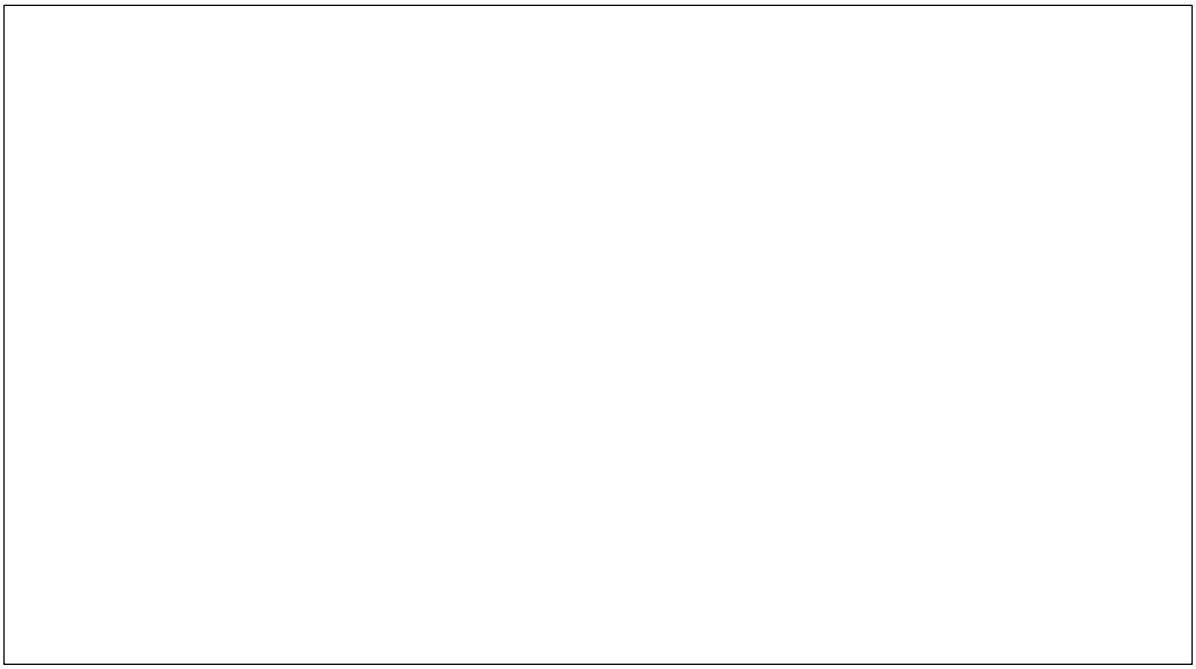

Figure 4.2.2. Design of a rig for irradiation

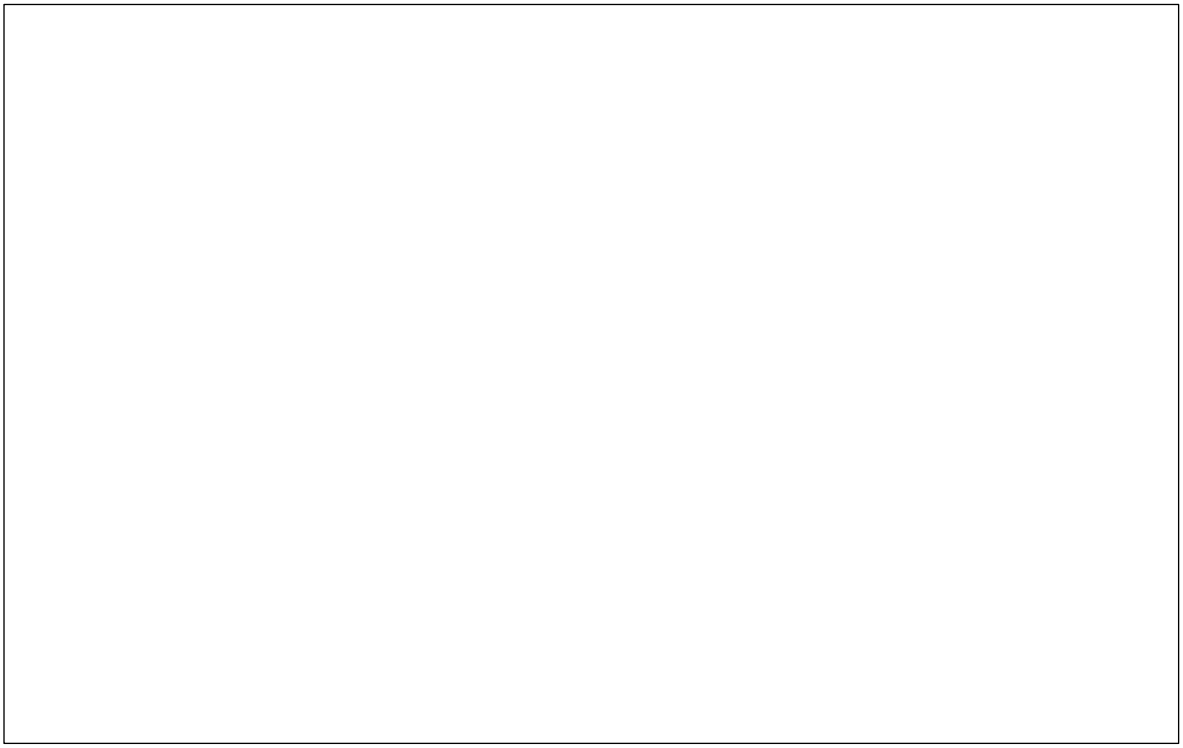

Figure 4.2.3. Positions for rigs; cross-section of the reactor

Results and discussion

5.1 Pre- and post-irradiated specimens

5.1.1 Dimensions of specimens

Average values of height and diameter were calculated for non-irradiated specimens based on the measurements (Table 5.1.1.1). By the human eye perception, the geometry of specimens is represented by perfect cylinders. However, on micro level it is not possible to see the irregularities in shape detected by measurement device. Therefore, the presented data is accompanied with the average values and standard deviations.

Table 5.1.1.1. Dimensions of the non-irradiated E and F series

Table 5.1.1.2 include dimensions of the irradiated samples. The dimension measurements are done only for selected specimens, since other samples were received in crushed condition.

Table 5.1.1.2. Dimensions of the irradiated E and F series

It is expected that neutron irradiated samples will expand and such fact could be seen from the dimensional changes. However, due to uneven geometry of every individual specimen, it is not possible to draw results of dimensional changes. The results will be concluded with the measurements of exactly same pre- and post-irradiated samples, moreover, at the same locations

5.1.2 Density of specimens

Figure 5.1.2.1 concludes the results of density measurements for non-irradiated specimens. The corresponding values near the marks indicate the average values from 3 measurements, and the ranges below and above marks indicate standard deviations. As it may seem, the helium pycnometry results show good reproducibility, when in case of water pycnometry the results vary comparatively largely (even though outlying values were excluded), however, in the acceptable range.

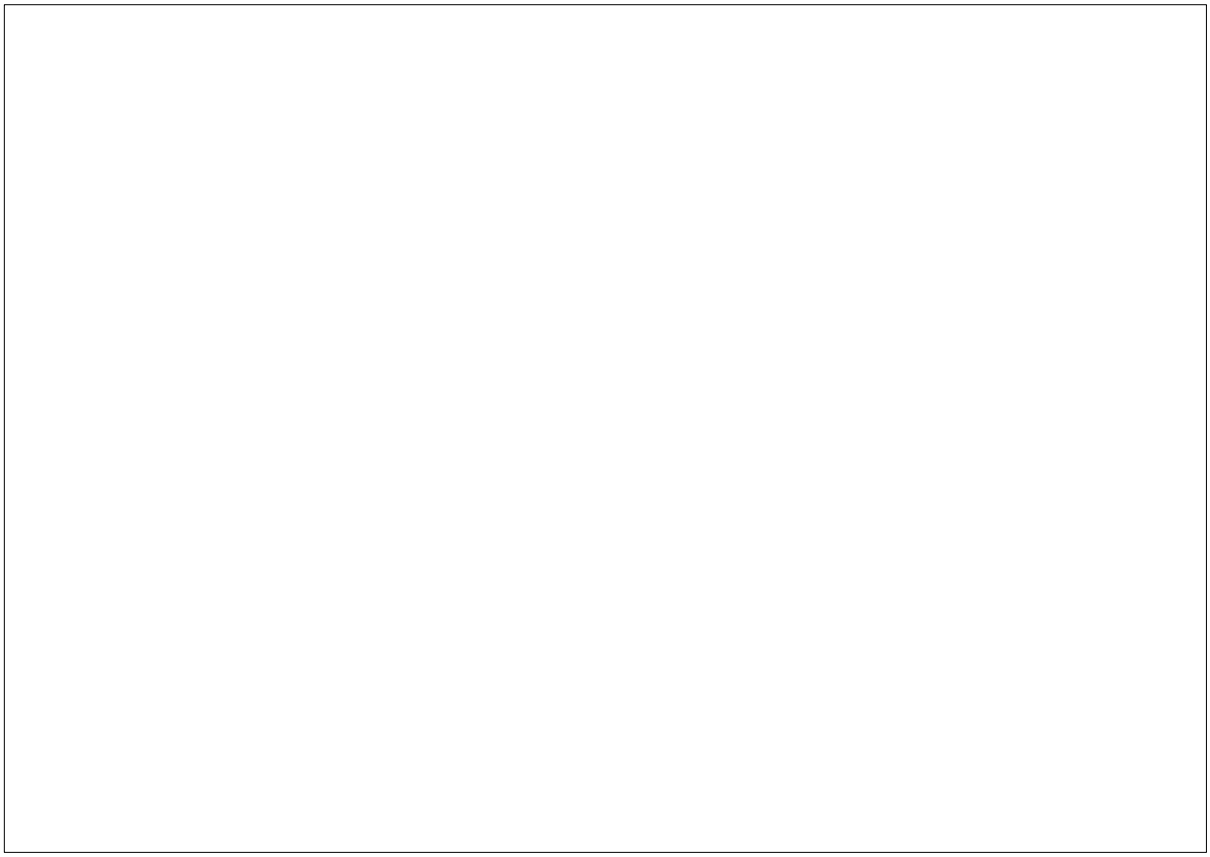

Figure 5.1.2.1. Density values of the non-irradiated specimens

As it may seem, the density values from helium pycnometry slightly larger than from water pycnometry. It could be explained by the penetration ability of helium and distilled water. Since the first one, in fact, is the gas represented by the smallest single atoms of helium, they could easily penetrate into the extremely narrow cracks replacing air, hence, show the real skeleton density. On the other hand, molecules of water are comparatively larger. Due to the fact, that the specimens were immersed into the water for less than a minute and in the depth (full immersion) with the lowest possible hydrostatic pressure, the absorption by water was minimized. Such facts could be used for assessment of porosity and volume of cracks. The porosity can be estimated by the ratio of densities:

$$p = \left(1 - \frac{\rho_w}{\rho_h}\right) \times 100\% \qquad (9)$$

where, p [%] is the porosity, ρ_w and ρ_h are densities obtained from water and helium pycnometers respectively.

Similarly, the porosity can be estimated by the ratio of volumes, which were also measured from helium pycnometry and calculated from dimensional measurements, by the formula:

$$p = \left(1 - \frac{V_h}{V_d}\right) \times 100\% \qquad (10)$$

where, V_h and V_d are the volumes from helium pycnometry and dimension measurements respectively. The results are concluded in Table 5.1.2.1, where the highlighted cells indicate the errors from rough approximation of samples geometry.

Table 5.1.2.1. Porosity and pore volume of the non-irradiated specimens

Figure 5.1.2.2 concludes the results of density measurements for irradiated specimens. As it may seem, the obtained results show comparatively better accuracy. Similarly, the E and F series of specimens vary in densities as in the case of non-irradiated series.

It is expected that irradiated samples will decrease in density. Therefore, in an attempt to draw an evidence of such fact, densities (from helium pycnometry) (Table 5.1.2.1 and Table 5.1.2.2) of each respective aggregate series were averaged and compared to each other. As a result, average skeleton density of irradiated samples E 2,26 % lesser than non-irradiated E series. The decrease in density in this case is accounted for volumetric expansion of present phases excluding volume of cracks in minerals and between phases. Similarly, increase in porosity by 5,56 % and 2,4 % were calculated according to Eq. 9 and 10 respectively for averaged pre- and post-irradiated E and F specimens. However, the results will be concluded with the measurements of exactly same pre- and post-irradiated samples.

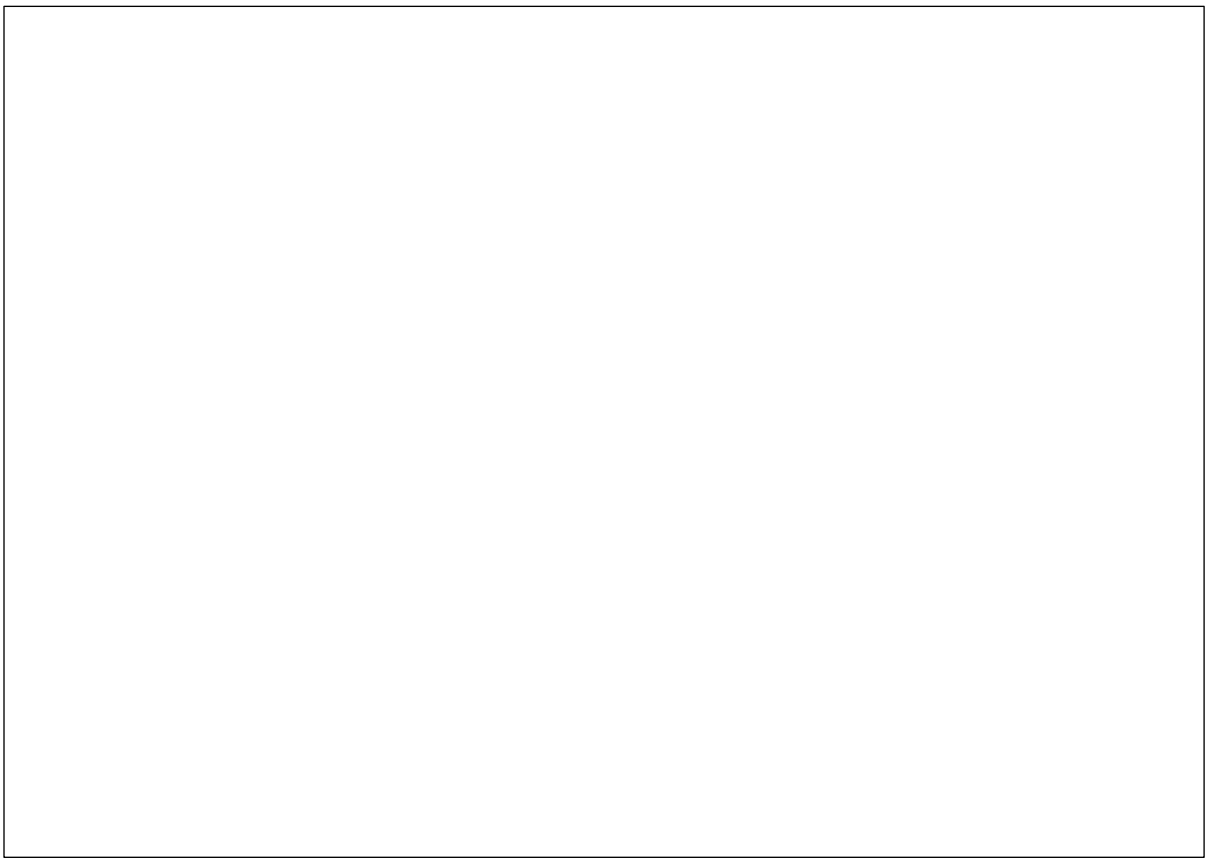

Figure 5.1.2.2. Density values of the irradiated specimens

Table 5.1.2.2. Porosity and pore volume of the irradiated specimens

5.1.3 Light optical microscopy

Thin sections of different types of aggregates were investigated with the goal to classify the rock type, describe the main textural features of the individual aggregates and assess the homogeneity of the cylindrical samples taken. The differences within the samples of the individual rock type may have an impact on the assessment of the quantities of main rock-forming minerals in each sample of the aggregate type using the Rietveld analysis of acquired XRD patterns. The variation in the mineral composition of individual samples may be

significant, because the rocks examined are of sedimentary origin and their homogeneity is dependent also on the method of sampling in the field, in relation to the layering, sorting, diagenesis, lithification and cementation. Table 5.1.3.1 shows the typical texture of the different aggregate types together with the range of grain sizes of the sedimentary rocks. The grains typically show no preferred orientation, but in some samples, weak lamination or subparallel orientation of the matrix was observed.

Table 5.1.3.1. Aggregate type, grain size and texture

Aggregate Type	
Grain size [mm]	
Image (plane polarized light)	

Aggregate type E – The grain size and texture vary among each specimen; laminar texture can be observed in the samples E32 and E38; quartz veinlets and pockets of fine-grained matrix formed by clay and micas are distributed non-homogeneously.

Aggregate type F – The quartzite sample is typically very fine-grained, with alternating parts of the coarser-grained texture; some of the aggregates exhibit the traces of alteration – the presence of veins filled with secondary micas clinochlore; sample F32 showing laminar texture; quartz veinlets are abundant.

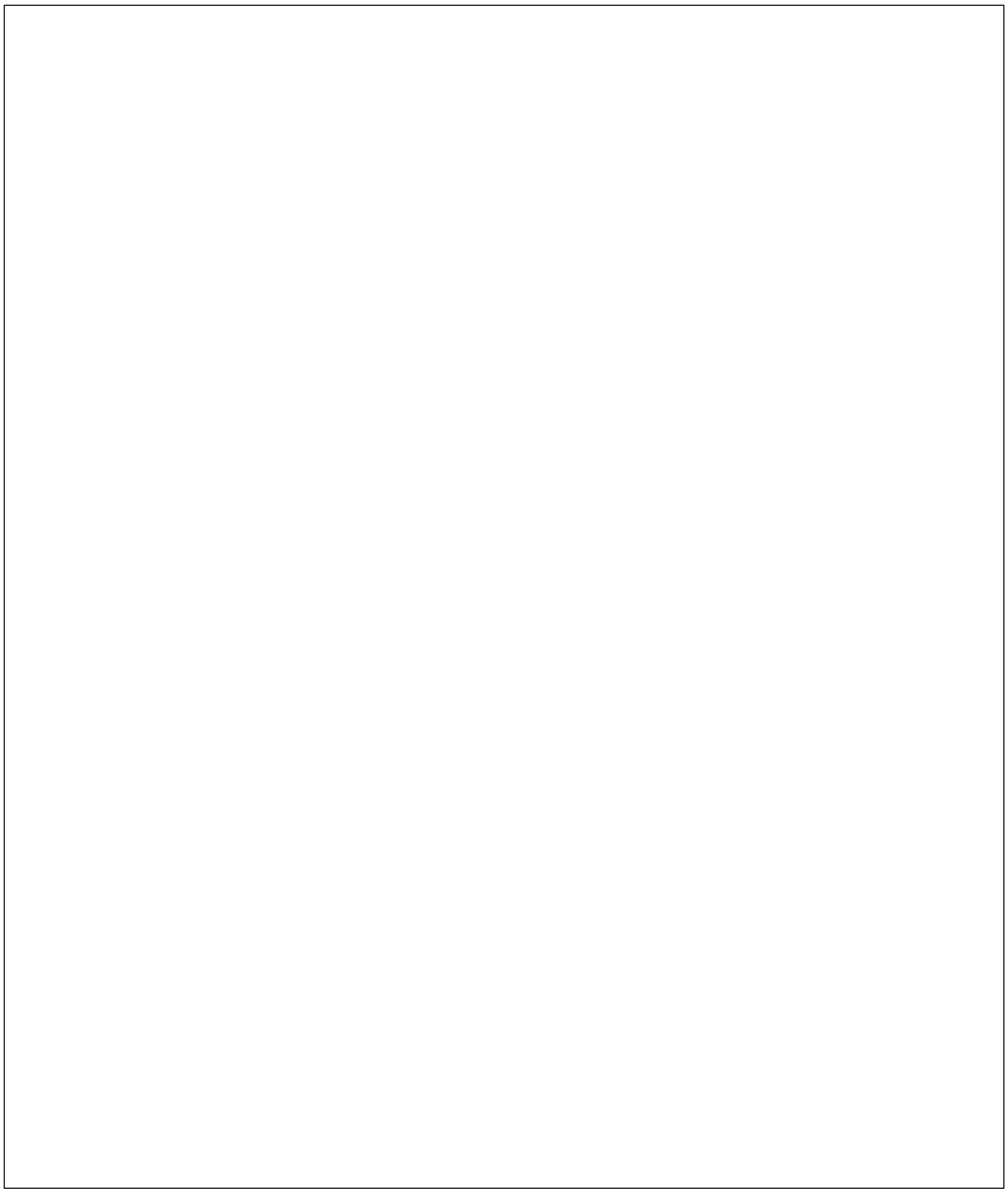

Figure 5.1.3.1. LOM images of the non-irradiated E series

Light optical micrographs of the representative texture of aggregate type E samples, taken in plane-light. The observed rock type is a fine to medium grained sandstone, composed of angular to subangular grains of quartz and feldspar, surrounded by fine-grained matrix of mica and clay minerals. Locally, quartz veinlets are penetrating through the lithified clastic mass. Psammitic layers are alternating with clay inserts, as was captured on E38 sample.

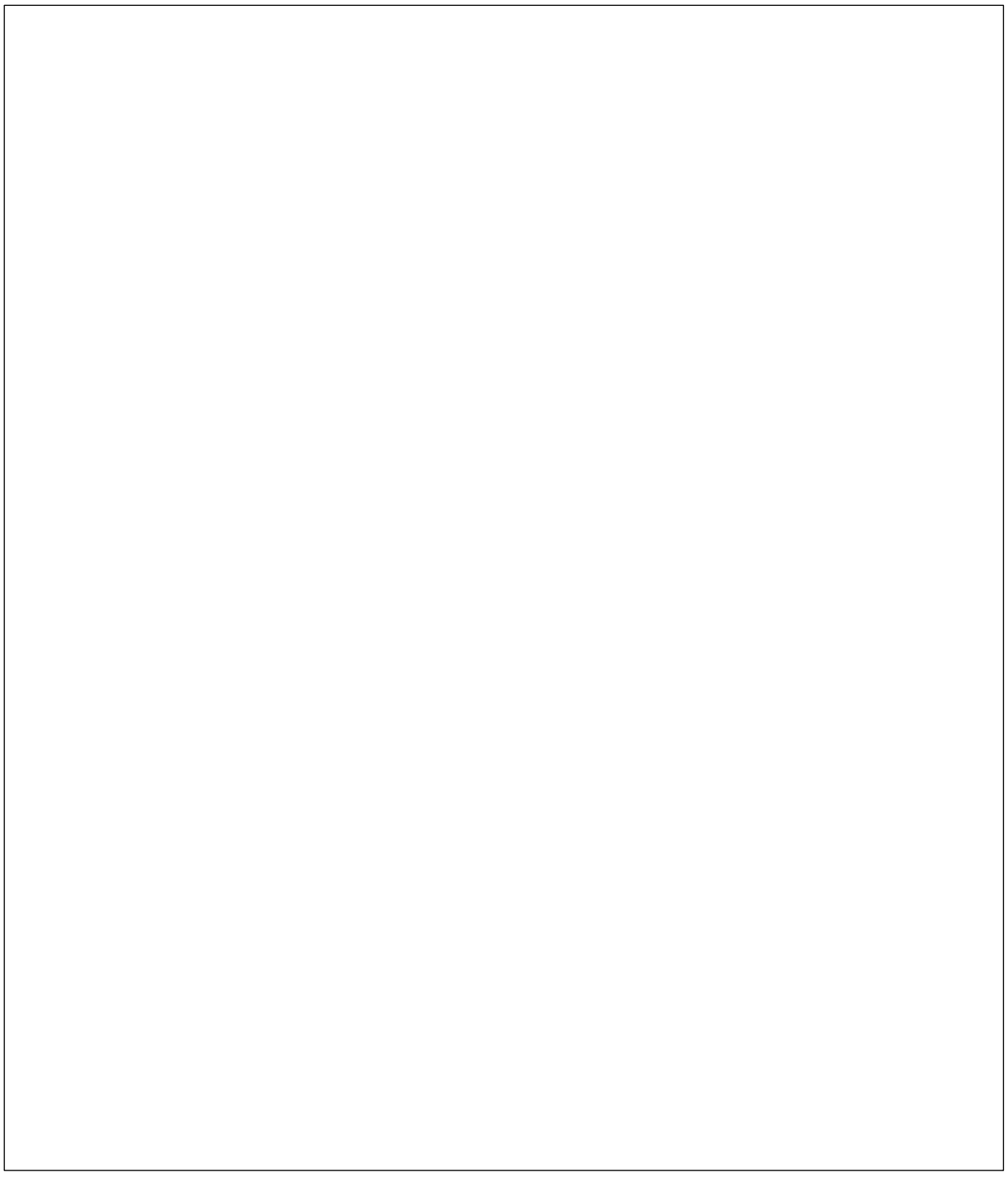

Figure 5.1.3.2. LOM images of the non-irradiated F series

Light optical micrographs of the representative texture of aggregate type F samples, taken in plane-light. The observed rock is a very fine-grained quartzite composed of a very fine-grained polygonal equant grains formed by recrystallization. The size of the recrystallized quartz grains varies locally and numerous quartz veins are clearly visible. Products of secondary alteration (cracks filled with micas) can be observed.

During the microscopy of the irradiated samples (both E and F series), no clear changes of

optical properties (such as amorphization, extinction) were observed in quartz or feldspars. The clastic portion of the type E samples remain transparent, no glassy component was observed. In the sample E07, recrystallized quartz domains were observed.

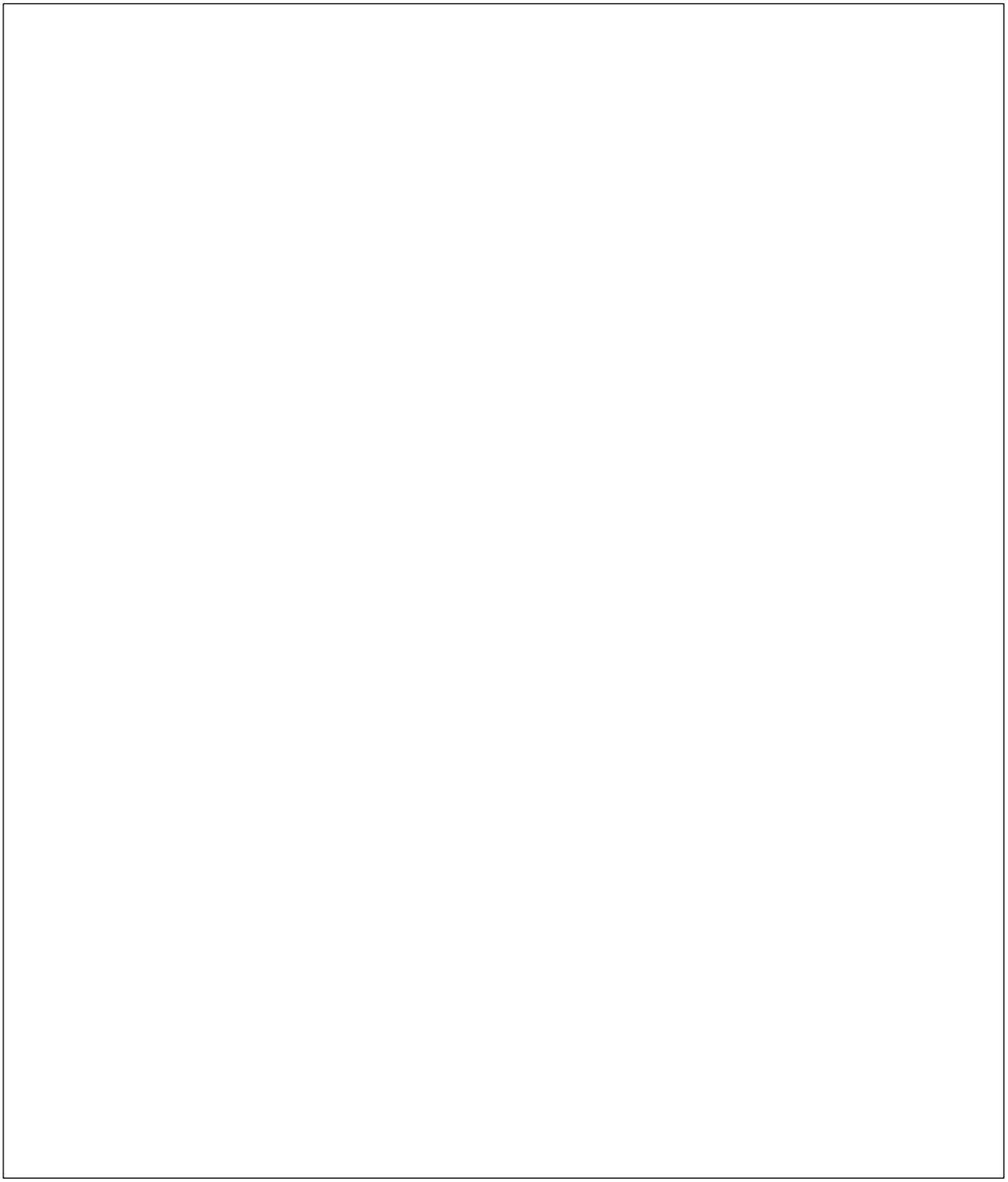

Figure 5.1.3.3. LOM images of the irradiated E series

Figure 5.1.3.4. LOM images of the irradiated F series

Decomposition of potassium feldspar into albite and illite is commonly observed. For F series, alternating parts of fine-grained and coarser-grained texture is typical. Sample F07 contains large amounts of sulphides, dispersed in the matrix. Figures 5.1.3.3 and 5.1.3.4 are demonstrating the main features of each specimen observed.

5.1.4 Scanning electron microscopy

The specimen series E and F were studied in the form of thin section using the means of electron microscopy and microanalysis. Both sample series belong to sedimentary type of rocks. Electron images taken in backscattered mode (BSE) were used to distinguish individual mineral phases present in the studied samples, phase identification was done using point EDX quantitative analysis.

- **Non-irradiated E series:**

The most common minerals in the E series (sandstone) are quartz, feldspars (albite-oligoclase, K-feldspar), also include common micas (biotite, muscovite), clinochlore and illite. The texture is strongly variable among the samples, main pattern is that quartz is the dominant mineral.

- **Non-irradiated F series:**

In the F series (quartzite) found very small grains of potassium-feldspar. Main minerals observed in the F series are quartz and potassium feldspar, also include pyrite, fluorine-apatite, clays in veinlets and calcium-sodium-plagioclases as accessories. Numerous brittle cracks in F27, F37 and F38 are filled with the secondary product – micas (biotite) and clinochlore, while F32 and F39 are the most homogeneous aggregates.

Phase composition of the E and F series represented in Table 5.1.4.1.

Table 5.1.4.1. Phase composition of the non-irradiated E and F series

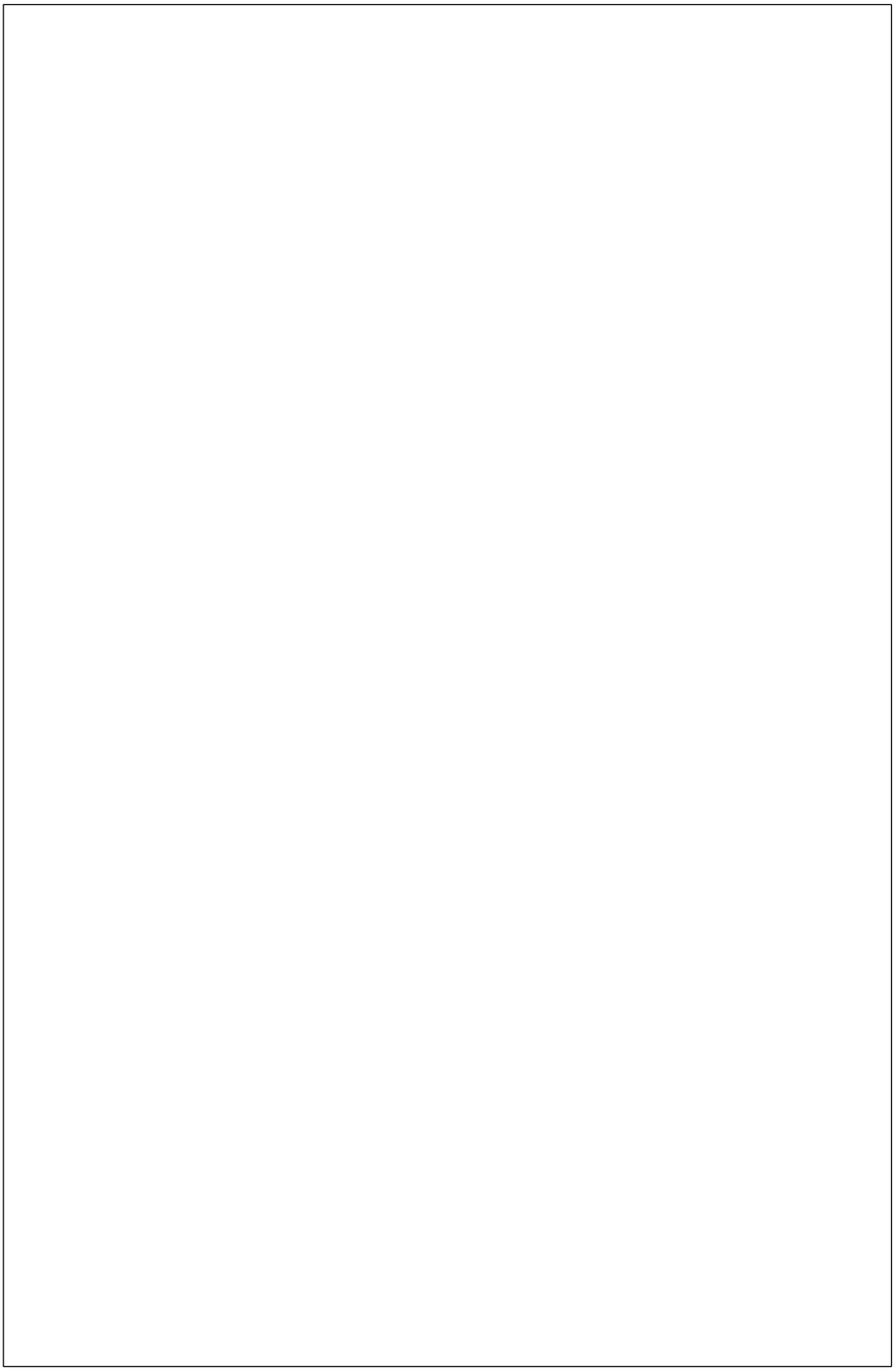

Figure 5.1.4.1. Phase composition map of the non-irradiated E series

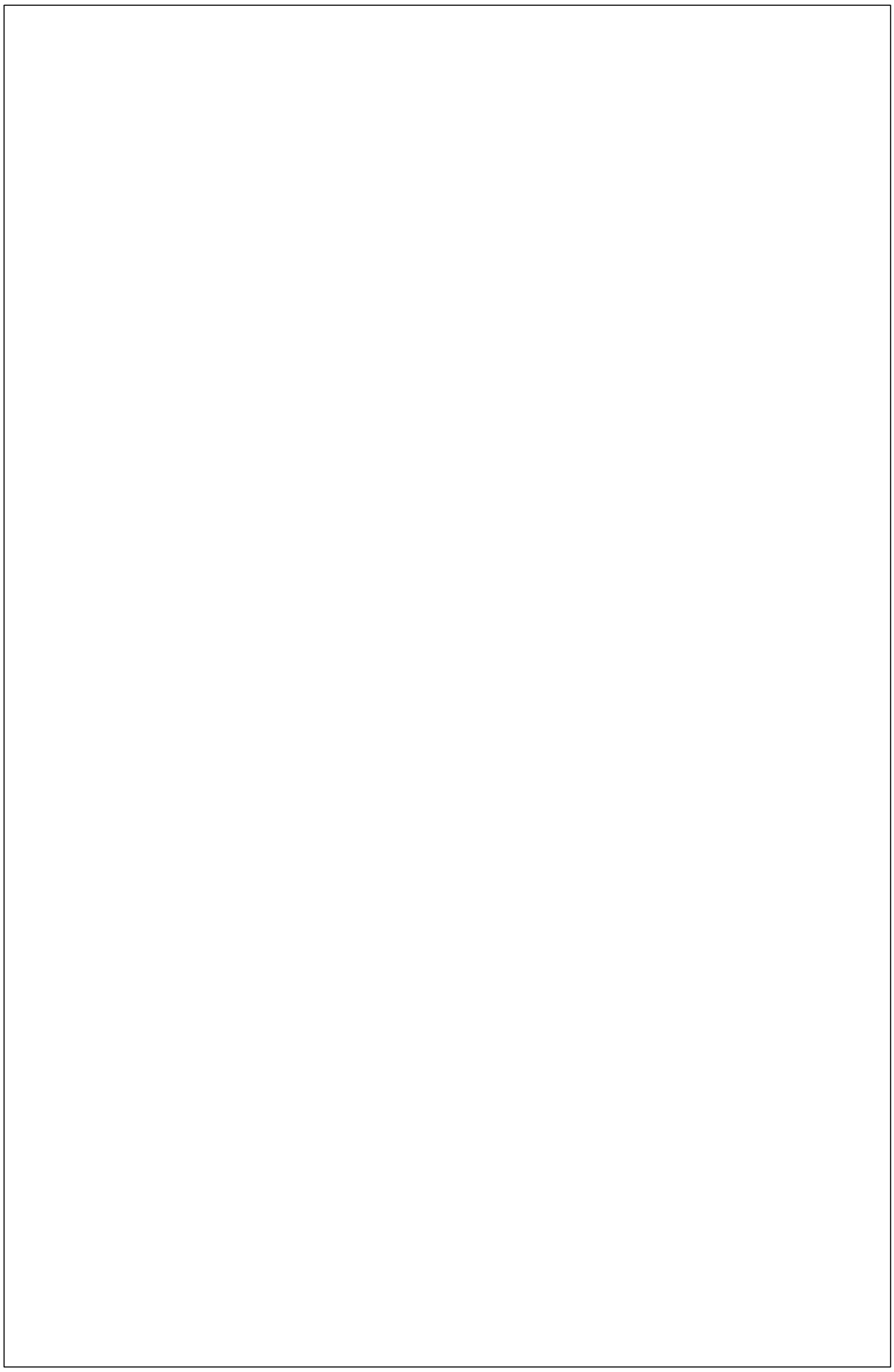

Figure 5.1.4.2. Phase composition map of the non-irradiated F series

As in the case of non-irradiated E series, the texture and mineral content is variable among the

samples. The dominant minerals are quartz and feldspars (present as K-feldspar and Na-plagioclase). The highest content of quartz in the sample E19. Samples E07 and E08 have the highest Na-plagioclase content, and sample E14 contain large portion of accessory minerals. Numerous cracks can be observed in the samples E01 and E02, as a result of compression testing of the specimens prior the sample preparation.

Quartz is the most dominant mineral in all irradiated samples of F series, having different grain-sizes in individual samples, newly formed quartz veinlets are common and are often followed by the presence of mica or clinochlore insets. The presence of micro-sized potassium-feldspar and calcium-sodium-plagioclase grains within the quartz matrix is typical. Main accessory minerals include pyrite and apatite, pyrite is associated with newly filled quartz veins and traces of chalcopyrite was also found in some specimens.

Table 5.1.4.2. Phase composition of the irradiated E and F series

Slight differences in averaged fraction of phases are seen (Table 5.1.4.1 and Table 5.1.4.2) between the same pre- and post-irradiated series.

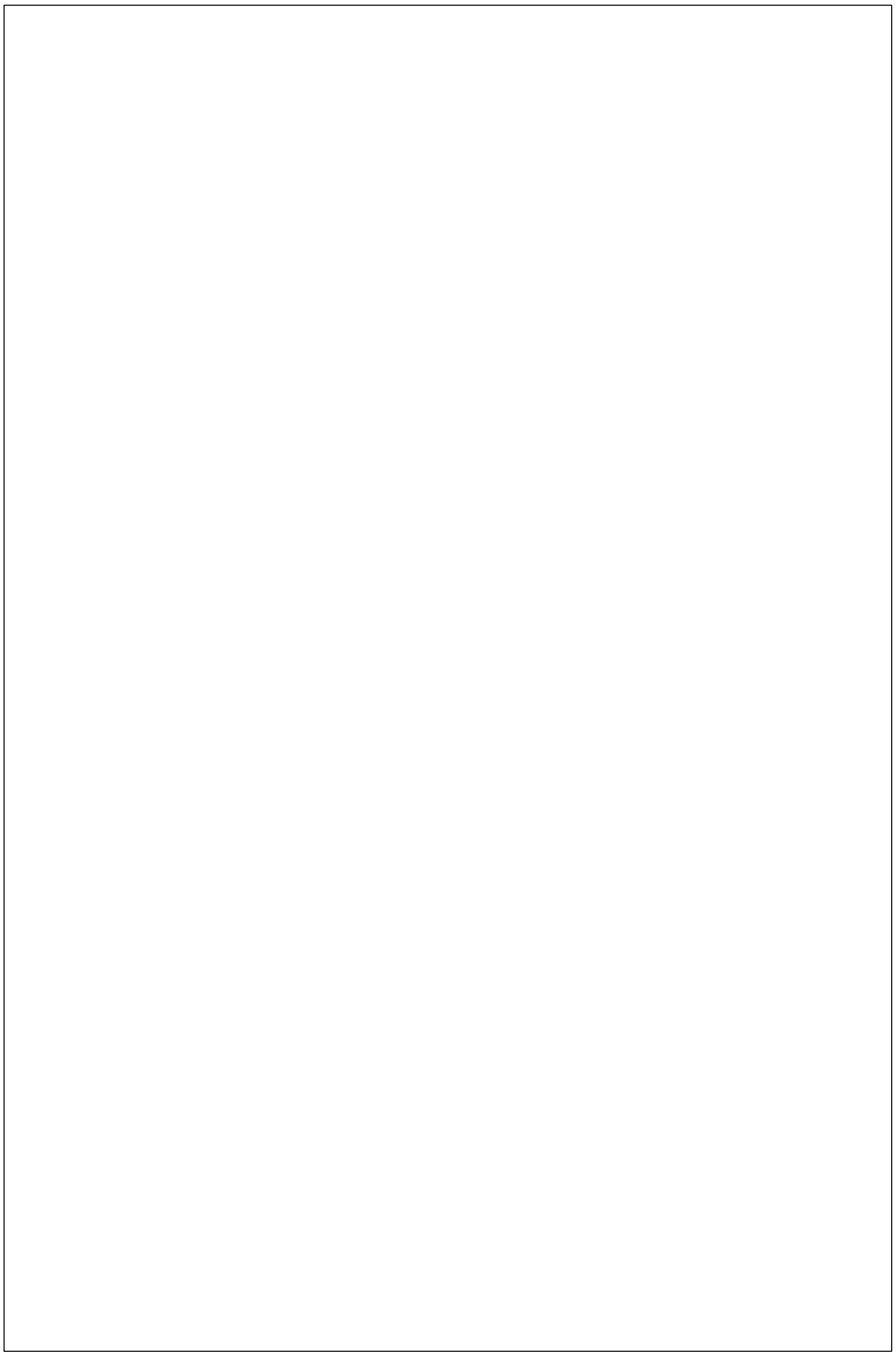

Figure 5.1.4.3. Phase composition map of the irradiated E series

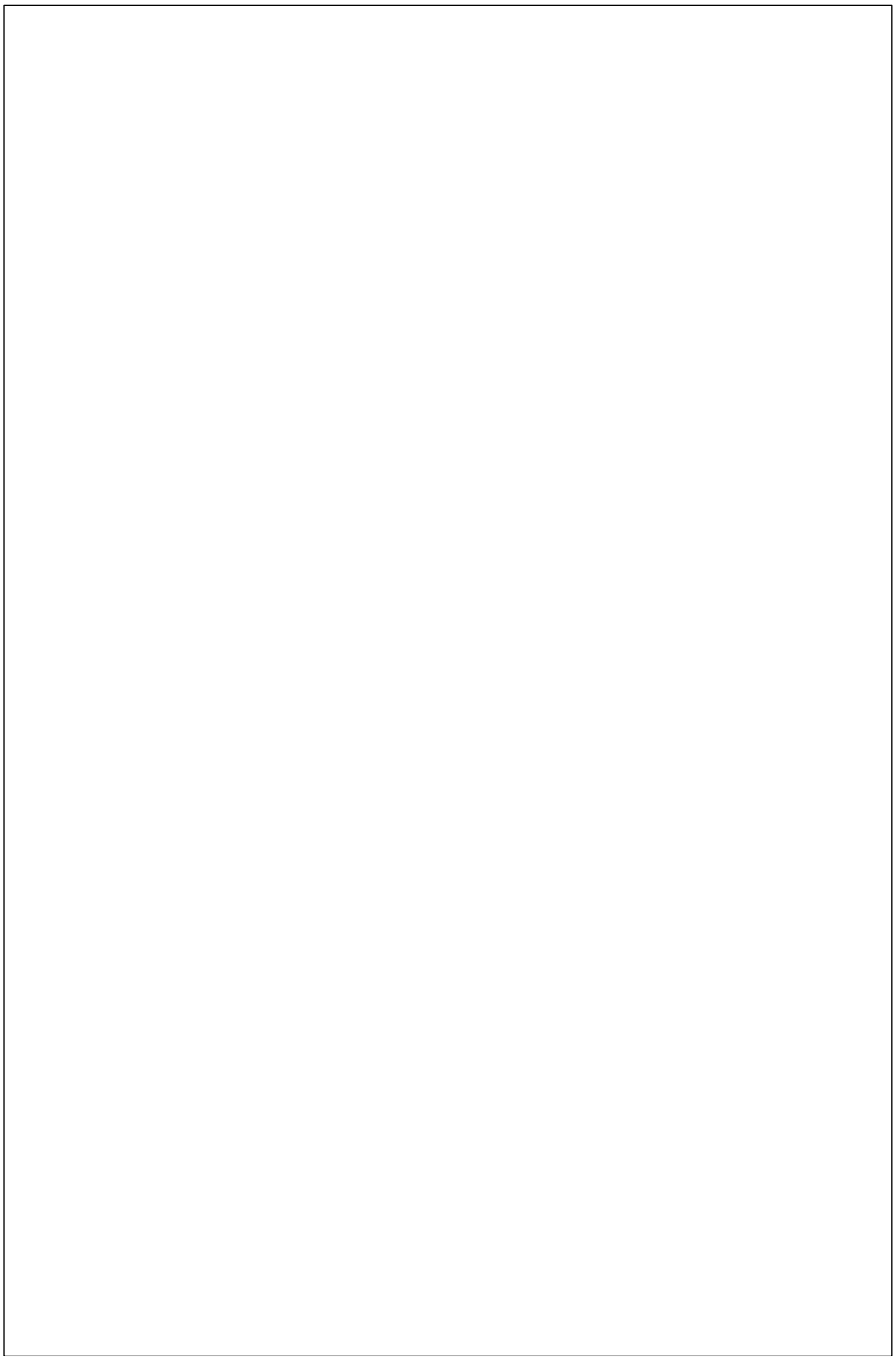

Figure 5.1.4.4. Phase composition map of the irradiated F series

5.1.5 Raman microscopy

A full spectrum is taken at different points of the pre- and post-irradiated samples. The point analyses were conducted for comparison of the non-irradiated and irradiated samples of the same type, with the special focus on characterization of main minerals.

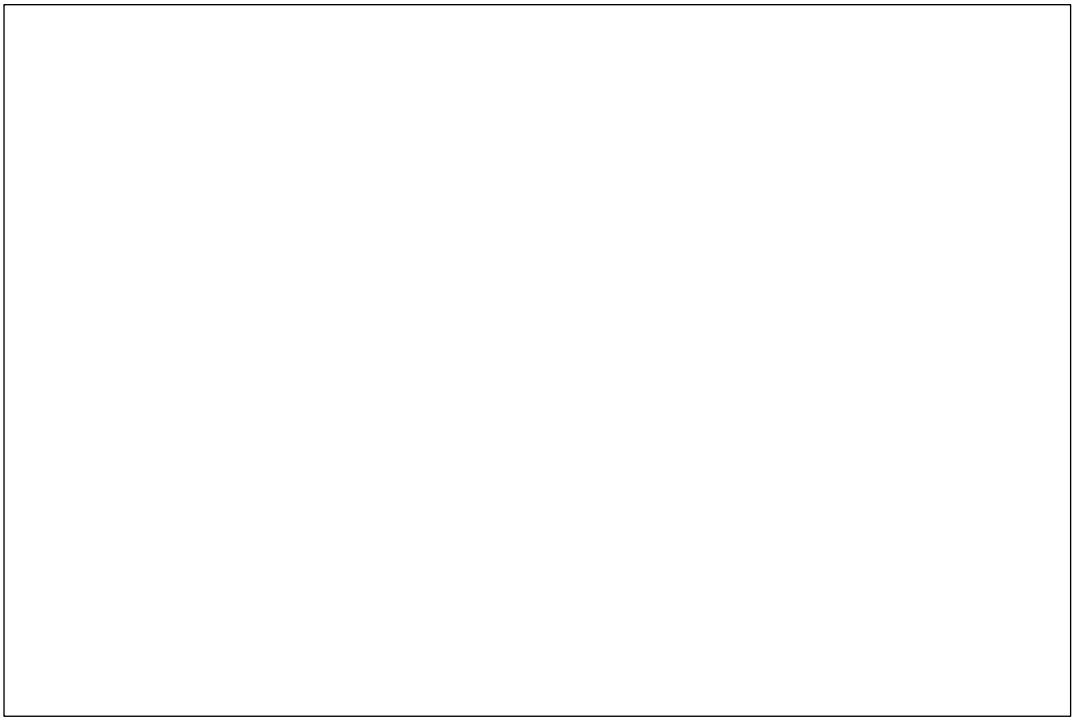

Figure 5.1.5.1. Raman spectra of quartz in the non-irradiated E series

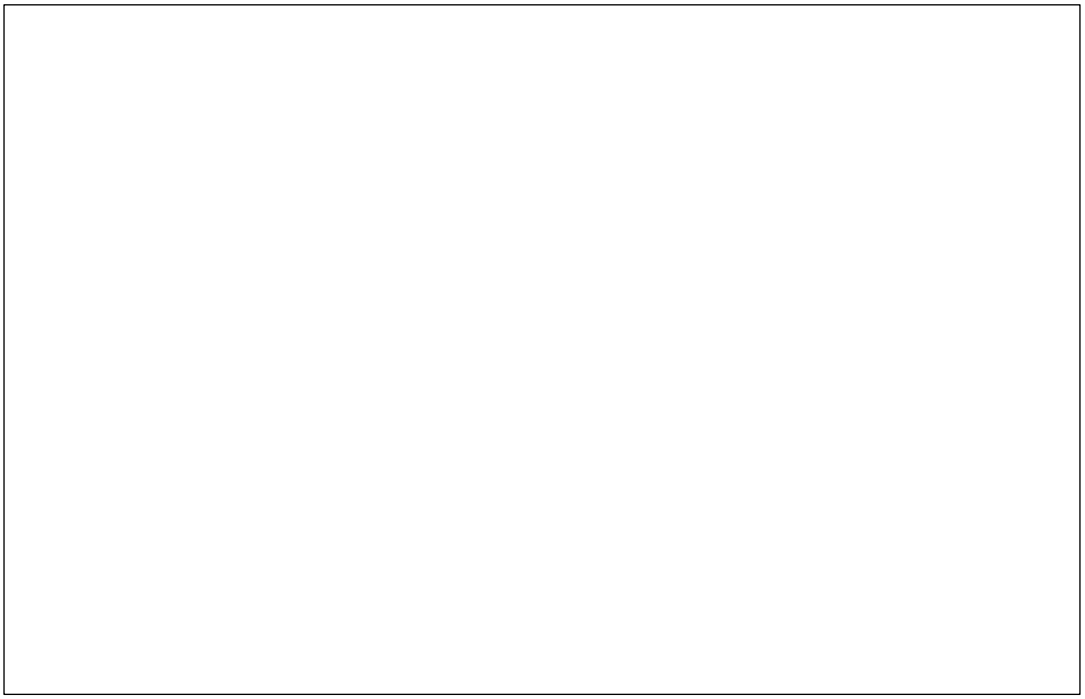

Figure 5.1.5.2. Raman spectra of albite in the non-irradiated E series

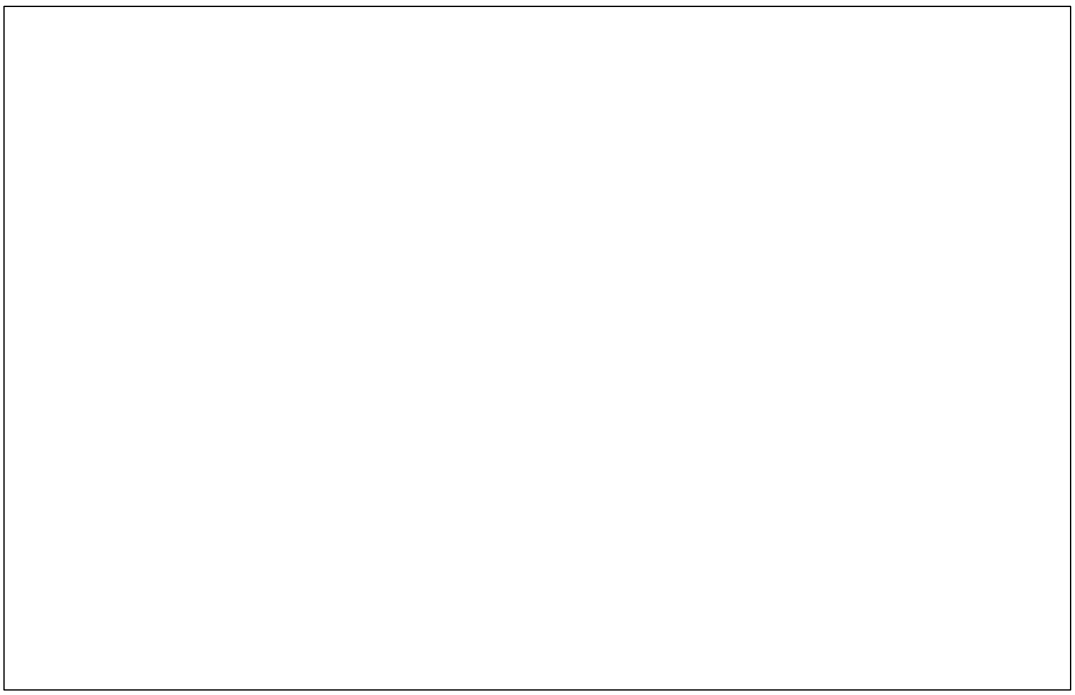

Figure 5.1.5.3. Raman spectra of quartz in the non-irradiated F series

The obtained data (Figures 5.1.5.1 – 5.1.5.3) of phase identification complement the data from the SEM.

Table 5.1.5.1 concludes found main minerals and accessories.

Table 5.1.5.1. Phase composition of the irradiated E series by Raman microscopy

Figure 5.1.5.4 illustrates Raman spectra of quartz in the irradiated E series. Spectra of quartz in samples E07, E08, E19, E20 show typical bands of crystalline quartz at about 463, 354, 263, 202 and 126 cm^{-1}. There are some slight changes for spectra of samples E13 and E14, the peaks become broader and change positions. For samples E01 and E02, the bands of crystalline quartz are replaced by amorphous quartz, as a result of defect accumulation.

Figure 5.1.5.4. Raman spectra of quartz in the irradiated E series

Figures 5.1.5.5 and 5.1.5.6 illustrates Raman spectra of albite and K-feldspar in the irradiated E series respectively. For the spectra of albite in samples E01 and E02, the peaks are most of broad. With samples E13 and E14 the peaks are broader compared to E19 and E20. Crystalline structure of albite and K-feldspar was metamictized by the same mechanism of defect accumulation.

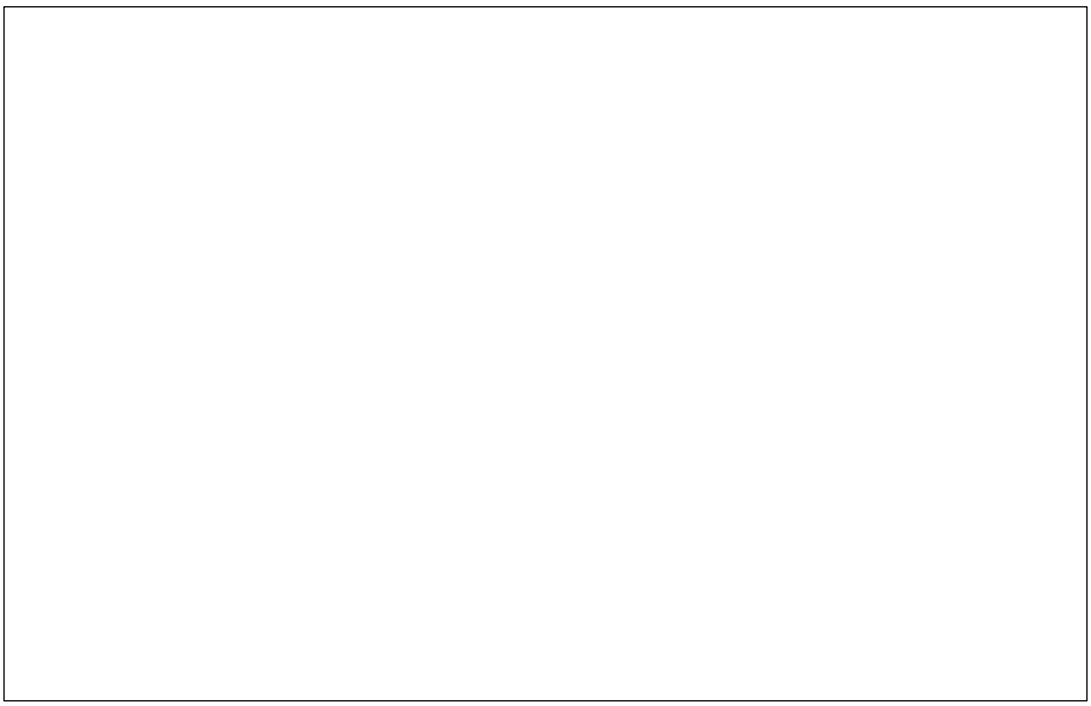

Figure 5.1.5.5. Raman spectra of albite in the irradiated E series

Figure 5.1.5.6. Raman spectra of potassium feldspar in the irradiated E series

Phase identification for the irradiated F series summarized in Table 5.1.5.2.

Table 5.1.5.2. Phase composition of the irradiated F series by Raman microscopy

There was observed similar behaviour of quartz in the irradiated series F (Figure 5.1.5.7) compared to the irradiated E series. Samples F07, F08, F19 and F20 show spectra with characteristic bands of crystalline quartz, while the bands of quartz in sample F13 are broader. The most significant changes are observed in spectra of samples F01 and F02, where the bands of quartz are replaced by amorphous quartz.

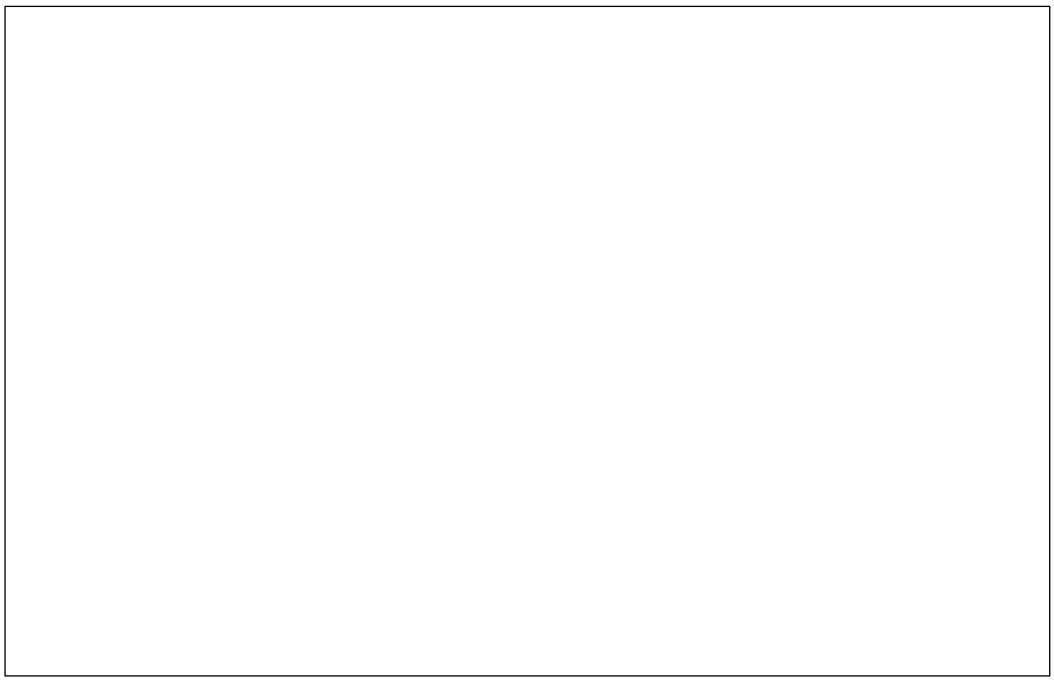

Figure 5.1.5.7. Raman spectra of quartz in the irradiated F series

5.1.6 Fourier-transform infrared spectroscopy

The strong broad band at around 1000 cm^{-1} created by multiple overlapping peaks belong to the SiO vibrations. The existence of quartz in the sample is indicated by the bands at around 1161, 1080, 795, 778, 694, 512 and 455 cm^{-1} (Figure 5.1.6.1). The bands at 990, 761, 745, 724, 648 and 589 cm^{-1} are assigned clearly to albite in these samples.

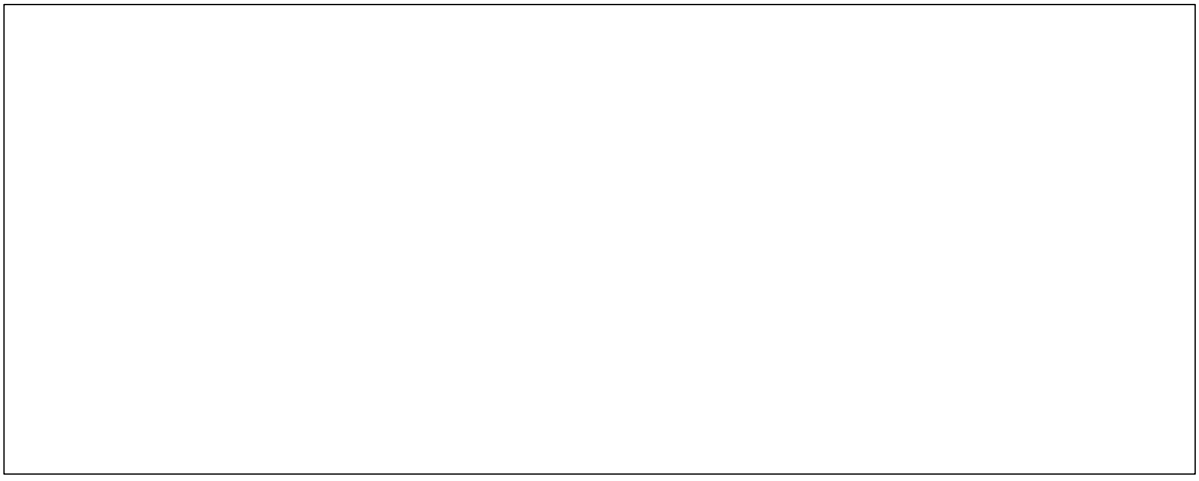

Figure 5.1.6.1. FTIR spectrum of the non-irradiated E series, left) full range; right) detail

The spectra of the sample series F indicate that the main component is quartz with the vibrational bands at 1162, 1051 (shoulder 1081), 795, 777, 694, 512 and 455 cm^{-1} (Figure 5.1.6.2). Other very weak bands at around 550-700 cm^{-1} are assigned to some trace of other components.

Figure 5.1.6.2. FTIR spectrum of the non-irradiated F series, left) full range; right) detail

FTIR spectra for the irradiated series E illustrated in Figure 5.1.6.3.

For samples E07, E08, E19, E20, the existence of quartz in samples is observed exhibiting characteristic bands at around 1050, 779, 694, 516 and 454 cm^{-1}. The bands at 762 and 743 cm^{-1} are assigned to albite. And other bands at 723, 648, 586, 529 and 420 cm^{-1} could be assigned to albite or potassium feldspar.

As for samples E13 and E14 in comparison with the samples E07, E08, E19 and E20, the typical peaks assigned to quartz are broader and have less intensity at 779 and 693 cm^{-1}. The bands at 726, 645 and 583 cm^{-1} are of albite and K-feldspar.

In case of samples E01 and E02, the characteristic bands of quartz are disappeared. Instead of that, the bands at around 1000 and 783 cm^{-1} could be assigned to amorphous phase of SiO_2. The bands at 763, 579 and 535 cm^{-1} are typical for albite or potassium feldspar. The characteristic peaks of albite and potassium feldspar are very similar at the mid infrared range. On top of that, the peaks are broader, therefore it is difficult to distinguish between albite and potassium feldspar in the mixture.

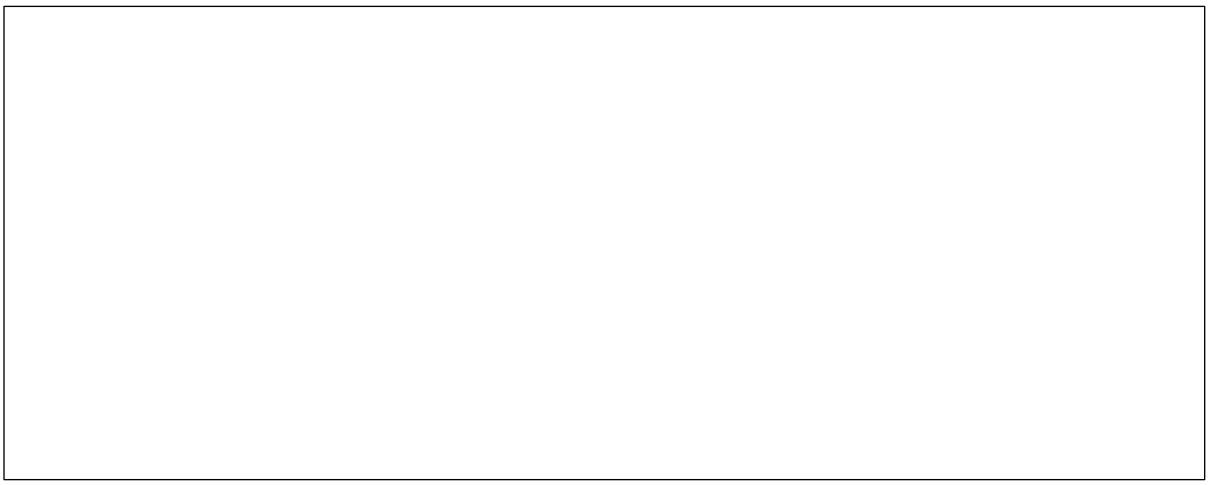

Figure 5.1.6.3. FTIR spectrum of the irradiated E series, left) full range; right) detail

FTIR spectra for the irradiated series F illustrated in Figure 5.1.6.4.

Changes due to neutron irradiation were also observed for the F series. Overview of the samples F contains the main quartz mineral. Spectra of samples F07, F08, F19 and F20 show the bands of quartz at 1050, 792, 776, 693 and 444 cm^{-1}. For samples F13 and F14 the characteristic bands of quartz are broader and less intensive, due to existence of 2 phases - remnant crystalline original quartz and amorphous phase of SiO_2. For samples F01 and F02, the bands of quartz are completely replaced by the bands of amorphous SiO at around 996 and 790 cm^{-1}. The peaks at very low intensity around 619 and 587 cm^{-1} appeared in most of spectra can be assigned to albite or potassium felspar.

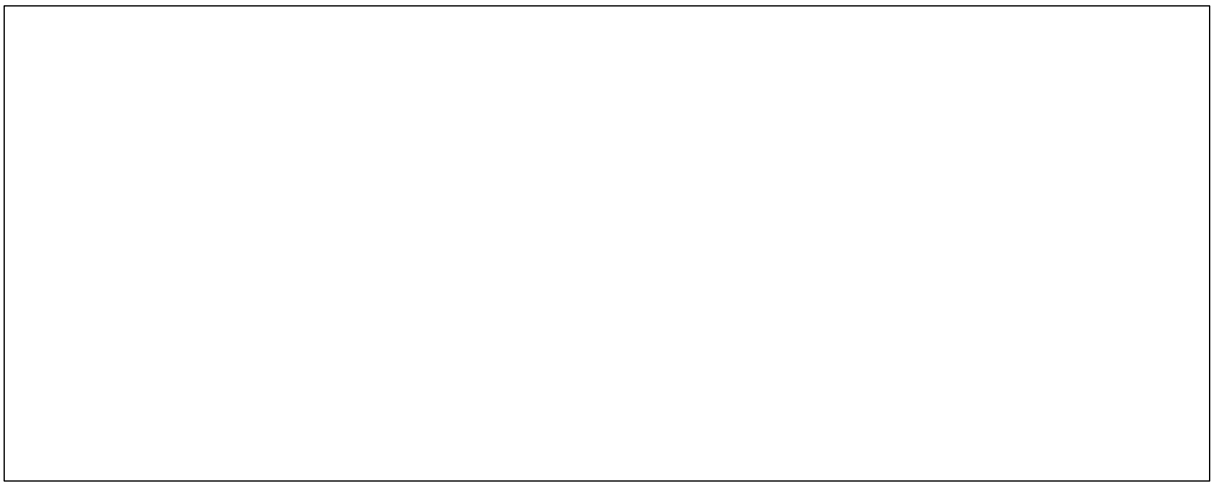

Figure 5.1.6.4. FTIR spectrum of the irradiated F series, left) full range; right) detail

5.1.7 X-ray diffraction

The results from XRD mineral phase identification are with good agreements to those obtained from the LOM observations. The non-active powders were measured in transmission mode. The identified phases (Figures 5.1.7.1 and 5.1.7.2) for each series of aggregates are listed in Table 5.1.7.1.

Table 5.1.7.1. XRD identification of mineral phases in the non-irradiated E and F series

Figure 5.1.7.1. XRD patterns for the non-irradiated E series; A – albite, B – biotite, C – clinochlore, M – microcline, m – muscovite, P – pyrite, p – pigeonite, Q – quartz, T – titanite, β – beta line

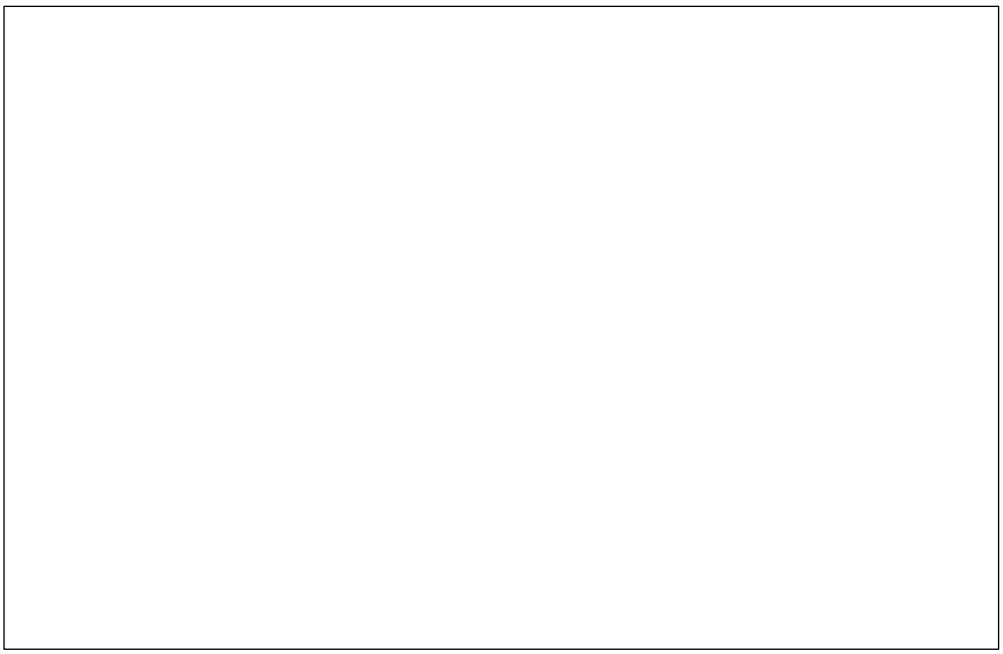

*Figure 5.1.7.2. XRD patterns for the non-irradiated F series; A – anorthite, B – biotite, C – clinochlore, M – microcline, Q – quartz, T – titanite, * - cordierite, β – beta line*

Rietveld quantitative analysis was performed for all measured XRD patterns. The first set of calculations is aimed at qualitative analysis of the present crystalline phase and determination of lattice parameters. The second set of calculations based on samples mixed with a ZnO standard in 1:1 ratio and is aimed in the analysis of the percentage of amorphous phase in each sample.

It was observed that composition of the E series aggregates varies between samples (Table 5.1.7.1). Complementing data from the LOM, it was confirmed that the main minerals are quartz and albite, also the samples contain accessory minerals such as clinochlore, microcline and micas (muscovite, biotite and illite) and minor traces of pyrite. The E38, in comparison with other samples, contains more albite; the E27 contains clinopyroxene (pigeonite).

As for aggregates of the F series (Table 5.1.7.1), the most dominant mineral is quartz with the fraction content up to 94 %, the minor phases assigned to microcline and anorthite with traces of titanite, fluorapatite, biotite and clinochlore. The F32 exhibits additional presence of cordierite. Table 5.1.7.2 represents the content of crystalline and amorphous phases with the standard deviation for the E series.

Table 5.1.7.2. Quantitative analysis of crystalline and amorphous phases in the non-irradiated E series

Table 5.1.7.3 represents the content of crystalline and amorphous phases with the standard deviation for the F series.

Table 5.1.7.3. Quantitative analysis of crystalline and amorphous phases in the non-irradiated F series

The identified phases for each series of the irradiated aggregates are listed in Table 5.1.7.4.

The composition of aggregates E is variable between samples, quartz and albite are the major phases; clinochlore, microcline and micas (muscovite, biotite, illite) are present in minor amounts, also traces of pyrite and fluorapatite are observed. In samples E01 and E08 besides the aforementioned phases there is around 10 % of amorphous-like silicon oxide phase. It is still not clear the formation of this phase, whether it is a product of a mechanical deformation of quartz during grinding or formed by neutron induced transition by irradiation.

Quartz is the main phase in the aggregates F reaching up to 92% of the total composition, excepting F01 and F02, where quartz contribution is less than 20%. Minor phases as microcline

and anorthite are observed, fluorapatite, titanium biotite, and clinochlore. Cordierite is also observed in the samples F01 and F08. The most degraded sample was F02, where the presence of amorphous content is visible at first sight, and it amorphous SiO_2 is clearly observed, besides that it was observed and unidentified peak at 2theta 36.6°.

Table 5.1.7.4. XRD identification of mineral phases in the irradiated E and F series

Figures 5.1.7.3 and 5.1.7.4 illustrate XRD patterns for the irradiated E and F series respectively.

Figure 5.1.7.3. XRD patterns for the irradiated E series; A – albite, B – biotite, C – clinochlore, c – calcite, I – illite, M – microcline, m – muscovite, P – pyrite, Q – quartz, s – silicon oxide, T – titanite

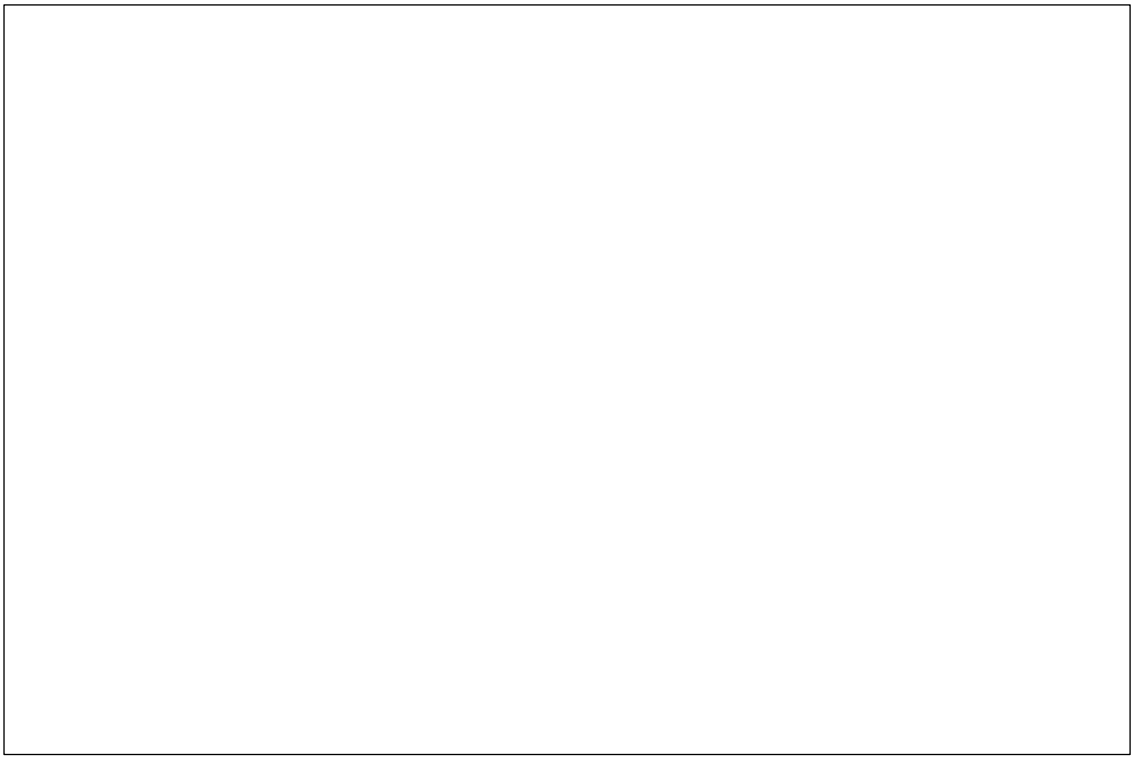

*Figure 5.1.7.4. XRD patterns for the irradiated F series; A – anorthite, B – biotite, C – clinochlore, c – cordierite, M – microcline, m – muscovite, Q – quartz, s – silicon oxide, β – beta line, * - unidentified peak*

In contrast to the non-irradiated E and F series, irradiated series exhibit presence of additional phases, which could be explained by phase transition under the neutron impact. The results

(Tables 5.1.7.4 and 5.1.7.5) of quantified amorphous content for both aggregates, which were measured three times together with an internal standard (ZnO) with a 1:1 ratio. In each table the average values of phases weight percentage with their respective standard deviation are presented and obtained by Rietveld analysis of the XRD patterns.

Table 5.1.7.5. Quantitative analysis of crystalline and amorphous phases in the irradiated E series

Table 5.1.7.6. Quantitative analysis of crystalline and amorphous phases in the irradiated F series

It is expected that with the higher fluence the amount of amorphous phase will increase, however, an anomaly was observed in comparison of the samples E07, E08, F07, F08 and E13, E14, F13, F14, where the data (Figure 5.1.7.5), probably, mistakenly states reverse. Assuming that the content of minerals was more or less the same, then the mistake could arrive from a sophisticated examination by Rietveld analysis or overgrinding of powder for XRD, another error, however less likely, could appear from badging of a false fluence value.

Non-irradiated samples E27, E32, F27 and F32 were chosen for comparison (Figure 5.1.7.5), it may be seen that practically no difference have appeared for the samples E19, E20, F19 and F20, only that the irradiated F series exhibit slightly higher content of amorphous phase. It could be explained by an increased content of quartz on average. The most vulnerable mineral is quartz, when irradiated it is metamictized and show the largest expansion, and the rate of volumetric growth is also larger with the larger fluence, when compared to other minerals. Therefore, samples F01 and F02 show even larger amorphization in comparison with E01 and E02 at the higher neutron radiation dose.

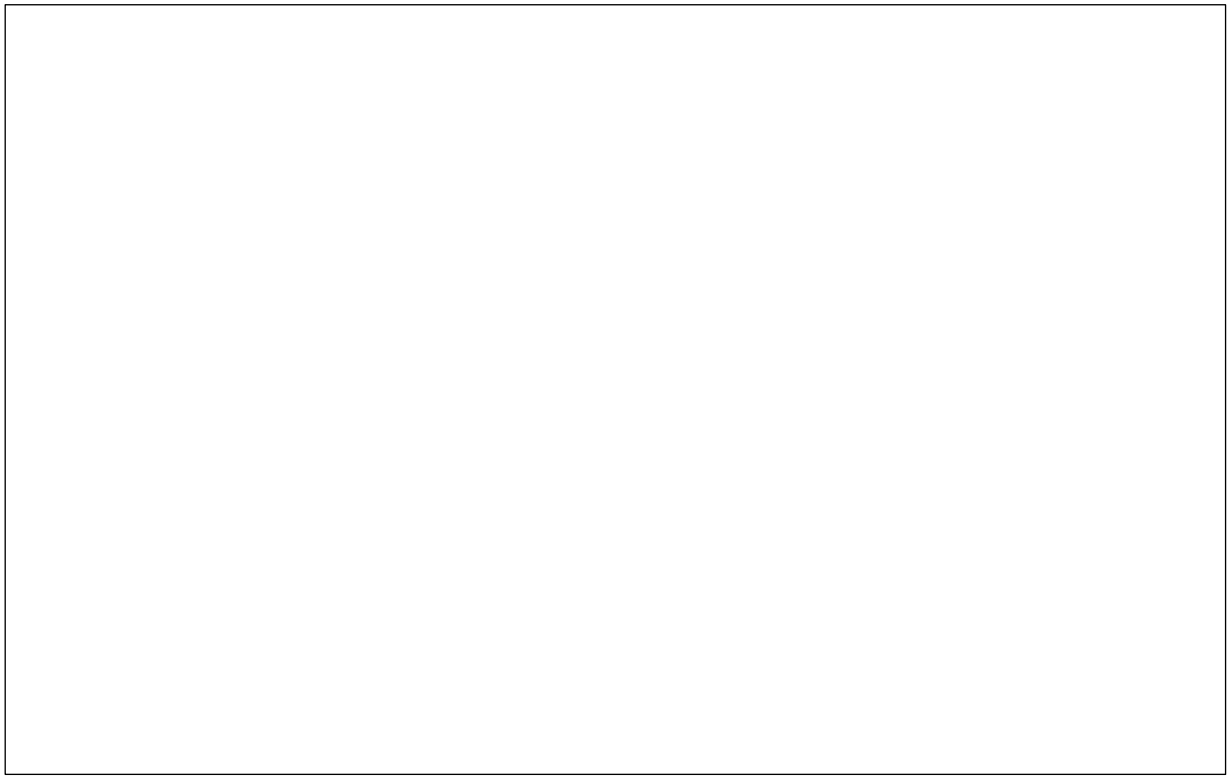

Figure 5.1.7.5. Content of the amorphous phase with respect to fluence

Moreover, lattice parameters (dimensions and volume of a unit cell in a crystal lattice) and crystal density of the main minerals were calculated at the CVŘ.

In case of calculations of the lattice parameters, it was observed that it was dependent on the range of measurements. Therefore, additional measurements were performed in the reflection mode with increased range of measurements (2θ: 5 - 140°), where θ is the angle of reflection. Also, thin sections, instead of powder, were used to exclude possible effects, such as deformation of lattice and amorphization of phases from overgrinding. When thin sections were not available, the data from powder was used. Table 5.1.7.7 represents physical dimensions and volume of a unit cell of a hexagonal structured quartz, where non-irradiated sample E27 was introduced for comparison.

*Table 5.1.7.7. Comparative results of quartz refined lattice parameters for aggregates E and F from thin sections; * - data from powder samples*

As it may seem, the expansive trend is continuous with the higher fluence, excepting samples E07, E08, F07 and F08, where somehow the contraction was observed.

Figure 5.1.7.6 show variation of cell parameters of different minerals with respect to fluence. It is evidently drawn that cell parameters, and, hence volume, increase with the increased fluence. Also, the rate of expansion of quartz is higher than for other minerals, this fact is well

noticed by Denisov *et al.* (Denisov et al., 2012), being that quartz is the main contributor in RIVE of rocks. The decrease of cell parameters reported for samples E07, E08, F07 and F08, which is questionable.

The obtained unit cell parameters of quartz (relative expansion) (Table 5.1.7.7) show good correlation (except samples E07, E08, F07 and F08) with the parameters of quartz obtained by Denisov *et al.* (Table 5.1.7.8). The correlation is also good for the respective minerals (Figure 5.1.7.6 and Table 5.1.7.8).

Table 5.1.7.8. Indicators of radiation change in the properties of crystalline minerals (Denisov et al., 2012)

Figure 5.1.7.6. Variation of lattice parameters and cell volume in function of fluence

Crystal densities of the main minerals were calculated at the CVŘ with the previously calculated cell parameters. It was verified that density of minerals decreases with the increased fluence. Therefore, the decrease in crystal density obtained as (Figure 5.1.7.7): quartz -8,3% (E aggregate) and -9,8% (F aggregate), microcline -1,2% (E aggregate) and -2,0% (F aggregate), albite -1,4% (E aggregate), anorthite -0,8% (F aggregate), muscovite -3,3% (E aggregate), and biotite-ti -1,6% (F aggregate). Since calculations were based on lattice parameters, again, the only anomaly was observed for the samples E07, E08, F07 and F08.

Figure 5.1.7.7. Variation of crystal density in function of fluence

5.2 Discussion on suitability of rock types as aggregates for CBS structure

When a question on suitability of rock types for CBS structure is raised, the right strategy is to address the question from multiple problems, such as shielding properties, reactivity regarding alkali-silica reaction and RIVE of aggregates.

Based on extensive data of mineral's RIVE collected by Denisov *et al.*, the RIVE is larger for rocks with the higher content of quartz. Based on limited experimental data, discussed in this

thesis, the contribution of content of quartz in RIVE is the most dominant. Also, it could be verified that the relative expansion of quartz is proportional to the volume fraction of amorphized phases (Zubov & Ivanov, 1966). Therefore, quartz content is the main factor contributing to RIVE. Since sensitivity of deterioration mechanism of concrete, in the first place, depend on expansion of aggregates, one way to increase service life of a CBS structure is to use aggregates with the lower content of quartz. The best suited aggregates are from olivine and pyroxene group of minerals having island or single/double chain structure.

Since the alkali-silica reaction occurs between the highly alkaline cement paste and amorphous silica in aggregates, the aggregates with the lower or no content of silica should be chosen, since the quartz is expected to be metamictized during the service life of a CBS wall. Calcite does not have silica at all, also, according to Denisov *et al.* (Denisov et al., 2012), the RIVE at saturation state is only 0,4 %.

Neutron and gamma ray possess stronger penetrating ability in comparison with alpha and beta radiation. Therefore, if the CBS structure is made of ordinary concrete, the minimum thickness for effective attenuation is ~2,7 m. The thickness can be reduced by addition of heavyweight aggregates, such as magnetite, hematite, ilmenite and serpentine, which, in return, exhibit comparatively low RIVE. In Russian NPPs, serpentinite is used as an aggregate for CBS wall. The reason is that serpentinite retains comparatively large amount of water under elevated temperature, and hydrogen containing compositions show a good shielding property against neutron radiation.

Conclusion

6.1 Conclusions of master's thesis

The effects of neutron irradiation on concrete aggregates were studied by the extensive list of available literature.

The baseline characterization of non-irradiated samples has been performed by means of optical measurement device, helium and water pycnometry, LOM, SEM + EDX, Raman microscopy, FTIR spectrometry and XRD at the CVŘ. The obtained data, such as density, of non-irradiated samples is in good correlation with the properties of minerals found in various sources. The samples were measured several times and the standard deviation is in the acceptable range. Therefore, very accurate results are expected when compared to irradiated state.

Irradiation of the samples has been performed at the LVR-15, however, as the post-irradiation examination is in progress, it was decided to proceed with the analogues, which were previously irradiated at the IFE.

The baseline characterization of irradiated samples has been performed by the same techniques. However, some samples were shipped in crushed condition, and were not suited for density measurements. The increase of the geometry of samples was expected, however, it was not possible to assess, since each aggregate varies in dimensions, and also the expected increase could be considered very small. The expected decrease in density was observed from both helium and water pycnometry. From the LOM, decomposition of potassium feldspar into albite and illite was commonly observed. From the FTIR, the significant changes were observed in spectra of samples F01 and F02, where quartz is replaced by amorphous quartz. From the XRD, with the higher fluence the amount of amorphous phase increased, however, an anomaly was observed for samples E07, E08, F07, F08. The uncertainties could arrive from a sophisticated examination by Rietveld analysis or overgrinding of powder for XRD. Calculated values of lattice parameters of quartz show good agreement with the lattice parameters of irradiated quartz found in Russian literature.

References

Bjergbakke, B. a. (2008). A comprehensive model to describe radiolytic processes in cement medium. J. Nucl. Mater.

Bouniol, P. A. (1998). *"Disappearance of Oxygen in Concrete under Irradiation : The role of Peroxides in Radiolysis* (Vols. Vol.28, No.11). Cement and concrete research.

Bykov, V., Denisov, A., Dubrovskii, V., Korenevskii, V., Krivokoneva, G., & Muzalevskii, L. (1981). *Effect of irradiation temperature on the radiation expansion of quartz* (Vol. 51(3)). Soviet Atomic Energy.

Caër, L. (2011). Water radiolysis: influence of oxide surfaces on H2 production under ionizing radiation. Water.

Charit, K. L. (2013). *An Introduction to Nuclear Materials: Fundamentals and Applications, First Edition.* Wiley-VCH Verlag GmbH & Co.

Denisov, A., Dubroskii, V., & Solovyov, V. (2012). *Radiation Resistance of Mineral and Polymer Construction Materials.* Moscow: ZAO Publishing House "MEI".

Dubrovskii, V. B., Ibragimov, A., Ladygin, S., & Pergamenshckik, B. K. (1966). *The effect of neutron irradiation on certain properties of refractory concretes* (Vol. 21). Atomnaya Energiya.

Dubrovskii, V. B., Ibragimov, S. S., Kulakovskii, M. Y., Ladygin, A. Y., & Pergamenshchik, B. K. (1967). *Radiation damage in ordinary concrete.* Soviet Atomic Energy.

Dubrovskii, V. B., Ibragimov, S., Korenevs, V., Ladygin, A. Y., Pergamen, V., & Perevalov, V. (1970). *Hematite concrete for shielding against high neutron fluxes* (Vol. 28(3)). Soviet Atomic Energy.

Dubrovskii, V. B., Ibragimov, S., Ladygin, A. Y., Kulakov, M. Y., & Pergamen, B. K. (1968). *Radiation stability of serpentine concrete* (Vol. 25(6)). Soviet Atomic Energy.

Dubrovskii, V., Lavdanskii, P., & Engovatov, I. (2010). *Construction of nuclear power plants.* Moscow: Publishing Association of Civil Ingeeniring Universities.

Elleuech, M. R. (1971). *Behavior of special shielding concretes and of their constituents under neutron irradiation.* Fourth United Nations International Conference on the Peaceful Uses of Atomic Energy 7.

ENSREG. (2018). *Topical Peer Review Report 'Ageing Management'.* European Nuclear Safety Regulator's Group.

Field, K. G., Remec, I., & Le Pape, Y. (2015). Radiation effects in concrete for nuclear power plants – Part I: Quantification of radiation exposure and radiation effects. *Nuclear Engineering and Design*, 126-143.

Fu, L., Nakamura, H., Yamamoto, Y., & Miura, T. (2017). Investigation of influence of section pre-crack on shear strength and shear resistance mechanism of RC beams by experiment and 3D RBSM analysis. *Journal of Advanced Concrete Technology*, 700-712.

Fujiwara, K. I. (2009). *Experimental study of the effect of radiation exposure to concrete.* Proceedings of the 20th International Conference on Structural Mechanics in Reactor Exposure.

Gray, B. (1971). *The Effect of Reactor Radiation on Cement and Concrete.* Risley Engineering and Materials Lab.

Hilsdorf, H., Kropp, J., & Koch, H. (1978). The effects of nuclear radiation on the mechanical properties of concrete. *ACI Special publication*, 223-254.

Ishikawa, S., Takizawa, M., Etoh, J., Sato, O., Maruyama, I., Kontani, O., . . . Igari, T. (2017). Update on JAMPSS Neutron Irradiation experiment conducted under Japanese NRA project. *International Committee on Irradiated Concrete (ICIC).* Prague.

Kawai, T. (1978). New discrete models and their application to seismic response analysis of structures. In *Nuclear Engineering and Design* (pp. 207-229). Nuclear Engineering and Design.

Khmurovska, Y. (2019). *Influence of Neutron and Gamma Irradiation on Concrete Properties and Structural Performance.* Prague.

Khmurovska, Y., & Štemberk, P. (2019). Mechanisms behind radiation-induced deterioration of concrete. *Materials Science and Engineering* (p. 596). Prague: IOP Conference.

Kontani, O., Ichikawa, Y., Ishizawa, A., Takizawa, M., & Sato, O. (2010). *Irradiation effects on concrete structures.* Int. Symp. On the Ageing Manag. of Nucl. P. P., 173-182.

Le Pape, Y., Alsaid, M. H., & Giorla, A. B. (2018). Rock-forming minerals radiation-induced volumetric expansion. *Journal of Advanced Concrete Technology, 16*, 191-209.

Lowinska-Kluge, A., & Piszora, P. (2008). *Effect of gamma irradiation on cement composites observed with XRD and SEM methods in the range of radiation dose 0-1409 MGy* (Vol. 114). Acta Phys. Pol.

Maruyama, I., & Sugie, A. (2014). Numerical study on drying shrinkage of concrete affected by aggregate size. *Journal of Advanced Concrete Technology*, 12(8), 279-288.

Maruyama, I., Kontani, O., Ishizawa, A., Takizawa, M., & Sato, O. (2012). *Development of system for evaluating concrete strength deterioration due to radiation and resultant heat.* Salt Lake City: Proceedings of 3rd International Conference on NPP Life Management for Long Term Operations.

Maruyama, I., Kontani, O., Sawada, S., Sato, O., Igarashi, G., & Takizawa, M. (2013). *Evaluation of irradiation effects on concrete structure-background and preparation of neutron irradiation test.* POWER 13, American Society of Mechanical Engineers.

Maruyama, I., Kontani, O., Takizawa, M., Sawada, S., & Ishikawa, S. (2017). Development of Soundness Assessment Procedure for Concrete Members Affected by Neutron and Gamma-ray Irradiation. *Journal of Advanced Concrete Technology, 15*, 440-523.

McDowall, D. C. (1972). *The Effect of Gamma Irradiation On the Creep Properties of Concrete.* Luxembourg: Central Electricity Research Laboratories.

Pedersen, A. (1971). *Radiation damage in concrete: measurements on miniature specimens of cement mortar.* Brussels: Proceedings of an information exchange meeting on "Results of concrete irradiation programmes".

Remec, I., Rosseel, M. T., Field, K. G., & Le Pape, Y. (2018). Radiation-Induced Degradation of Concrete in NPPs. Oak Ridge, TN: Oak Ridge National Laboratory.

Rosseel, T. M., Maruyama, I., Le Pape, Y., Kontani, O., Giorla, A. B., Remec, I., . . . Ordonez, M. (2016). Review of the Current State of Knowledge on the Effects of Radiation on Concrete. *Journal of Advanced Concrete Technology*, 14, 368-383.

Sasano, H., Maruyama, I., Sawada, S., Ohkubo, T., Murakami, K., & Suzuki, K. (2020). Meso-scale modelling of the mechanical properties of concrete affected by radiation-Induced aggregate expansion. *Journal of Advanced Concrete Technology*, 648-677.

Schneider, M. (2020). *The World Nuclear Industry Status Report 2020.* Paris: A Mycle Schneider Consulting Project.

Uetaki, A. (2019). *Current Status of Nuclear Power in Japan.* Japan Atomic Industrial Forum, Inc.

World Nuclear Association. (2020). *World Nuclear Performance Report 2020.* London: World Nuclear Association.

Yamamoto, Y., Nakamura, H., Kuroda, I., & Furuya, N. (2014). Crack propagation analysis of reinforced concrete wall under cyclic loading using RBSM. *European Journal of Environmental and Civil Engineering*, 780-792.

Zubov, V., & Ivanov, A. (1966). *Expansion of quartz caused by irradiation with fast neutrons* (Vol. 11). Soviet Physics Crystallography.